Understanding Combinatorial Atomic Layer Deposition and Chemical Vapor Deposition

A DISSERTATION
SUBMITTED TO THE FACULTY OF THE GRADUATE SCHOOL OF THE UNIVERSITY OF MINNESOTA
BY

Tyler Leighton Moersch

IN PARTIAL FULFILLMENT OF THE REQUIREMENTS FOR THE DEGREE OF DOCTOR OF PHILOSOPHY

Wayne L. Gladfelter

February, 2009

ACKNOWLEDGEMENTS

No body of scientific work can be completed without significant assistance. I would like to thank the following entities at the University of Minnesota for their support: the Gladfelter Research Group, the Department of Chemistry, the Characterization Facility, the Minnesota Supercomputer Institute, Benjamin E. Kucera, Victor G. Young, Jr., and the X-Ray Crystallographic Laboratory. I would like to thank CIRIMAT, ENCIACET, NSF and CNRS for the opportunity to study fludized bed reactors in Toulouse, France. I would also like to thank Amber Runge for her contributions to the computational modeling project. Funding for this work was provided by the National Science Foundation.

DEDICATION

I would like to dedicate this thesis to everyone who has supported, guided and enabled me to complete this project. I specifically dedicate this work to my thesis advisor, Wayne Gladfelter, whose patient and prescient guidance through this difficult task has made my work possible, and to my family, who was always there for me, through thick and thin. I thank all my coworkers throughout the years for their scientific discussions and encouragement. I am gracious to Constantin Valhas for advising my work in Toulouse, FR, on fluidized bed precursor delivery systems. Finally, I would like to thank everyone who helped me jump through hoops, file paperwork, strategize my career, discuss science, learn to be a good teacher and generally strive to be a good scientist.

ABSTRACT

The transformation of molecular precursor to solid film begins with an understanding of molecular structure, proceeds through delivery of the molecule to the surface and ends with the decomposition of precursor on the surface to form a deposit. An understanding of the physical and chemical processes leading from molecule to film enables the utilization of chemical precursors in effective deposition processes.

Single crystal X-ray crystallography was used to study the structure of $[NO]_{0.5}[NO_2]_{0.5}[Zr(NO_3)_5]$ and $[NO]_{0.5}[NO_2]_{0.5}[Hf(NO_3)_5]$. Infrared spectroscopy was employed to identify the nature of the cation in the crystal structure, and characteristic absorptions of both nitronium and nitrosonium cations were observed.

Fluidized bed reactor technology has been used to study the sublimation behavior of solid-state chemicals. Fluidization behavior, precursor mass transfer rates and delivery uniformity for aluminum trichloride were studied and the results reported.

Mixed metal oxide nanolaminate films of hafnium oxide and zirconium oxide interspersed with layers of silicon oxide have been deposited on silicon substrates by a combinatorial atomic layer deposition (ALD) technique. Exposure of repeated cycles of co-dosed alkoxide precursors $Hf[OC(CH_3)_3]_4$ and $Zr[OC(CH_3)_3]_4$ with counter-reactant pulses of $Si[OC(CH_3)_3]_3(OH)$ formed films of uniform thickness (±5%) and uniform silicon oxide concentration (85% per total metals basis). The hafnium and zirconium concentrations exhibited smooth gradation across the film from 18% - 82% (per Hf and Zr metals basis). Self-limiting deposition rates of 1.5 nm / cycle were measured, and a linear relationship of film thickness to number of deposition cycles was observed, both consistent with a true ALD process. Rutherford backscattering spectrometry, ellipsometry and X-ray reflectivity results were used to map the composition and determine the film microstructure.

Single precursor depositions have been performed and compared to computational models created using CFD-ACE in order to further the understanding of the interaction of fluid dynamics and chemistry in the combinatorial chemical vapor deposition process. The physical and chemical processes contributing to film growth in combinatorial chemical vapor deposition were evaluated.

TABLE OF CONTENTS

LIST OF FIGURES

LIST OF TABLES

CHAPTER 1

Introduction

Understanding the deposition of thin films by chemical reaction requires knowledge of molecular precursors, the process of mass transport, and the mechanism of film formation. Chemical reactivity of precursor molecules drives deposition processes occurring on the surface of a growing film which in turn dictates film morphology. Chemical properties of the precursor, such as vapor pressure, determine the mass transport phenomena involved in the delivery process; controlled delivery of precursor compounds to the deposition region is critical to predictable film formation. Observing film growth under a range of deposition conditions enables the correlation of film compositions and microstructures to the conditions under which the film was grown, which is advantageous when trying to create a specific stoichiometry or morphology. Control of deposited material is enabled by understanding the chemical processes involved in precursor delivery and molecular routes to film formation.

The process of thin film formation by chemical transformation of gas phase molecules into surface material with a different composition is called chemical vapor deposition (CVD). This is distinct from physical vapor deposition (PVD) where atoms or molecules are transported chemically unchanged to form thin films. Evaporation and sputtering are two examples of PVD methods. Generally speaking, CVD allows conformal coatings while PVD is limited to line-of-sight deposition. Molecular diffusion, both in the gas phase and on the surface, aids in the uniform distribution of surface coating under optimal conditions. A wide range of materials can be targeted through CVD, including metals, insulators, semi-conductors as well as various magnetic and optoelectronic materials. The purity of CVD deposits is often high, owing to the refined nature of the precursors, although partial decomposition and/or reaction can lead to impurity incorporation in the growing material. The refined nature of the precursor often adds cost to the process meaning some materials are cheaper to deposit by PVD rather than CVD.

Design and study of molecules intended for use in chemical vapor deposition allows effective implementation of a deposition route to materials with desired properties. As previously mentioned, precursor attributes contribute to the entire process, from creating the vapor to the morphology of the deposit. Knowledge of the precursor's

properties streamlines the formation of the target compounds. Sometimes the choice of precursor makes the implementation of the process easy. High volatility liquids or gases allow convenient metering for process control. Compounds that do not exhibit facile side-reactions with air or moisture allow for convenient handling and loading of the chemicals into the precursor delivery systems. No special protections, such as glove boxes or inert atmospheres are required for compounds such as this. However, the limited reactivity of these molecules that makes handling easy often makes deposition difficult to achieve. Thus chemical properties of precursors dictate not only the deposition chemistry but also engineering concerns surrounding implementation of such a process.

The synthesis, purification and characterization of the anhydrous metal nitrates of hafnium and zirconium, $[NO]_{0.5}[NO_2]_{0.5}[Hf(NO_3)_5]$ and $[NO]_{0.5}[NO_2]_{0.5}[Zr(NO_3)_5]$, will be presented in Chapter 2. These compounds are of interest, because molecular chemistry can define not only which atoms will be in the final film but also which atoms will not. One route to a carbon-free metal oxide film is to create that film from precursors containing no carbon. The use of anhydrous metal nitrates in the formation of high-κ dielectrics is a notable example.

Chapter 3 will detail the development of a fluidized bed precursor delivery system to address the unique challenges solid-phase precursors present to process control. Sublimation from powders suffers from temporal inhomogeneity of precursor flux due to continuously changing surface areas as the powders sublimate, an effect which is only exaggerated by the presence of any impurity on the surface and by contact between particles. Suspending the particles in a gas flow would negate contact between precursor particles and allow more intimate mixing of the particles with the gas. This would result in increasing the uniformity of chemical delivery due to the net increase of precursor surface as well as increased gas-precursor mixing leading to precursor vapor pressures which are closer to equilibrium values. A fluidized bed reactor can be employed to address this delivery issue by mixing inert powders of specific size and shape (fluidization medium) with chemical precursor powders and blowing gas vertically through the mixture. Under the correct conditions, the mixture of precursor and

fluidization medium enters a regime in which gas pockets roil to the top of the powder like water vapor in a boiling pot. By operating in this regime, an intimate mixing of carrier gas and precursor occurs, and the uniformity of precursor flux is increased. Delivery of uniform chemical flux enables consistent engineering applications of vapor deposition processes involving solid-state chemical precursors.

Ultimately, it is the chemical reactions that occur at or near the substrate surface that determine the nature of the deposit. Some source of energy must be provided to assist the chemical decomposition. This energy could be from a hot substrate, a plasma, a hot wire, a laser or from chemical potential energy due to reactivity between molecular species. Films of various microstructures and morphologies can be grown by CVD. Studying the effect that changes in temperature, pressure, and precursor flux have on the deposition process allows the correlation between deposition conditions and the stoichiometry and microstructure of the deposit formed on the surface. For example, amorphous materials will grow in low temperature ranges, while polycrystalline films will form at higher temperatures.

Rate differences between arrival of new precursor to the surface and decomposition of the surface molecules to create new reactive sites are important factors in the deposition process. When the reaction rate is high compared to the arrival rate, this is called the flux-limited regime, because the kinetic bottleneck of the deposition process is the arrival of precursor to the surface. When the decomposition rate is slower than the arrival of material to the surface, this is referred to as the reaction-limited regime. In the reaction-limited regime, the deposited films tend to be uniform in thickness, but they deposit more slowly, because the surface is filled with unreacted molecules waiting to decompose. In the flux-limited regime, film growth is limited by precursor arrival to the surface, because open reactive sites are readily available due to rapid precursor decomposition. This flux-limited deposition regime is typically faster than the reaction-limited regime, but thickness uniformity in the flux-limited zone of deposition is largely flux dependant.

The morphology of the deposit is dependant on precursor chemistry, hinging on molecule-dependant parameters such as nucleation energy, surface mobility of adsorbed

species and reaction kinetics to generate different surface features in different temperature regimes. The relationship of chemical kinetics and reaction thermodynamics with the underlying fluid and chemical dynamics of molecules arriving to the surface dictates the nucleation and growth behavior involved in the deposition process. Control over the roughness, crystallinity, texture and microstructure of a film allowed by properly selecting precursor chemistry and deposition conditions is advantageous to many applications.

Thin films can be grown by utilizing chemical reactions between precursor species instead of relying on precursor decomposition. Atomic layer deposition (ALD) is a subset of chemical vapor deposition in which alternating exposures of chemical precursors allows films to be grown via surface reactions. In ALD, the substrate on which a film is to be grown is exposed to vapors of a chemical precursor. The molecules irreversibly adsorb to the surface, and the adsorption process is limited by the number of chemical sites available. After surface saturation is achieved, the deposition chamber is evacuated of the remaining first precursor. A second precursor is then introduced into the system. A reaction between the first surface bound molecule and the second arriving molecule occurs, ultimately leaving a thin layer of deposited material and a saturated layer of the second precursor tenaciously bound to the new material surface. When repeated, a film is grown by the reaction between these two precursors, atomic layer by atomic layer.

Because of the growth mechanism of ALD, thickness control and uniformity on a near-molecular scale can be achieved. Flux dependence is minimized once the surface is filled with adsorbed molecules. Decomposition is largely negligible at the low temperatures employed in ALD, so adsorption of new molecules to the surface will not occur until the next precursor is introduced, where upon a reaction occurs between precursors allowing material to become incorporated into the growing film. Beyond achieving saturation, flux to the surface is not a major factor in film growth rate, and because of this behavior ALD excels at depositing uniform thickness films on substrates with complex morphologies and high aspect ratio features.

Chapter 4 will present the use of atomic layer deposition methodologies in

conjunction with combinatorial deposition techniques to form compositionally graded, uniform-thickness films with nanolaminate morphology. Surface saturation kinetics, thickness dependence on number of film cycles, and elemental profiles of the films are presented. X-ray reflection spectroscopy is used to examine the reflection of X-ray photons off of the film to reveal alternating layers of dielectric strength characteristic of nanolaminated materials.

Chapter 5 will present preliminary work done using computational fluid dynamics modeling of combinatorial chemical vapor deposition processes. Model design, molecular properties and reaction schemes are addressed and initial results are reported. Successful conclusion of the project remained elusive, however.

Control of film thickness, morphology, uniformity and composition by understanding all aspects of the route from molecular precursor to deposited film enables successful application of chemical vapor deposition techniques to real world products. By studying the molecular properties of precursor chemicals, refining delivery systems to address key concerns and mapping deposition processes over a range of conditions one can hope to address the successful control of film growth processes.

CHAPTER 2

Synthesis, Purification and Structural Analysis of $[NO]_{0.5}[NO_2]_{0.5}[Hf(NO_3)_5]$ and $[NO]_{0.5}[NO_2]_{0.5}[Zr(NO_3)_5]$

2.1. INTRODUCTION

Anhydrous metal nitrates were first described by Field and Hardy, who synthesized and described anhydrous zirconium nitrate in 1962.[1] The first review of anhydrous metal nitrates was written by Addison and Logan in 1966.[2] Anhydrous metal nitrates have been studied for potential use in microelectronics because of their utility in the formation of high κ dielectric materials.[3a-p] While the synthesis and use of anhydrous hafnium and zirconium nitrates has been reported by multiple authors, only a single crystal X-ray structure of the zirconium compound has been reported, though the authors mention the synthesis and analysis of an isotypic nitronium pentanitratohafnate compound.[4,5] The X-ray crystal structures reported by the previous authors indicated that the compound formed in the synthesis is not $Zr(NO_3)_4$, but rather $NO_2(NO_3)_3[Zr(NO_3)_5]_4$ or $NO_2[Zr(NO_3)_5]$ respectively. The synthesis performed in each case was identical, and also representative of the synthesis techniques used by others to create anhydrous metal nitrates. In this work, we describe the characterization of anhydrous hafnium nitrate and anhydrous zirconium nitrate, synthesized according to the Field and Hardy method of reacting metal halides with dinitrogen pentoxide, as a mixed N_2O_5 / N_2O_4 dissociated solvent adduct of $Zr(NO_3)_4$ and $Hf(NO_3)_4$.

2.2. EXPERIMENTAL

2.2.1. Synthesis and purification of $[NO]_{0.5}[NO_2]_{0.5}[Hf(NO_3)_5]$ and $[NO]_{0.5}[NO_2]_{0.5}[Zr(NO_3)_5]$

Anhydrous hafnium nitrate and anhydrous zirconium nitrate were synthesized according to a modified literature procedure by reacting dinitrogen pentoxide with the respective metal chlorides.[6] The resultant crude product was purified by repeated cycling of nitrogen at atmospheric pressure and vacuum in the reaction flask until no further colored gas, believed to be NO_2Cl, could be seen evolving from the crude product. The crude product was transferred to a cold-finger sublimator in a glove box. The sublimator

was evacuated and heated to 100° C, and the sublimator's cold finger was cooled to 0° C using an ethylene glycol/water solution running through a mechanical chiller. Sublimation was performed for 60 hours under static vacuum, with sublimated product collected from the cold finger after 12 hours, 36 hrs and 60 hrs. Crystals of sufficient size for X-ray analysis (approx. 1 mm^3) were found on top of the crude product when the cold finger was heavily covered with sublimed material and are believed to have fallen off the cold finger (see Results 2.3.1).

2.2.2. Infrared Absorption Spectroscopy

Infrared spectroscopy using Fluorolube mulls between KBr plates was performed on a Nicollet 560 IR spectrometer. 64 scans were averaged, and a resolution of one wavenumber was used. While in a glove box, the samples were ground with a corundum mortar and pestle and mixed with Fluorolube. The Fluorolube/sample mixture was spread on a KBr plate and another KBr plate was pressed onto the sample until the sample was semi-transparent. The sandwich was wrapped in parafilm and immediately transported to the spectrometer.

2.2.3. X-Ray Crystallography

For each compound, a crystal (approximate dimensions 0.30 x 0.30 x 0.20 mm^3) was placed onto the tip of a 0.1 mm diameter glass capillary and mounted on a Siemens SMART Platform CCD diffractometer for data collection at 173(2) K. A preliminary set of cell constants was calculated from reflections harvested from three sets of 20 frames. These initial sets of frames were oriented such that orthogonal wedges of reciprocal space were surveyed. This produced initial orientation matrices determined from 229 (hafnium sample) or 212 (zirconium sample) reflections. The data collection was carried out using MoKα radiation (graphite monochromator) with a frame time of 15 seconds and a detector distance of 4.919 cm (hafnium sample) or 4.996 cm (zirconium sample). A randomly oriented region of reciprocal space was surveyed to the extent of one sphere

Table 2.1. Crystal data and structure refinement for $[NO]_{0.5}[NO_2]_{0.5}[Hf(NO_3)_5]$ and $[NO]_{0.5}[NO_2]_{0.5}[Zr(NO_3)_5]$

Empirical formula	$N_6O_{16.50}Hf$	$N_6O_{16.50}Zr$
Formula weight	526.55	439.28
Temperature	173(2) K	173(2) K
Wavelength	0.71073 Å	0.71073 Å
Crystal system	Tetragonal	Tetragonal
Space group	$I4_1/a$	$I4_1/a$
Unit cell dimensions	a = 13.7210(7) Å α = 90°	a = 13.7209(7) Å α = 90°
	b = 13.7210(7) Å β = 90°	b = 13.7209(7) Å β = 90°
	c = 25.799(3) Å γ = 90°	c = 25.777(3) Å γ = 90°
Volume	4857.1(7) $Å^3$	4852.8(7) $Å^3$
Z	16	16
Density (calculated)	2.880 Mg/m^3	2.405 Mg/m^3
Absorption coefficient	8.714 mm^{-1}	1.030 mm^{-1}
F(000)	3936	3424
Crystal color, morphology	colorless, block	colorless, block
Crystal size	0.30 x 0.30 x 0.20 mm^3	0.30 x 0.30 x 0.20 mm^3
Theta range for data collection	1.68 to 27.49°	1.68 to 27.49°
Index ranges	$-17 \le h \le 17$, $-17 \le k \le 17$, $-33 \le l \le 33$	*same*
Reflections collected	28270	27914
Independent reflections	2786 [R(int) = 0.0290]	2780 [R(int) = 0.0262]
Observed reflections	2694	2603
Completeness to theta = 27.49°	100.0%	99.8%
Absorption correction	Multi-scan	Multi-scan
Max. and min. transmission	0.175 and 0.092	0.8205 and 0.7475
Refinement method	Full-matrix least-squares on F^2	*same*
Data / restraints / parameters	2786 / 4 / 223	2780 / 5 / 223
Goodness-of-fit on F^2	1.043	1.013
Final R indices [I>2sigma(I)]	R_1 = 0.0161, wR_2 = 0.0370	R_1 = 0.0305, wR_2 = 0.0708
R indices (all data)	R_1 = 0.0173, wR_2 = 0.0375	R_1 = 0.0328, wR_2 = 0.0720
Largest diff. peak and hole	0.406 and -0.592 $e.Å^{-3}$	0.317 and -0.382 $e.Å^{-3}$

and to a resolution of 0.77 Å. Four major sections of frames were collected with 0.30º steps in ω at four different φ settings and a detector position of -28º in 2θ. The intensity data were corrected for absorption and decay (SADABS). Final cell constants were calculated from the xyz centroids of 3726 (hafnium sample) or 3533 (zirconium sample) strong reflections from the actual data collection after integration (SAINT). A summary of additional refinement information and crystal data is given in Table 2.1.

The structures were solved using SHELXS-97 and refined using SHELXL-97. The space group $I4_1/a$ was determined based on systematic absences and intensity statistics for both compounds. A direct-methods solution was calculated which provided most non-hydrogen atoms from the E-map. Full-matrix least squares / difference Fourier cycles were performed which located the remaining non-hydrogen atoms. All non-hydrogen atoms were refined with anisotropic displacement parameters. The final full matrix least squares refinement converged to $R_1 = 0.0161$ and $wR_2 = 0.0375$ (F^2, hafnium sample, all data) and $R_1 = 0.0305$ and $wR_2 = 0.0720$ (F^2, zirconium sample, all data).

2.3. RESULTS

2.3.1. Infrared Spectroscopy

Infrared spectroscopy using Fluorolube mulls between potassium bromide plates showed no difference between the spectra of the crystals collected from the top of the crude product and the spectra of the cold-finger deposited product, confirming that the cold-finger product and the X-ray diffraction samples were chemically identical. Sharp absorption IR absorption peaks at 2731 cm^{-1} and 2300 cm^{-1} were assigned to nitronium and nitrosonium ions respectively. A high intensity split absorption with peaks at 1605 cm^{-1} and 1570 cm^{-1} were attributed to bidentate nitrate bonding. One sharp absorption peak at 2354 cm^{-1}, which was significantly less intense than the 2371 cm^{-1} and 2300 cm^{-1} absorption peaks, was unassigned.

2.3.2. X-ray Crystal Structures

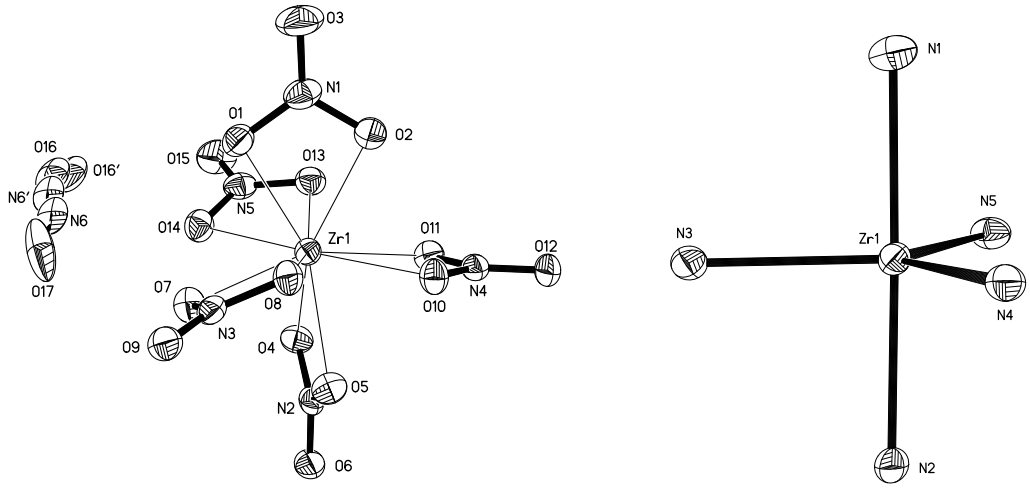

Figure 2.1. Pictures showing crystal structure of $[NO]_{0.5}[NO_2]_{0.5}[Zr(NO_3)_5]$ (left) and trigonal pyramidal arrangement of nitrate ligands around the central zirconium atom (right)

Figure 2.1 illustrates the arrangement of the nitrate ligands around the central zirconium atom and also shows a simplified picture of only the nitrogen atoms in the nitrate ligand around the central zirconium atom for the zirconium species. The hafnium species exhibited the same crystalline structure. The oxygen atoms of the nitrate groups are slightly twisted in orientation with respect to the trigonal bipyramidal structure, but the location of the nitrogen atoms in the compound confirms the molecular structure is indeed trigonal bipyramidal.

The modeled structures contain a 50:50 site occupancy between an NO_2^+ and NO^+ cation. The cations are located in channels in the lattice and appear to alternate between NO_2^+ and NO^+ along the channel as shown in Figure 2.2. When the NO^+ cation is left out, close contacts between oxygen atoms on the NO_2^+ cations generate fitting alerts. This further confirms the 50:50 mixed arrangement, because the cations would need to alternate between NO_2^+ and NO^+ to avoid close contacts. The NO^+ was modeled based on the IR evidence, and the knowledge that dinitrogen pentoxide synthesized from fuming nitric acid and phosphorus pentoxide contains high levels of dinitrogen tetroxide, which would dissociate into NO_3^- and NO^+.[7] Modeling without the NO^+ yields an R_1 of

Table 2.2. Atomic coordinates (x 10^4) and equivalent isotropic displacement parameters (Å^2 x 10^3) for $[NO]_{0.5}[NO_2]_{0.5}[Zr(NO_3)_5]$. U_{eq} is defined as one third of the trace of the orthogonalized U_{ij} tensor.

	x	y	z	U_{eq}
Zr1	1182(1)	5501(1)	1652(1)	20(1)
N1	1370(2)	6848(2)	2413(1)	32(1)
O1	1061(2)	7037(2)	1952(1)	30(1)
O2	1579(2)	5938(2)	2473(1)	35(1)
O3	1455(2)	7446(2)	2747(1)	51(1)
N2	953(2)	4157(2)	887(1)	24(1)
O4	1685(2)	4729(2)	919(1)	28(1)
O5	356(2)	4246(2)	1268(1)	29(1)
O6	832(2)	3594(2)	536(1)	33(1)
N3	-706(2)	6025(2)	1502(1)	24(1)
O7	-20(2)	6179(2)	1170(1)	30(1)
O8	-396(2)	5645(2)	1925(1)	25(1)
O9	-1544(2)	6213(2)	1417(1)	30(1)
N4	1552(2)	3907(2)	2279(1)	24(1)
O10	722(2)	4324(2)	2270(1)	26(1)
O11	2159(2)	4276(2)	1947(1)	26(1)
O12	1755(2)	3248(2)	2559(1)	32(1)
N5	2670(2)	6551(2)	1209(1)	29(1)
O13	2747(2)	5936(2)	1588(1)	29(1)
O14	1803(2)	6629(2)	1037(1)	30(1)
O15	3349(2)	7007(2)	1045(1)	44(1)
N6	1575(8)	8093(16)	379(13)	47(3)
O16	2311(8)	8451(16)	359(18)	53(3)
O17	779(6)	7904(6)	411(2)	69(2)
N6'	1728(9)	8314(18)	434(13)	47(3)
O16'	2526(8)	8298(16)	392(18)	53(3)

Table 2.3. Atomic coordinates (x 10^4) and equivalent isotropic displacement parameters (Å^2 x 10^3) for $[NO]_{0.5}[NO_2]_{0.5}[Hf(NO_3)_5]$. U_{eq} is defined as one third of the trace of the orthogonalized U_{ij} tensor.

	x	y	z	U_{eq}
Hf1	8817(1)	5506(1)	6651(1)	20(1)
N1	9045(2)	4162(2)	5890(1)	24(1)
O1	8320(2)	4750(2)	5920(1)	27(1)
O2	9634(2)	4247(2)	6273(1)	27(1)
O3	9160(2)	3599(2)	5539(1)	32(1)
N2	8635(2)	6850(2)	7409(1)	30(1)
O4	8942(2)	7036(2)	6947(1)	28(1)
O5	8431(2)	5943(2)	7468(1)	33(1)
O6	8556(2)	7450(2)	7740(1)	48(1)
N3	7332(2)	6561(2)	6210(1)	29(1)
O7	8199(2)	6636(2)	6036(1)	29(1)
O8	7264(2)	5944(2)	6589(1)	28(1)
O9	6648(2)	7009(2)	6047(1)	43(1)
N4	8452(2)	3911(2)	7273(1)	22(1)
O10	7851(2)	4287(2)	6939(1)	25(1)
O11	9282(2)	4329(2)	7269(1)	26(1)
O12	8246(2)	3244(2)	7553(1)	32(1)
N5	10697(2)	6022(2)	6499(1)	24(1)
O13	10014(2)	6170(2)	6166(1)	27(1)
O14	10387(1)	5648(2)	6924(1)	24(1)
O15	11537(2)	6210(2)	6415(1)	29(1)
N6	8406(8)	3101(18)	4620(14)	46(3)
O16	7660(12)	3440(30)	4620(30)	57(3)
O17	9205(5)	2925(5)	4589(2)	62(2)
N6'	8268(9)	3324(19)	4571(14)	46(3)
O16'	7475(12)	3310(30)	4640(30)	57(3)

Table 2.4. Selected bond lengths (Å) and angles (°) for $[NO]_{0.5}[NO_2]_{0.5}[Hf(NO_3)_5]$ and $[NO]_{0.5}[NO_2]_{0.5}[Zr(NO_3)_5]$

Hf(1)-N(2)	2.701(3)	Zr(1)-N(1)	2.707(3)
Hf(1)-N(5)	2.704(2)	Zr(1)-N(3)	2.717(3)
Hf(1)-N(1)	2.712(2)	Zr(1)-N(2)	2.719(3)
Hf(1)-N(3)	2.747(3)	Zr(1)-N(5)	2.748(3)
Hf(1)-N(4)	2.759(2)	Zr(1)-N(4)	2.766(3)
N(2)-Hf(1)-N(5)	90.84(8)	N(1)-Zr(1)-N(3)	90.74(8)
N(2)-Hf(1)-N(1)	178.70(8)	N(1)-Zr(1)-N(2)	178.77(9)
N(5)-Hf(1)-N(1)	87.88(7)	N(3)-Zr(1)-N(2)	88.03(8)
N(2)-Hf(1)-N(3)	82.60(8)	N(1)-Zr(1)-N(5)	82.70(8)
N(5)-Hf(1)-N(3)	120.63(8)	N(3)-Zr(1)-N(5)	120.68(8)
N(1)-Hf(1)-N(3)	98.26(8)	N(2)-Zr(1)-N(5)	98.03(8)
N(2)-Hf(1)-N(4)	95.95(8)	N(1)-Zr(1)-N(4)	95.68(8)
N(5)-Hf(1)-N(4)	117.78(7)	N(3)-Zr(1)-N(4)	117.88(8)
N(1)-Hf(1)-N(4)	84.43(7)	N(2)-Zr(1)-N(4)	84.80(7)
N(3)-Hf(1)-N(4)	121.59(8)	N(5)-Zr(1)-N(4)	121.43(8)

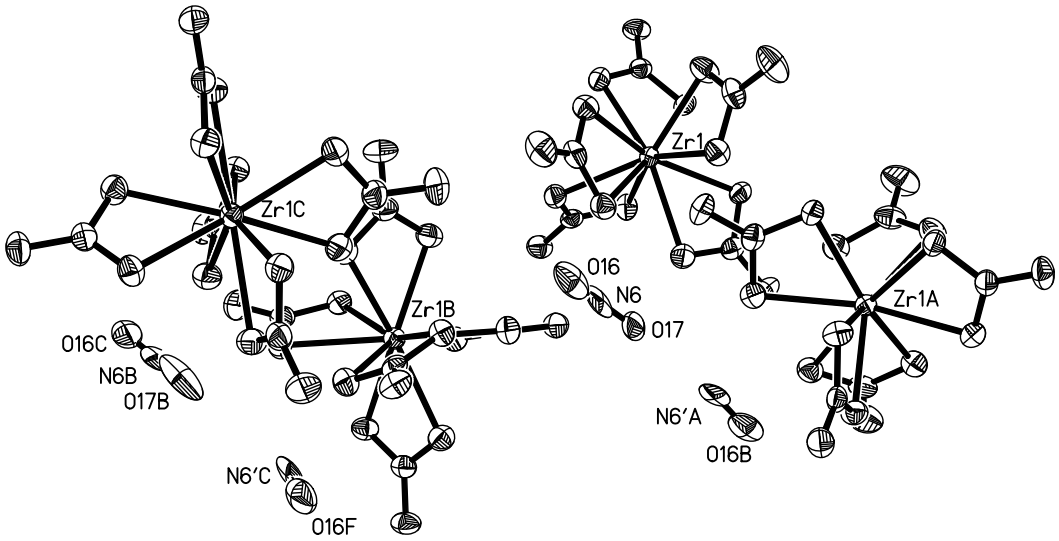

Figure 2.2. Picture showing alternating NO^+ and NO_2^+ cations

0.0183 and a wR_2 of 0.0529 (F^2, all data) for the hafnium species and an R_1 of 0.0344 and a wR_2 of 0.0897 (F^2, all data) for the zirconium species. Despite large thermal ellipsoids, attempts to model the NO_2^+ as disordered over two positions were unsuccessful.

2.4. DISCUSSION

Field and Hardy describe the product of the reaction of $ZrCl_4$ with N_2O_5 as a dissociated solvent adduct of an impure N_2O_5 solvent with $Hf(NO_3)_4$.[8] The formula they reported was $Zr(NO_3)_4 \cdot (0.4\ N_2O_5\ \ 0.6\ N_2O_4)$. It is mentioned in their paper that the coordinated solvent was lost after 4 hours at 0.01 mmHg and 100 °C, though Tikhomirov *et al.* report the preservation of the solvent adduct while purifying by sublimation under dynamic vacuum.[9] In another publication, Field and Hardy report the formation of the hafnium analog $Hf(NO_3)_4 \cdot N_2O_5$.[10]

The X-ray crystal structures presented herein show a trigonal bipyramidal arrangement of bidentate nitrate groups around a central metal atom for the zirconium compounds. The hafnium compound exhibits the same ligand arrangement. Bonding to the central metal atom weakens the nitrogen-oxygen interactions, creating two different bond lengths in the formally symmetric nitrate molecule. This asymmetry creates two different vibration frequencies. Separate infrared absorption peaks at 1605 cm^{-1} and 1570 cm^{-1} support the bidentate classification of the nitrate anions.[11,12]

The single crystal X-ray crystallography results clearly indicate five nitrate groups are coordinated to the central metal atom, but what is not so clear is the nature of the cation that must exist for charge balance. It is extremely likely that the solvent adducts of both the dinitrogen pentoxide and the dinitrogen tetroxide molecules exist as dissociated ion pairs creating NO_3^- anions balanced with either NO^+ or NO_2^+ cations. This behavior is probable, given the known solid-state structure of N_2O_4 which exists as $(NO^+)(NO_3^-)$.[13] Adducts of dinitrogen tetroxide (and presumably dinitrogen pentoxide) with metal nitrates are known to be stabilized by the formation of a nitrosonium (or nitronium) salt

of a nitrato-complex anion, such as in the case of $(NO^+)[Fe(NO_3)_4]^-$.[14] The infrared absorption peaks at 2731 cm^{-1} and 2300 cm^{-1} were assigned to nitronium and nitrosonium respectively, which matched literature reports. Both absorptions are strong, and the presence of two peaks supports the hypothesis that both cations are found in the crystalline compound. This spectral evidence strengthens the crystallographic interpretation that both compounds are mixed solvent adducts of N_2O_5 and N_2O_4.

2.5. CONCLUSION

For anhydrous zirconium and hafnium nitrates synthesized according to literature reaction of metal chloride with dinitrogen pentoxide, the formula $M(NO_3)_4$ is erroneous. The crystals grown during static vacuum sublimation are not molecular solids as previously believed but are ionic solids of the formulas $[NO]_{0.5}[NO_2]_{0.5}[Hf(NO_3)_5]$ and $[NO]_{0.5}[NO_2]_{0.5}[Zr(NO_3)_5]$. The presence of both NO^+ and NO_2^+ cations in the crystal structure is supported by the observation of appropriate infrared absorption peaks at 1605 cm^{-1} and 1570 cm^{-1}. X-ray crystal structures show a five ligand coordination sphere including ten metal-oxygen bonds from five bidentate nitrate ligands. Infrared spectral evidence supports the assignment of bidentate nitrate ligands, because the sample exhibited two separate absorption peaks at 2731 cm^{-1} and 2300 cm^{-1}.

CHAPTER 3

Aluminum Trichloride Sublimation and Delivery using a Fluidized Bed Reactor

3.1. INTRODUCTION

Chemical vapor deposition using precursors that are solids at operating temperatures and pressures presents challenges due to their relatively low vapor pressures. In addition, the sublimation rates of solid state precursors in fixed bed reactors change with particle and bed morphology. This paper discusses the use of fluidized bed technology to provide a high flux of solid state precursor in an engineering application.

The use of a fluidized bed reactor to study the sublimation behavior of aluminum triacetylacetonate [$Al(acac)_3$] with alumina (Al_2O_3) support has been reported.[15] Aluminum trichloride ($AlCl_3$) is a less expensive alternative Al source that is used extensively in industry to deposit aluminum oxide and aluminum nitride. This paper will present the fluidization study of $AlCl_3$ with Al_2O_3 support and the mass transfer of $AlCl_3$ under typical fluidization conditions and is supported by reports in literature.[16,17]

3.2. EXPERIMENTAL

3.2.1. Materials

Aluminum trichloride was used as received from Aldrich (99.99% purity). Alumina powder was sieved for at least 10 minutes on an 80 micron ASTM sieve.[18] Any alumina fines smaller than 80 microns were disposed of. Additional details of alumina granulometry as well as details of reactor geometry and construction can be found in a previous report.[19] The fluidized bed reactor was modified by the addition of a 5 micron sintered stainless steel filter, shown in Figure 3.1, fitted into a KF50 retainer ring and mounted at the exit of the reactor.

Figure 3.1. 5 micron stainless steel filter shown inside KF50 retainer ring with O-ring gasket (ring and gasket are sitting on a KF50 flange)

3.2.2 Reactor operation

To begin each experiment, 601.5 g of sieved alumina was loaded into the fluidized bed reactor through an access port in the top of the reactor. This alumina formed the bulk of the fluidized bed. Typically, 2-3 hours were required to preheat the fluidized bed reactor to operating temperatures. Reactor conditions are shown in Table 3.1. All measurements of bed and internal reactor temperature were conducted using a

Table 3.1 Operating conditions for fluidized bed reactor

	Fluidization	Mass Transfer Run 1	Mass Transfer Run 2	Mass Transfer Run 3
Temperatures (°C):				
-Serpentine	100	100	100	100
-Fluidized bed	107	107	107	107
-Expansion cone	112	111	111	110
-Expansion cylinder	113	112	113	112
-Top of reactor	113	113	112	112
-Filter	115	114	116	115
Nitrogen Mass Flow Rate (sccm)	Variable	6651	7529	8412
Aluminum trichloride mass loaded (g)	10.02	10.06	10.00	10.00
Total bed mass (g) (precursor + support)	621.5	621.6	621.5	621.5
Time of trapping (min)	N/A	20.00	20.00	20.00
Time of second trapping (min)	N/A	10.00	N/A	N/A
Time of third trapping (min)	N/A	10.00	N/A	N/A

type-K thermocouple inserted down a narrow tube that extended from the top of the reactor to halfway into the bed (in fixed mode). The thermocouple was raised and lowered to the appropriate position and the temperature recorded. The temperature of the filter was measured using an alcohol thermometer. During preheating, the alumina bed was dried by operating above 100 °C for at least one hour with dry nitrogen flowing through the bed at a minimum of 5,000 standard cubic centimeters per minute (sccm). An additional 10.0 grams of sieved alumina was dried under vacuum for at least 4 hours and transfered into a glove box in a sealed container. In the glove box, 10.0 g of aluminum trichloride was added to the 10.0 g of alumina, thoroughly mixed, poured into a precursor loading vessel (Figure 3.2), sealed and removed from the glove box.

3.2.3. Fluidization study

In order to determine fluidization conditions, measurements of pressure drop from the entrance of the reactor to the exit of the reactor (across the fluidization bed) were performed for various flow rates. The pressure drop was measured from the nitrogen inlet below the bed to the top of the expansion cylinder. The reactor was preheated to operating conditions. After temperature stabilization, the precursor vessel was mounted onto a KF25 flange on the top of the reactor. Nitrogen was run through the reactor for several minutes after mounting the precursor vessel to purge oxygen and moisture, and then the precursor / alumina mixture was introduced into the reactor. To prevent additional exposure to atmosphere, the precursor vessel was left attached to the reactor for the remainder of the experiment. To insure good mixing of the aluminum trichloride and the alumina

Figure 3.2. Precursor loading vessel for protecting reactive precursors from atmosphere (scale - bottom flange is KF25)

bed, nitrogen was flowed for 1 minute at approximately 7,000 sccm (bed fluidization conditions) before data collection began. Pressure drop data were collected from low flow (fixed bed conditions) through high flow (fluidized bed conditions) and back to low flow. Cold traps were used for this experiment to collect the aluminum trichloride and prevent the corrosive gas from exhausting to atmosphere. Because of the difference in coefficient of thermal expansion for glass and Teflon, it is important to rotate the stopcocks on the traps every 10 minutes during heating or cooling of the traps.

3.2.4. Mass transfer versus flow rate study

Experiments were performed to determine the experimental mass transfer of aluminum trichloride out of the fluidized reactor as a function of flow rate. In order to prevent release of aluminum trichloride into the atmosphere and also to trap the precursor for a known amount of time, a two way bypass was constructed (Figure 3.3). The effluent of each timed mass transfer run was trapped with 2 consecutive traps. The first trap was a dry, cold trap (Figure 3.4) filled with small pieces of glass tube (outer diameter

Figure 3.3. Trapping set-up showing bypass line (behind, dark dewer) and mass transfer trapping line (closer, light dewer and bubbler trap on right)

approximately 6 mm, inner diameter approximately 3 mm, length approximately 2 cm) and cooled to -45 °C with an ethanol / liquid nitrogen bath. The glass tubing served to increase the surface area of the cold trap. The second trap was a bubbler style trap filled approximately one-third full with pure water. Any residual $AlCl_3$, which passed through the first trap, would react with the water in the second trap (Figure 3.5). The bypass line consisted of one cold trap, kept at -45°C with an ethanol / liquid nitrogen bath. Using heating tape, the lines running from the reactor to the traps were heated to a slightly higher temperature (about 2 °C) than the filter in order to prevent precursor condensation before the traps.

The reactor was pre-heated to operating temperatures listed in table 3.1. After temperature stabilization, the precursor loading system was mounted to the top of the reactor. Dry nitrogen was flowed for several minutes before precursor introduction to remove oxygen and water vapor from the reactor. Temperatures at the various heights in the reactor were recorded using a thermocouple gauge. When beginning an experiment, gas flow was stopped, and the precursor/alumina mixture was introduced into the reactor. No evidence of reaction between aluminum trichloride and moisture in the reactor was observed upon the introduction of the alumina / aluminum trichloride. The precursor introduction system was left mounted on the reactor for the duration of the experiment to prevent introduction of atmospheric contaminants. Gas flow was restarted at the chosen flow rate. During the time after precursor introduction and before the mass transfer trapping, the reactor effluent was routed through the bypass

Figure 3.4. Dry, cold trap filled with small glass tubing pieces (scale – flange shown on right is KF50)

line. Within 5 minutes of precursor introduction, the flow of gas from the reactor was diverted through the measurement line and the mass transfer experiment began. A stopwatch was used to determine exactly 20 minutes of trapping, after which the reactor effluent was once again directed through the bypass line. The product trapped in the analysis traps was analyzed according to the $AlCl_3$ mass transfer analysis protocol which will follow.

3.2.5. Mass transfer versus time study

An experiment to determine the mass transfer of aluminum trichloride as a function of time was performed. After reactor initiation as described above, an initial sample was collected for 20 minutes. Then the reactor effluent was temporarily diverted through the by-pass line, and the cold trap was removed and replaced with a clean cold trap. The bubbler was emptied of its contents (which were saved for later analysis), rinsed with clean DI water, refilled to the prescribed mark and replaced on the reactor line, thus resetting the trapping system for another collection. A second quantification of aluminum trichloride flux occurred from 21-31 minutes (10 minute duration). The trap replacement procedure was followed again, and a third trapping of aluminum trichloride was made from 47-57 minutes (10 minute duration). All three samples were analyzed for chloride content.

Figure 3.5. Bubbler style trap

3.2.6. $AlCl_3$ mass transfer analysis

At the end of a trapping experiment, the cold trap was removed from the ethanol / liquid nitrogen bath and immersed in an ice water bath. The aluminum trichloride in the cold trap was carefully hydrolyzed using chloride-free de-ionized water. The solution from the cold trap was added to the solution in the bubbler which then accounted for all precursor trapped for the run. The resultant solution was diluted using chloride-free DI water to 1.00 L in a volumetric flask (solution A). 20.00 ml of solution A was diluted to 250.0 ml in a volumetric flask using chloride-free DI water (solution B).

Approximately 1.0 ml (20 drops) of 0.5 M K_2CrO_4 was added to 20.00 ml of solution B in a 50.0 ml Erlenmeyer flask and then titrated by 0.010 M $AgNO_3$ (aq) to a slightly orange endpoint.[20] If the volume of titrant added was less than 3.0 ml, another titration was performed on the more concentrated solution A to provide higher accuracy of titration. At least three titrations were performed for each sample, and less than 2% difference between titrations was observed.

3.3. RESULTS AND DISCUSSION

3.3.1. Fluidization study

Figure 3.6 shows the pressure drop across the fluidized bed as a function of gas velocity for both increasing and decreasing velocities. There are two linear regions shown in Figure 3.6, one at high velocities (greater than 0.07 m/s) and one at low velocities (less than 0.04 m/s). The intersection of the linear extrapolation of these two regions gives the minimum fluidization velocity (U_{mf}). From this data, U_{mf} was determined to be 0.052 m/s. The theoretical maximum pressure was calculated from the weight of the fluidized bed. The pressure drop across the bed was always less than the theoretical maximum.

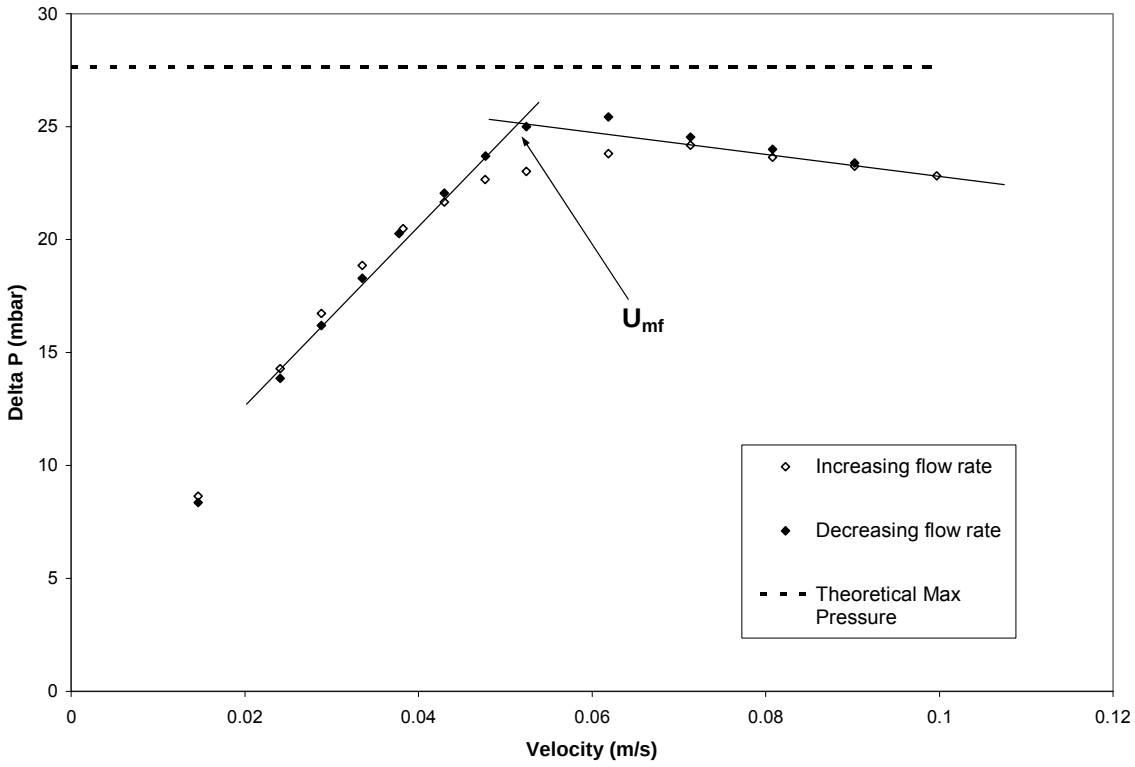

Figure 3.6. Pressure drop across reactor bed versus velocity of nitrogen through bed

3.3.2. Mass transfer versus flow rate

Figure 3.7 shows the graph of aluminum trichloride mass flow rate as a function of gas velocity. The theoretical mass transfer rate in Figure 3.7 was calculated using vapor pressure data for aluminum trichloride[21] along with the nitrogen mass flow rate corresponding to a given gas velocity. For the theoretical calculation, it was assumed that precursor sublimation from the bed was the only contributor to precursor flux. The experimental measurements at velocities of 0.0713 m/s, 0.0808 m/s and 0.0902 m/s correlated to 1.4 U_{mf}, 1.6 U_{mf} and 1.73 U_{mf} respectively, thus the bed was fluidized for all three points.

The experimental data are above the predicted values based on the equilibrium vapor pressure of $AlCl_3$ at 107 °C. There are two possible explanations for the higher than predicted aluminum trichloride mass flux values. The first pertains to particles of $AlCl_3$ that might pass through the filter. While there was no observation of aluminum

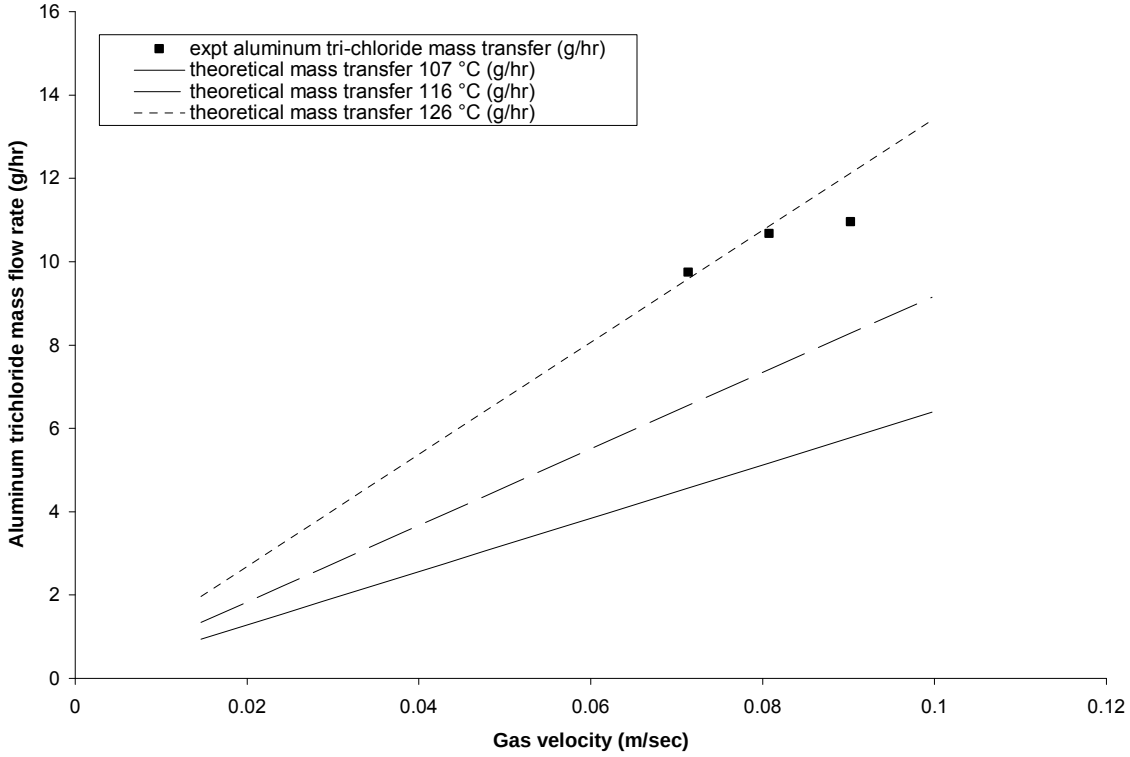

Figure 3.7. Graph of precursor mass flow rate versus gas velocity showing theoretical precursor mass flow rate values for bed temperatures of 107, 116 and 126 °C

trichloride particles downstream of the filter, it is likely that they would be sublimed on the path to the traps, due to the slighter higher temperatures in the effluent lines compared to the reactor.A second explanation for the high mass measurement is the lack of adequate thermal regulation of the reactor. The vapor pressure of aluminum trichloride is sensitive to temperature near the bed temperature (107 °C). At 107 °C, the vapor pressure of aluminum trichloride is 1.43 Torr, but at 117 °C the vapor pressure is 2.13 Torr, a nearly 50% increase. Localized heating of the reactor walls due to the use of heating tape might also give rise to higher local temperatures not reflected in the thermocouple measurements. A calculation was made to determine the theoretical temperature necessary to achieve the mass flux of each experimental data point. From lowest velocity to highest, the necessary temperatures were 126 °C, 126 °C and 123 °C, indicating a mass flux which is higher than predicted by the reactor temperature. During an experiment, the highest measured temperature (116 °C) at any location occurred at the filter.

3.3.3. Mass transfer versus time

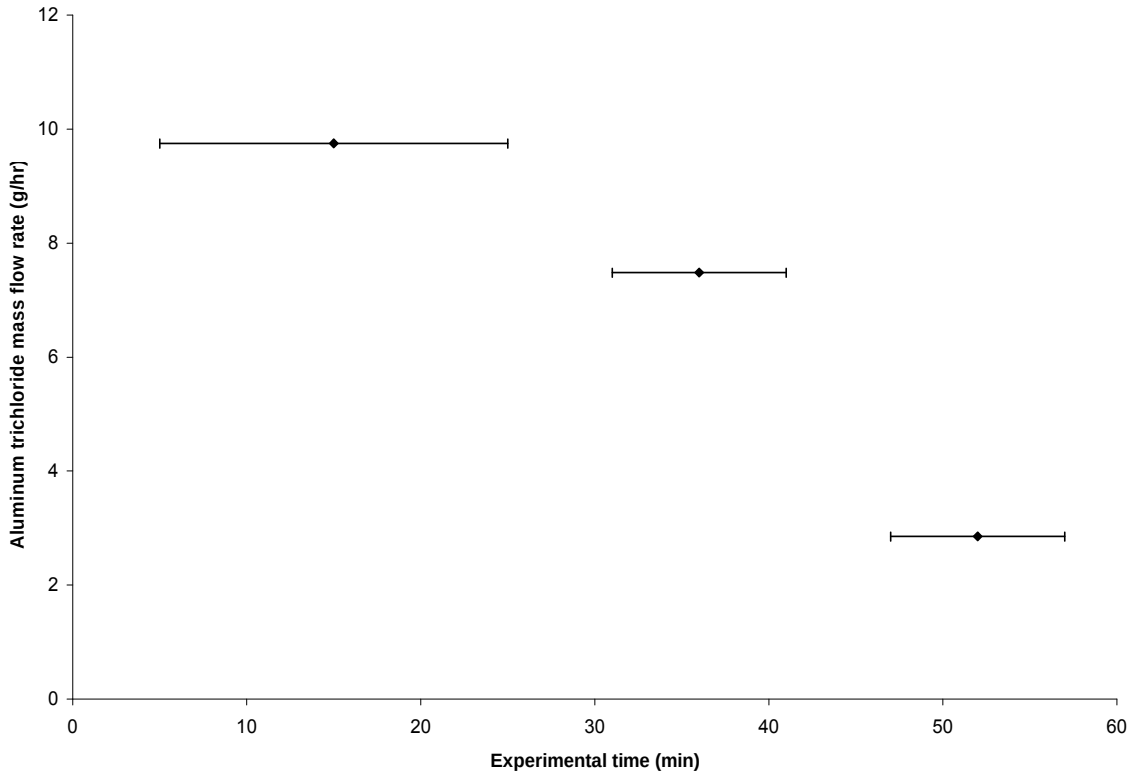

Figure 3.8. Mass transfer of aluminum trichloride out of reactor as a function of effluent time. Whiskers represent duration of trapping for each data point.

Figure 3.8 shows three measurements of trapped aluminum trichloride as a function of time. The horizontal bars represent the duration of each trapping; the first point was 20 minutes, but the other points were both collected for 10 minutes. The mass flow rate of precursor from the reactor decreases as $AlCl_3$ is consumed. The loading of precursor (10.0 g) was taken from previous reports and calculated to be sufficient for a 3.6 g/hr mass flow rate.[22] If the precursor mass flow rate were 3.6 g/hr, then the reactor could run for nearly three hours before the amount of aluminum trichloride was used up. Because the initial observed mass flow rate (9.75 g/hr) was substantially higher than the anticipated mass flow rate (3.6), the reactor's operating period was greatly reduced.

The experimentally measured precursor mass flow rate drops off substantially over the first hour of the experiment. In order to have a steady mass flow rate of precursor out of the reactor, one potential remediation for this situation would be to increase the initial

charge of aluminum trichloride. Because the aluminum trichloride is a very small percentage of the mass of the fluidized bed (10.0 g in 621.5 g), it is not expected that a doubling or even tripling of the precursor loading would substantially affect the fluidization behavior of the reactor. By increasing the initial loading of precursor in the reactor, a longer steady state period would be expected. Another potential improvement would be to run the reactor in a continuous process, rather than a batch mode. If precursor were constantly added to the reactor at the same rate the precursor were removed from the reactor, constant steady state operation could be achieved. Because of the construction of the reactor with an easily accessible precursor delivery port, all that would be required for continuous operation would be the creation of a precursor vessel designed for such a purpose.

3.4. CONCLUSION

It has been demonstrated that the fluidized bed reactor in this study is capable of exceeding the 3.6 g/hr target for aluminum trichloride delivery. Precursor mass flow rates of 9.75 to 10.96 g/hr have been observed for carrier gas (nitrogen) flow rates of 6649 – 8418 sccm. Improvements in reactor performance may be achieved by better thermal regulation of the system, increased initial precursor charging, and through continuous precursor addition during operation of the reactor to prevent depletion.

CHAPTER 4

Atomic Layer Deposition of Compositionally Graded $(HfO_2)_x(ZrO_2)_{1-x}(SiO_2)_{6.5}$ Nanolaminate Films

4.1. INTRODUCTION

Combinatorial chemistry found its roots in the desire to evaluate a wide palate of chemical possibilities by simultaneously creating a distribution of synthetic products. The variety of materials or compounds formed can then be evaluated for the desired properties or effects. Granted a sufficient measurement resolution, analyzing a sample with a graduated composition is often more efficient than analyzing several samples with discrete compositions due to, amongst others, practical concerns such as sample mounting and vacuum pumping time. Additionally, the production of an entire repertoire of target compounds enables the serendipitous revelation of unknown chemical products.

While seemingly advantageous, combinatorial methods were not immediately adopted by the wider scientific community. Two early developers of combinatorial methods were Merrifield, who applied parallel synthesis to peptide chemistry in the 1960's, and Hanak, who developed a co-sputtering technique at RCA in the 1970's.[23,24] Hanak eventually studied many materials including superconductors, light emitting diodes, amorphous silicon, and magnetic recording media. Takeuchi, Lauterbach and Fasolka have written a broad review of combinatorial materials synthesis which discusses a range of applications from microelectronics to polymer systems and methods from experimental design to high-throughput measurement techniques.[25]

Combinatorial research requires great amounts of data to be processed in order to thoroughly explore the materials system. Possibly due to the increasing ubiquity of personal computing, the late 1990's saw combinatorial methods become more widely incorporated into multiple active research groups. In 1995, Xiang and coworkers at Lawrence Berkeley National Laboratory reported their application of combinatorial methods to multi-component high-temperature superconductors and the magneto-resistant cobalt based compounds.[26,27] They achieved spatially addressable parallel synthesis by sputtering using masks and then sintering the thin films before analyzing the electronic properties of the materials. The libraries Xiang *et al*. created contained arrays of discrete samples, each with essentially uniform composition, which mapped out a wide synthesis space of potential compounds. Three years later, van Dover *et al*. reported the

creation a zirconium-tin-titanium oxide thin film compositional palate using off-axis sputtering to form continuous compositional gradients.[28]

The break of the new century saw combinatorial methods applied to study material properties beyond composition. Hotwire chemical vapor deposition (CVD) utilizing a moving mask was employed by Wang and coworkers in the combinatorial study of phase transition in amorphous silicon oxide.[29] They were able to observe the effect of changing silane to hydrogen dilution and map the amorphous to microcrystalline transition in the deposited material. In 2001, Koinuma and coworkers produced multiple α-Si:H thin film transistors on a single substrate using plasma enhanced CVD and masks to create devices which were combinatorial in thickness.[30]

2002 was a boom year for thin film combinatorial science. Koinuma *et al.* report using pulsed laser molecular beam epitaxy and a movable mask to deposit compositionally varied $Ba_xSr_{(1-x)}TiO_3$ thin films on a silicon surface with a temperature gradient.[31] Ginley *et. al.* publish their work using sputtering and hotwire CVD methods to study aluminum and nitrogen doping in zinc oxide and the amorphous to microcrystalline transition in amorphous silica.[32] Previously developed micro hot plates were extended to high-throughput materials screening by Taylor and Semancik when they explored temperature space in the chemical vapor deposition of titanium dioxide.[33] These researchers and others have continued to produce work in combinatorial chemistry and lead productive research groups.[34a-o]

One significant advance beyond 2002 that should be mentioned is the development of a spatially programmable CVD apparatus designed and implemented by Adomatis and coworkers. [35a-f] The Adomatis reactor includes use of localized precursor inlet tubes, but adds to the design a series of hexagonal baffles which can be raised and lowered *in situ*. The advantage gained by such a design is the flexibility to create either wholly continuous elemental distributions (when the baffles are entirely raised) or multiple segments on the surface within which regions of relative homogeneity would be found. Continuous gradients can be created for rapid screening, but once target materials are achieved, the reactor can be programmed to create a few distinct homogeneous zones which can be used for further analysis and device fabrication.

Combinatorial chemistry in the Gladfelter research group began with a 2002 report on the use of combinatorial low-pressure chemical vapor deposition (combi-CVD) to explore the ternary system of hafnium-tin-titanium oxide as deposited from the anhydrous nitrates of hafnium, tin and titanium on silicon substrates.[36] One of the advantages to combinatorial screening is discovering unanticipated materials or phases. During the combi-CVD of films from anhydrous hafnium, zirconium and tin nitrates, an unpredicted α–PbO_2 phase was revealed and studied by Gladfelter and coworkers in the hafnium-zirconium-tin oxide thin film system.[37,38,39,40] Creating compositionally graduated films by chemical vapor deposition was enabled by the use of precursors with matched ligand systems. At typical CVD growth temperatures, gas phase reactions between different precursors are often facile and result in unwanted depositions and powder formation. Using precursors with matched ligand systems (such as the anhydrous metal nitrates) negates the effects of gas phase ligand exchange and prevented chemical interaction between the precursors. The deposits seen in the combi-deposition are in effect the sum of three individual depositions.

Unlike the previous work in the Gladfelter group, the combi-CVD of tris-*tert*-butoxy silanol with anhydrous zirconium or hafnium nitrate used precursors with mis-matched ligand systems.[41] The resulting films exhibited compositional variation but had two important differences from previous work. The materials deposited at a much lower temperature, and the topography of the deposit was completely different. Instead of the film forming as the sum of the individual depositions, a relatively large film grew between the precursor inlets at conditions for which no growth of the individual precursors would be expected. This indicated that deposition was a result of chemical interaction between precursor species. The chemical reactivity exhibited in this system lead the researchers to apply atomic layer deposition techniques to create thin films of zirconium or hafnium silicates.[42,43]

Atomic layer deposition (also referred to as alternating layer deposition – both abbreviated ALD) is a process by which extremely uniform, conformal thin films are formed on surfaces by alternating exposure of two (or more) chemical precursors. Puurunen has written a review discussing the history of ALD, materials systems

explored, precursor chemistries and the mechanism of ALD as taught through the case study of trimethylaluminum and water.[44] Additionally, Musgrave and Gordon have published an article discussing the requirements for ALD precursors for high-κ dielectrics.[45] ALD processing requires vacuum equipment with high pumping capacity, and the deposition rate is limited compared to other film routes such as evaporation, sputtering, or chemical vapor deposition. However, thickness control to near atomic precision and uniformity over complex substrate morphologies with high aspect ratios makes the technique appealing.

The critical feature of ALD is self-limiting reactant exposure cycles leading to self-limiting repeatable deposition cycles. A single exposure consists of a dose of precursor 1 and an evacuation of any remaining gas-phase precursor 1. This would be followed by an exposure to the second precursor (precursor 2) and subsequent evacuation of that precursor. Any additional exposures may be included here, and the sequence of exposures: [dose 1 / evac / dose 2 / evac / dose 3 / evac...] is counted as one atomic layer deposition cycle.

The deposition temperature window of ALD is usually lower than that of the corresponding chemical vapor deposition process. ALD occurs in a range of thermal conditions limited on the high end by precursor decomposition and on the low end by condensation/multilayer adhesion. Within the ALD window a tenaciously adsorbed film of unreacted precursor is left behind after each dose / evacuation cycle, and the amount of precursor adhered to the surface is limited by the number of available adsorption sites. The conversion to solid film happens with the following exposure, where the next precursor chemically interacts with the adsorbed compound. The chemical reaction between molecules results in the production of the target material, and the continuing flux of precursor after the initial surface reaction allows the growing surface to be regenerated as a precursor-saturated layer. This surface regeneration is critical to ALD, and it allows multiple cycles of precursor exposure to be built upon one another.

A linear relationship of film thickness to number of ALD cycles shows each deposition cycle is independent of the previous cycle. This property of ALD allows control over deposited film thickness based simply on the number of deposition cycles.

As previously mentioned, another criterion for an ALD process is self-limiting deposition. As precursor dose increases from extremely small pulses to larger ones, an initial increase of deposition rate is observed. At some critical precursor dose, the deposition per cycle becomes constant and independent of precursor dose. This is the surface saturation point. Below surface saturation, increasing precursor dose will lead to increased deposition. Beyond surface saturation, increasing precursor dose will not lead to increased surface loading, because the surface is already completely packed with adsorbed molecules. In these conditions, additional molecules arriving to the surface will not remain attached and will be removed during the evacuation cycle.

Atomic layer deposition inherently creates uniform thickness films. One drawback of previous work in combi-CVD was the wide variety of film thicknesses which accompanied the variety of film compositions. Any property which might include a thickness dependence would be difficult to evaluate because of the convolution of thickness and material property. The extension of compositional gradient deposition techniques to ALD methods allows the creation of thin films with both elemental variation and uniform thickness.

To the author's best knowledge, there are no reports of atomic layer deposition using the combination of hafnium tetrakis-*tert*-butoxide (HTB) and tris-*tert*-butoxy silanol (tBOS) or the combination of zirconium tetrakis-*tert*-butoxide (ZTB) with tris-*tert*-butoxy silanol (tBOS). Tris-*tert*-butoxy silanol has been widely studied as an ALD reactant and has been shown to undergo self-limited chemical vapor deposition near room temperature.[46a-g] Literature reports the ALD reaction of HTB with tetrakis-ethylmethylaminosilane [$Si(N(CH_3)\text{-}(C_2H_5))_4$], ozone and plasma activated oxygen.[47a-d] The published work available for ZTB is slightly more extensive, including ALD of ZTB with water, oxygen, plasma activated oxygen, nitrous oxide and plasma activated argon.[48a-m] In related chemistry, Tilley and coworkers have synthesized the tris-*tert*-butoxysiloxy complexes $Zr[OSi(O^tBu)_3]_4$ and $Zr[OSi(O^tBu)_3]_4$ as single molecule precursors to $ZrO_2{\cdot}4SiO_2$ and $HfO_2{\cdot}4SiO_2$ materials.[49,50] These compounds exhibited thermo-gravimetric analysis decomposition temperatures similar to the experimental conditions described herein and thus should provide predictive analogs to the reactivity of

the surface species formed during the ALD of tris-*tert*-butoxy silanol with either zirconium tetrakis-*tert*-butoxide or hafnium tetrakis-*tert*-butoxide.

The only combinatorial ALD reports the author is aware of is the work of Rubloff and coworkers.[51,52,53] Rubloff has developed an ALD reactor which utilizes cross-flow of the reactant chemicals across the surface of the silicon wafer to create films which are combinatorial in precursor exposure. Thickness gradients were created by operating in the sub-saturation regime where increasing precursor dose affects film growth rate. Enhancement and depletion effects were observed by holding one reactant pulse fixed and varying the other reactant pulse. Rubloff was able to correlate the varying thickness profiles of the deposited films with precursor doses from sub-saturation through saturation conditions. The thickness profiles and properties of the deposited films were combined with records of real-time mass spectrometry data to allow rapid evaluation of ALD precursor dose recipes.

The creation of combinatorial, compositionally graduated, uniform thickness films by atomic layer deposition of hafnium tetrakis-*tert*-butoxide and zirconium tetrakis-*tert*-butoxide, simultaneously co-dosed from separate localized sources, followed by a tris-*tert*-butoxy silanol second dose (counter-reagent dose) is reported herein. The establishment of an ALD-mode deposition of these precursor systems along with measurements of elemental profiles and demonstration of alternating atomic microstructure follows.

4.2. EXPERIMENTAL

4.2.1. Depositions

A combinatorial low-pressure chemical vapor deposition reactor (Figure 4.1, described in detail elsewhere[54,55]) with computer-actuated pneumatic valves controlling the precursor dosing and purge gas flow was used to perform combinatorial atomic layer depositions (combi-ALD). A schematic of a typical pulse sequence is shown in Figure 4.2. One ALD cycle is composed of multiple precursor pulses. Each pulse consists of a

precursor dose (D) and an evacuation cycle (E). Each dose introduces either a single precursor (in the case of a two component deposition) or two precursors (in the case of a combi-experiment) simultaneously into the reactor. The following evacuation introduces clean nitrogen into the reactor to remove any excess unreacted precursor. Zirconium tetrakis-*tert*-butoxide (ZTB), hafnium tetrakis-*tert*-butoxide (HTB) and tris-*tert*-butoxy silanol (tBOS) were co-dosed from separate precursor vessels and through separate delivery lines. The precursors were introduced into the reactor through individual small stainless steel inlet tubes located above and perpendicular to the infrared susceptor (hot plate) such that the substrate surface was simultaneously exposed to a continuous partial pressure gradient of each precursor.

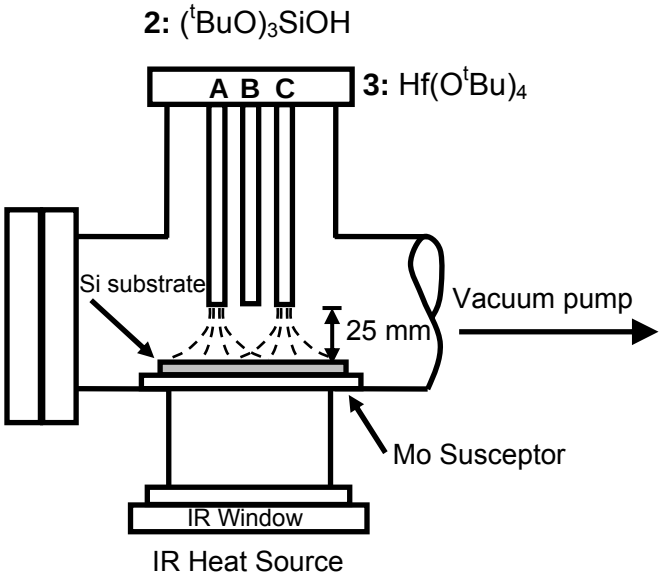

Figure 4.1. Schematic Drawing of Combi-ALD reactor. Flow through inlet lines (1, 2 and 3) was metered by mass flow controllers and driven by computer-actuated pneumatic valves.

Additional experiments were performed in order to shed light on the combi-ALD deposition. Atomic layer deposition of ZTB with tBOS (ZTB/tBOS), HTB with tBOS (HTB/tBOS), ZTB with HTB (ZTB/HTB), and three-component sequential ALD experiments of ZTB, HTB and tBOS (ZTB/HTB/tBOS), as well as the related sequence HTB, ZTB and tBOS (HTB/ZTB/tBOS) were performed. For the three-component sequential ALD experiments (ZTB/HTB/tBOS and HTB/ZTB/tBOS), the zirconia and hafnia precursor pulses of the depositions were always of equal lengths. For all experiments, the purge cycle allowed pure nitrogen gas to flow through all delivery lines used for that deposition. A summary of all experiments is given in Table 4.1.

Substrates were native oxide coated p-doped single crystal Si (100) which were cut to 2.5 cm squares and cleaned in 7:3 concentrated H_2SO_4 : H_2O_2 for at least 24 hrs,

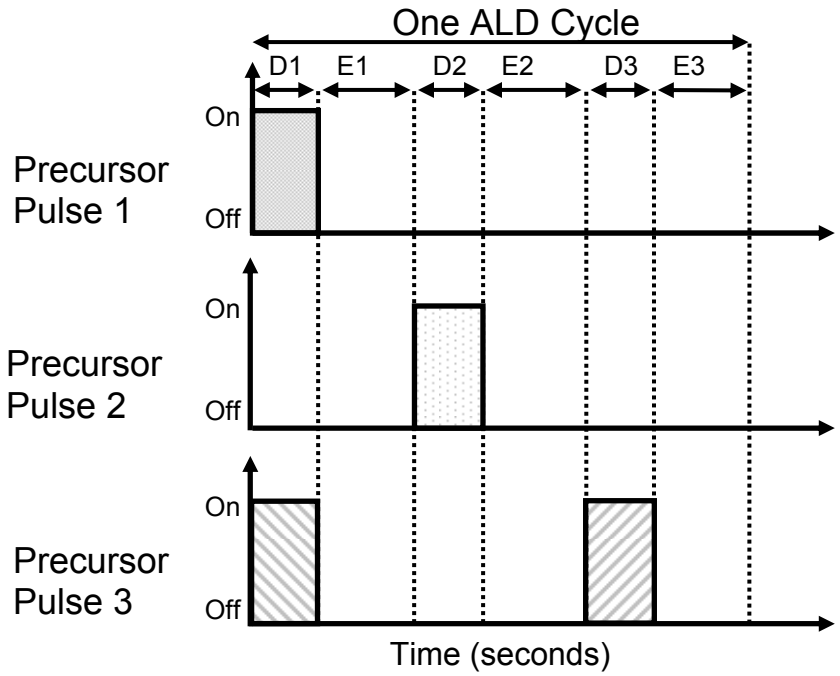

Figure 4.2. Diagram showing ALD pulse sequences. Each precursor pulse consists of a dose (D) and an evacuation (E) period. Multiple precursor pulses combine to make one ALD cycle. Two-component experiments utilize only Precursor Pulse 1 and Precursor Pulse 2. Precursor Pulse 3 shows two possible dose timings; only one precursor dose per pulse is used for any given experiment. Combinatorial experiments use the first dose of Precursor Pulse 3 and three-component experiments utilize the second precursor dose Precursor Pulse 3.

rinsed with DI water, submerged in clean DI water, blown dry with canned air and immediately inserted into reactor. With the exception of samples for film adhesion tests, substrates were not treated with dilute HF.

The HTB and ZTB (as received from Sigma Aldrich) were loaded in a glove box into glass-bead filled bubblers which were then mounted on the reactor and kept at room temperature during depositions. The glass beads were added to the precursor bubblers to take up space and allow the liquid level to rise above the level of the bubbler stem causing the carrier gas to bubble through the precursor liquid and achieve more uniform vapor saturation. Tris-*tert*-butoxy silanol (as received from Sigma Aldrich) was loaded into a precursor vessel in a glove box before being mounted on the reactor. The tBOS vessel was held at 50 °C during depositions. All precursor delivery lines were heated to 75 °C to prevent precursor condensation during delivery.

4.2.2. Analysis

Two ellipsometers were used to measure film thickness. Spectroscopic ellipsometry was performed using a SOPRA spectroscopic ellipsometer with a 70° incident angle. Single-wavelength ellipsometry was performed using a Rudolph ellipsometer with a wavelength of 632.8 nm and incident angle of 70°.

Rutherford backscattering spectroscopy (RBS) was utilized to measure film composition. The instrument was a NEC spectrometer equipped with a MAS 1700 endstation. A He^+ beam of 2.0 MeV with beam current of 10-15 mA was used, and a total charge of 8 μC collected for elemental profile measurements. For the measurement of CVD-mode thin films, a He^+ beam of 2.0 MeV with beam current of 20 mA was used, and a total charge of 20 or 40 μC was collected (40 μC were higher integration current measurements in the location of 20 μC measurements). HYPRA software was used to fit the amount of Hf, Zr, Si and O in the film. Integration of the hafnium and zirconium peaks divided by atomic number squared was used to verify the accuracy of the model. The carbon content was below the detection limit.

A Philips X′Pert five-circle diffractometer was used for specular X-ray reflection. A line focus incident beam (Cu K α 1) was conditioned using a 1/32° divergence slit and an X-ray mirror with a 0.04 rad Soller slit assembly. The reflected X-ray beam was conditioned by a 0.27° parallel plate collimator with a 0.1 mm slit. The X-rays were detected using a Xe proportional detector. Measurements were taken in 2θ/ω geometry from 0.3 degrees to 7.3 degrees using X-rays generated at 45 kV and 40 mA. Modeling of the patterns was done using the X'Pert Reflectivity software package.

Table 4.1. Summary of deposition conditions for combinatorial ALD (Combi-ALD), two-component ALD (ZTB/tBOS, HTB/tBOS and ZTB/HTB) and three-component sequential ALD (ZTB/HTB/tBOS and HTB/ZTB/tBOS) experiments.
na = not applicable, RT = Room Temperature

	Combi ALD	ZTB/tBOS	HTB/tBOS	ZTB/HTB/tBOS	HTB/ZTB/tBOS	ZTB/HTB
Dep. Temp. [°C]	120,140,160	140	140	140	140	140
T (ZTB) [°C]	RT	RT	na	RT	RT	RT
T (HTB) [°C]	RT	na	RT	RT	RT	RT
T (tBOS) [°C]	51 ± 3	51 ± 3	51 ± 3	51 ± 3	51 ± 3	na
Delivery line T [°C]	65-75	75	75	75	75	75
Gas Flow (each) [sccm]	25	25	25	25	25	25
Purge Pressure [Torr]	1.2 ± 0.3	1.6 ± 0.1	1.6 ± 0.1	1.5 ± 0.5	1.5 ± 0.5	1.55 ± 0.1
ALD sequence:						
Precursor 1	ZTB + HTB	ZTB	HTB	ZTB	HTB	ZTB
Pulse length precursor 1	1-30	2-30	1-30	2-20	2-20	2-10
Purge length precursor 1	20	20	20	20	20	20
	(30 for 30 sec pulse)	(30 for 30 sec pulse)	(30 for 30 sec pulse)			
Precursor 2	tBOS	tBOS	tBOS	HTB	ZTB	HTB
Pulse length precursor 2	5-45	5-45	5-45	2-20	2-20	2-10
Purge length precursor 2	30	30	30	20	20	20
	(45 for 45 sec pulse)	(45 for 45 sec pulse)	(45 for 45 sec pulse)			
Precursor 3	na	na	na	tBOS	tBOS	na
Pulse length precursor 3	na	na	na	30	30	na
Purge length precursor 3	na	na	na	30	30	na
number of cycles	25-100	25-100	25-100	100	100	50-200

4.3. RESULTS

Informal evaluation of film adhesion showed films deposited on native silicon oxide substrates passed the tape test, while films grown on dilute HF treated substrates routinely failed the tape test. For all films tested, the initial exposure of the substrate surface was to either HTB or ZTB. Nanolaminate films appeared to either be wholly removed from the substrate or were unaffected by the tape test.

Figures 4.3 and 4.4 show the change in growth per cycle as a function of tBOS pulse length (Figure 4.3) and transition metal alkoxide pulse length (Figure 4.4) for combi-ALD, HTB /tBOS and ZTB/tBOS. The growth per cycle in all cases reached a maximum and did not continue to increase as precursor doses were increased.

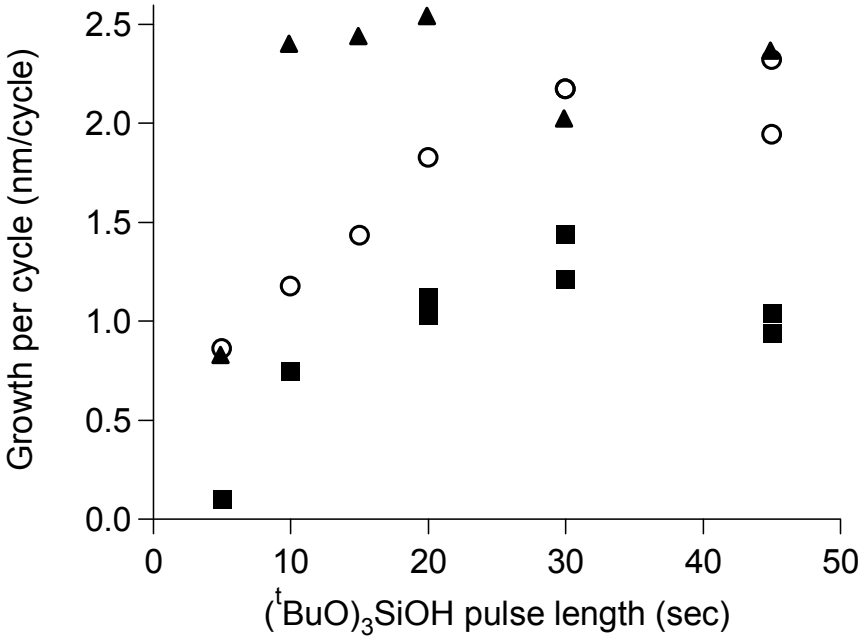

Figure 4.3. Growth per cycle as a function of silanol pulse length (10 second alkoxide pulses,) for combi-ALD of zirconium and hafnium tetrakis-*tert*-butoxides (■), zirconium tetrakis-*tert*-butoxide (○), and hafnium tetrakis-*tert*-butoxide (▲) with various tris-*tert*-butoxy silanol counter pulses. All films were 100 cycles deposited at 140 °C.

For the two-component ALD reactions of ZTB/tBOS and HTB/tBOS shown in Figure 4.3, saturation growth reached a maximum of 2.2 nm/cycle and 2.5 nm/cycle respectively. The combi-ALD film growth saturated at 1.2 nm/cycle. Judging from the data in Figure 4.3, a 30 second tBOS pulse was considered to be sufficient to achieve saturation conditions for all three experiments. As transition metal alkoxide pulse length increased (shown in Figure 4.4), maximum growth rates were 2.2 nm/cycle for ZTB/tBOS and 2.0 nm/cycle for HTB/tBOS. The combi-ALD deposition saturated at 1.5 nm/cycle. A transition metal alkoxide pulse of ten seconds was determined to be sufficient to be in saturation conditions.

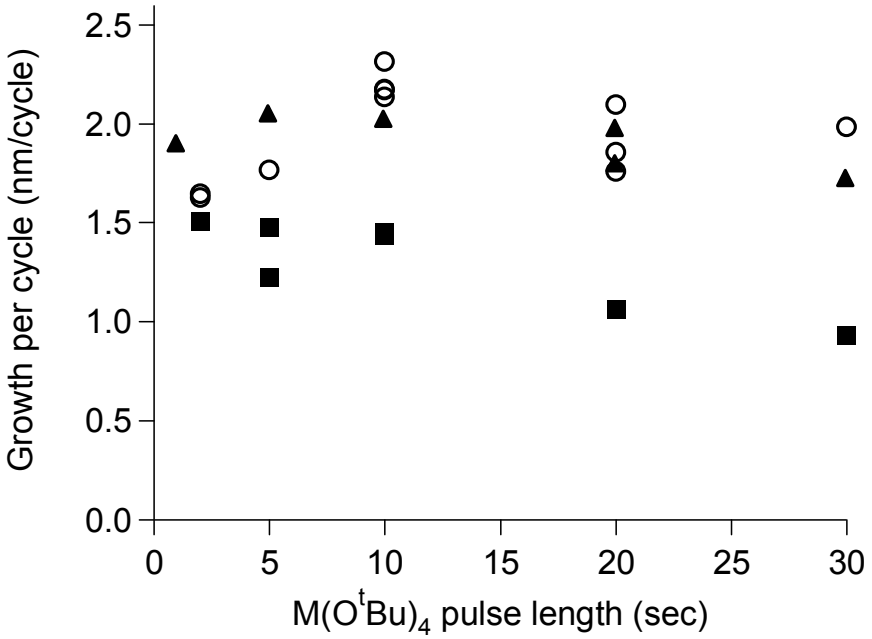

Figure 4.4. Growth per cycle as a function of alkoxide pulse length for combi-ALD of zirconium and hafnium precursors (■), zirconium tetrakis-*tert*-butoxide (○), hafnium tetrakis-*tert*-butoxide (▲) with 30 second tris-*tert*-butoxy silanol counter pulses. All films were 100 cycles deposited at 140 °C.

The relationship of film thickness to total number of deposition cycles for combi-ALD, ZTB/tBOS and HTB/tBOS was investigated (Figure 4.5). A linear relationship between total film thickness and number of deposition cycles was found in all three cases.

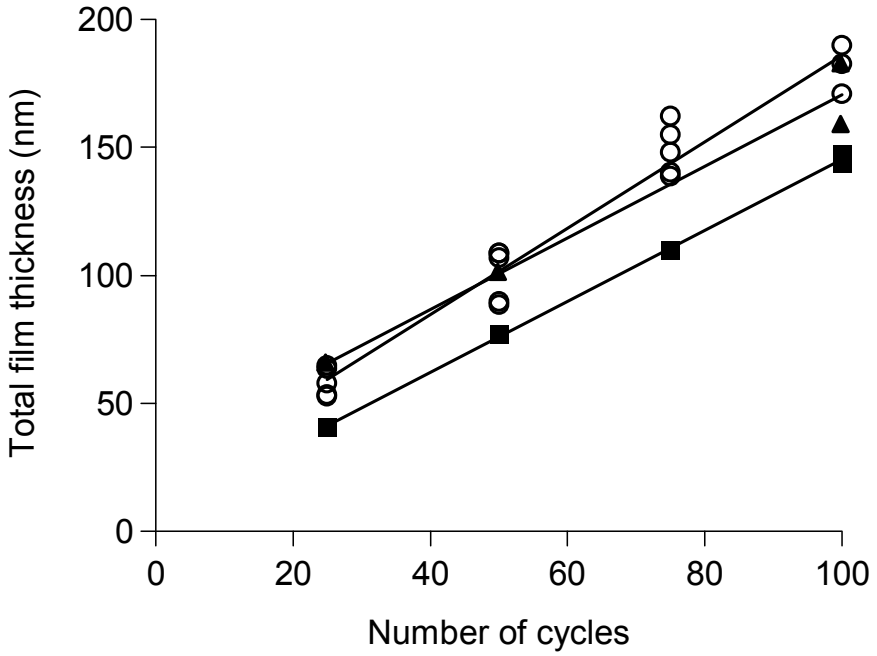

Figure 4.5. Total film thickness as a function of number of deposition cycles for combi-ALD of zirconium and hafnium precursors (■), zirconium tetrakis-*tert*-butoxide (○), and hafnium tetrakis-*tert*-butoxide (▲) with tris-*tert*-butoxy silanol counter pulse. All films were grown at 140 °C under saturation conditions (10 second alkoxide pulses and 30 second silanol pulses).

Rutherford backscattering spectrometry (RBS) was used to determine elemental composition. Measurements were taken on a line running directly under the zirconium and hafnium precursor inlets (a schematic diagram is shown in Figure 4.6 subset) for a combi-ALD film. Both film thickness and film composition were extracted from HYPRA as fit parameters from the obtained RBS spectra (not shown). Figure 4.6 shows the compositions of combi-ALD films deposited by 100 cycles of 10 seconds metal alkoxides (20 second purge) and 30 second tBOS (30 second purge) at 120 °C (▼), 140 °C (■) and 160 °C (▲) along with a 100 cycle film (●) deposited at 140 °C with 5 seconds metal alkoxides (20 second purge) and 30 seconds tBOS (30 second purge). Closed markers are hafnium and open markers represent zirconium. Thickness for the 140 °C combi-ALD sample (as analyzed by RBS fits) is also shown on the graph (×). Measurements in the perpendicular direction to that shown in Figure 4.6 subset and directly under the ZTB inlet (not shown) showed small variations in hafnium (±8.5%) and zirconium (±5.4%) concentration with the highest zirconium concentration directly under the ZTB inlet.

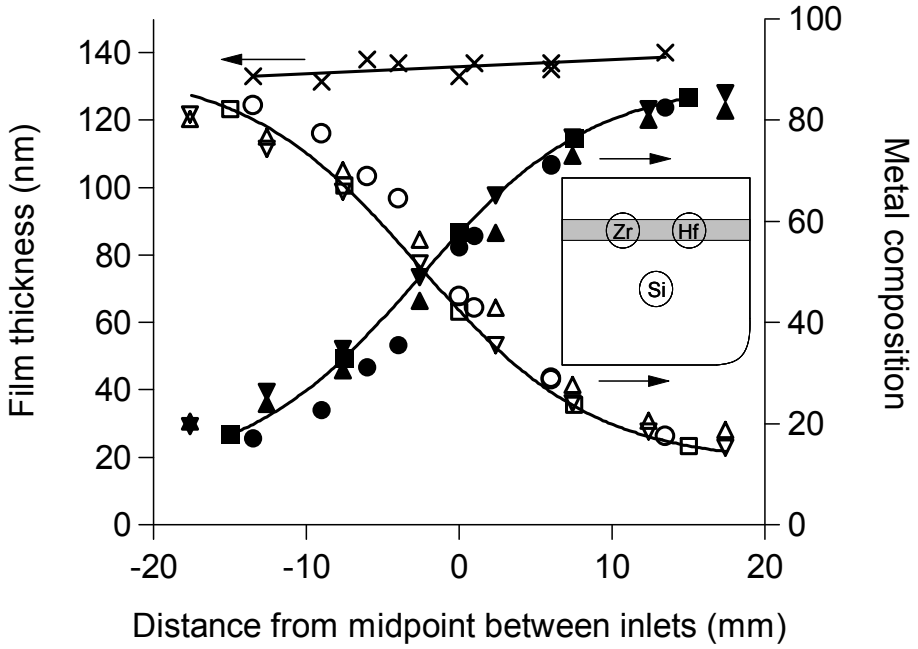

Figure 4.6. Line scan (as shown in inset) of RBS results showing film composition (percent of total hafnium + zirconium) of hafnium (closed markers) and zirconium (open markers) in combi-ALD film deposited under saturation conditions (10 sec alkoxides, 30 sec tBOS) at 120 (▼), 140 (■) and 160 (▲) , plus hafnium (●) and zirconium (○) for 5 second alkoxide pulses (30 sec tBOS) deposited at 140 °C. Also shown is thickness along analysis line (×) for 100 cycle combi-ALD sample deposited at 140 °C (by RBS fits).

The X-ray reflection pattern for three measurements on one combinatorial sample is shown in Figure 4.7. The measurement locations are shown in Figure 4.7 inset; each measurement encompasses a narrow slice of the film which extends the entire length of the sample. The modeled fit parameters for these three measurements are listed in Table 2.2.

RBS results for several three-component sequential ALD experiments are shown in Figure 4.8. The pulse sequence for these results was always ZTB/HTB/tBOS, with the variation shown on the X-axis being the length of the ZTB and HTB pulses. Concentrations are reported as fraction of (Si+Zr+Hf). Silicon concentrations range from 75.65% – 81.22%; zirconium concentrations are between 15.09% - 20.33%, and hafnium concentrations vary from 3.08% - 4.62%. Overall film thickness decreases from 212.4 nm to 158.7 nm with increasing alkoxide pulse length.

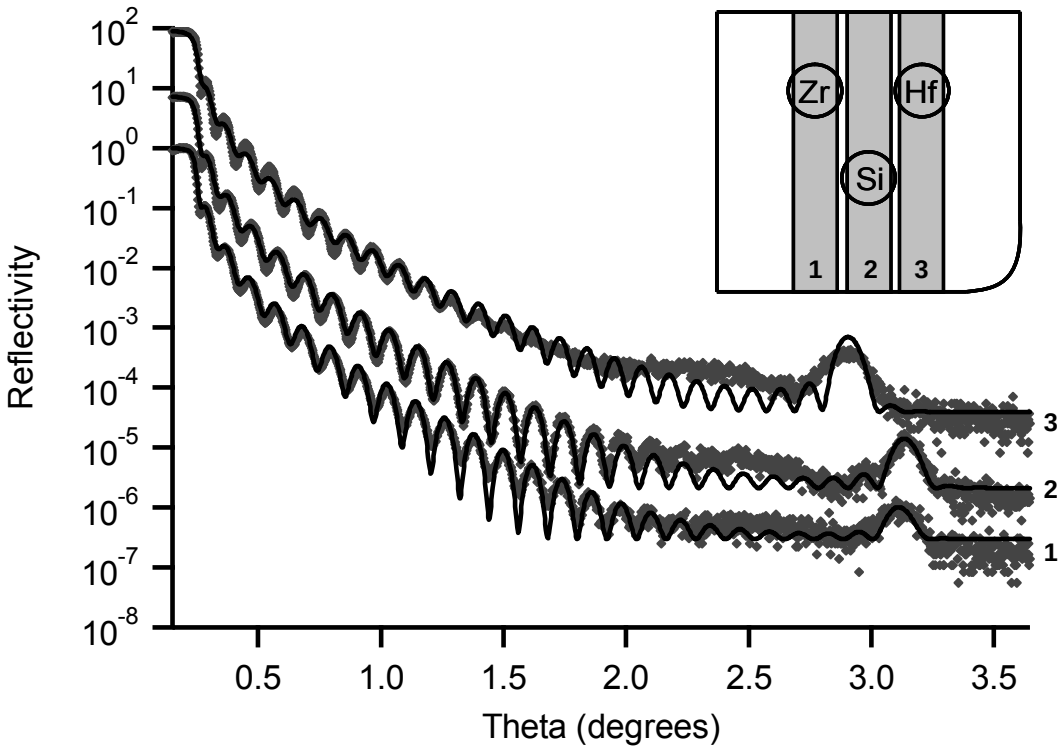

Figure 4.7. X-ray reflection patterns of combi-ALD film. Three separate areas were analyzed on the substrate surface, yielding three patterns. Patterns are offset for clarity. Film was deposited for 100 cycles under saturation conditions (10 seconds alkoxides, 30 seconds tBOS) at 140 °C.

For the three component ALD experiment ZTB/HTB/tBOS (graph not shown), no change of film thickness (1.428 nm/cycle GPC) or composition (82% zirconium and 18% hafnium) was seen when the purge length after the ZTB and HTB pulse was doubled from 20 to 40 seconds. HTB and ZTB pulse lengths were 10 seconds, and the tBOS pulse length was 30 seconds with a 30 second purge.

Also explored was the effect of changing from ZTB/HTB/tBOS three-component sequential ALD to a HTB/ZTB/tBOS three-component sequential ALD. Both films were deposited under identical reactor conditions with saturation pulse lengths; only the precursor order was changed. The greatest elemental representation (82% per total Zr+Hf) in the growing film was due to whichever species (ZTB or HTB) was first pulsed onto the film surface after the tBOS cycle was complete; however, a significant amount of the second precursor (18%) was observed in the film. The observed limits in the composition (82% - 18% by total of Zr+Hf) were also same the limits seen in the outer edges of the combi-ALD experiments.

Table 4.2. X-ray reflection modeling results. All films are modeled as 26 bilayer repeat units on top of single crystal silicon. For reference, material densities listed in the X'Pert modeling software are ZrO_2 = 6.1 g/cm^3, SiO_2 = 2.64 g/cm^3 and HfO_2 = 8.9 g/cm^3

XRR Sample location	Total film thickness (nm)	Bilayer spacing (nm)	Layer	Thickness (nm)	Density (g/cm^3)	Roughness (nm)
1	36.712	1.412	1	0.445	4.4469	0.623
			2 (silica)	0.967	1.8271	0.715
2	36.608	1.408	1	0.475	5.5545	0.597
			2 (silica)	0.933	1.7781	0.732
3	37.975	1.519	1	0.459	6.7500	0.770
			2 (silica)	1.06	1.6815	0.604

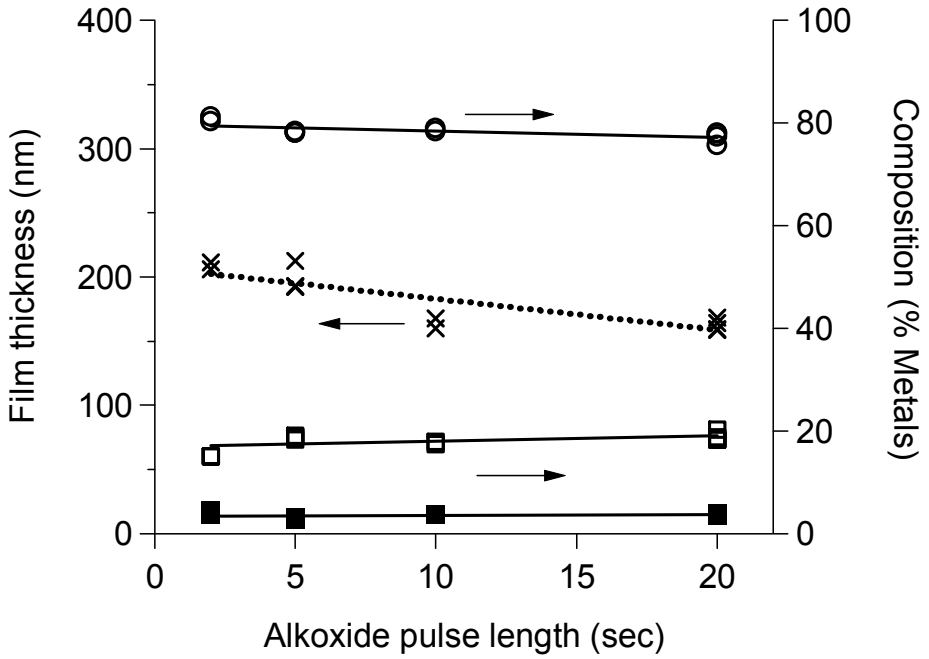

Figure 4.8. RBS results showing composition (percentage of Zr + Hf + Si) of hafnium (■), zirconium (□) and silicon (○), as well as thickness (×) as a function of alkoxide pulse length for several three-component sequential ALD experiments of ZTB/HTB/tBOS. tBOS pulse times were 30 seconds. All films were deposited by 100 cycles at 140 °C.

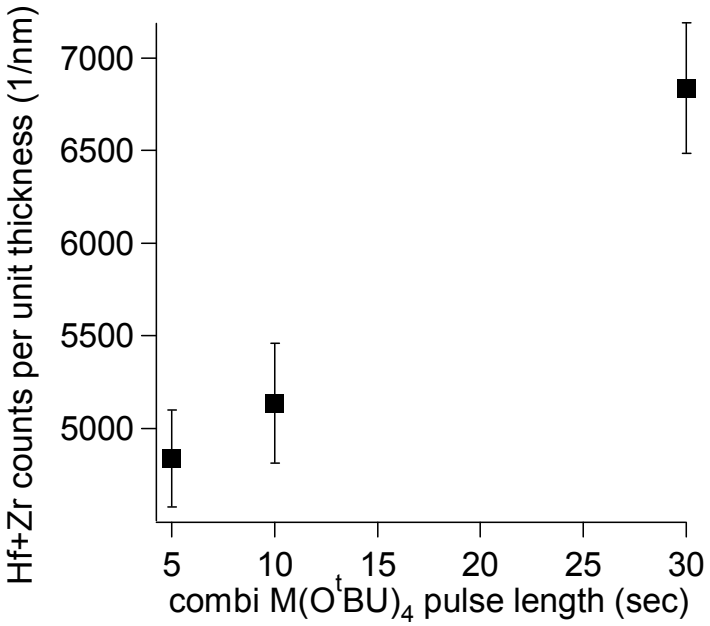

Figure 4.9. RBS counts for hafnium and zirconium calculated by normalizing RBS spectra to silicon background signal and adding counts from channels corresponding to hafnium and zirconium. Total counts of hafnium and zirconium are divided by film thickness to calculate relative amounts of hafnium and zirconium per unit thickness.

Further RBS results given in Figure 4.9 illustrate the increasing amount of hafnium and zirconium per unit thickness as a function of combi-ZTB+HTB pulse time. The amount of hafnium and zirconium per unit thickness is increasing as the film thickness is decreasing. Film thickness as a function of ZTB + HTB pulse time is shown in Figure 4.4.

Depositions were performed to measure the effect of CVD-mode precursor decomposition on the overall ALD process. Precursors were introduced into the reactor continuously or in a pulsed manner without a counter-reactant present in order to determine the magnitude of competing deposition processes. The results are given in Table 4.3.

Table 4.3. Depositions conducted to demonstrate presence and significance of CVD-mode reactions in the ALD experiments. ALD type experiments have one 10 sec precursor pulse followed by a 30 second nitrogen purge, except HTB/ZTB which is two sequential ALD pulses. GPC for the CVD experiments was calculated by dividing the film thickness by number of sequential 10 second deposition intervals (e.g. thickness/200 for a 2000 sec CVD)

Precursor:	HTB	ZTB	HTB/ZTB
Experiment type (below)	Growth per cycle (nm/cycle)		
100x ALD	0.127	0.208	0.355
200x ALD	0.0785	0.1105	0.339
1000 sec CVD	0.0705	0.0585	0.239
2000 sec CVD	0.0725	0.0655	na

4.4. DISCUSSION

Figures 4.3-4.5 show the two features necessary for ALD growth – self saturating deposition and linear relationship of thickness to number of deposition cycles. This behavior was demonstrated for both the two-component experiments and the combinatorial depositions. The elemental compositional gradients of several films are shown in Figure 4.6 which highlights the stoichiometric non-uniformity across the deposited film. The gradients of hafnium and zirconium exhibited in the film were not dependant on precursor pulse length doubling from 5 to 10 seconds of HTB and ZTB pulse. Additionally, for the three deposition temperatures explored (120, 140 and 160 °C), no change in stoichiometric distribution was observed. Taken together, these data show combinatorial ALD of ZTB and HTB with tBOS was successful and the elemental distribution robust to the experimental conditions explored.

While lateral compositional variation has been observed, it was unknown if the films contained vertical structure or texture. The deposits could have formed as well-mixed amorphous materials, phase-segregated nanocrystalline composites or perhaps as nanolaminates with alternating layers with oscillating chemical composition. The films were analyzed by X-ray reflection to look for repeating microstructure of the type

expected for nanolaminate materials (Figure 4.7). Bragg peak diffractions were seen in the reflection pattern, and these were successfully modeled using Philips X-Pert reflection modeling software. Two features are apparent in the patterns, an oscillating signal with a repeat distance of 0.1 degrees and a larger peak near 3° theta. The smaller features (Kiessig fringes) arose from the reflection of the X-ray beam off of two interfaces, the air/film surface and film/substrate surface, and yield a measurement of total film thickness. The larger peak near 3° theta arises from a Bragg-like diffraction due to a repeating bilayer structure within the film. Modeled results indicated the repeating structure within the film had two layers. One layer was denser (about 75% of the reference density of zirconia or hafnia under the respective precursor inlets) and had a roughness on the order of the thickness of the layer. This high roughness suggests a clean interface did not exist between the alternating layers of the bilayer structure. The second layer was less dense (67% silica reference density), and it had a roughness less than half of the total layer thickness. The reduction in the density of the deposited material hinted that the film microstructure was porous, though no additional tests were performed to confirm this. The smaller roughness of this second layer suggested that while a continuous material gradient existed between bilayers, the middle of the less dense (and thicker) layer was a constant density of material, suggesting a constant stoichiometry. These observations were consistent with a deposition mechanism involving small deposition of hafnia and zirconia per cycle, combined with a silicon dioxide layer which was thicker and contained a region of relatively pure silicon dioxide. This data was sensible, because tBOS was known to deposit many atomic layers in a single deposition cycle.[56]

Combi-ALD has been shown to form films with lateral compositional variation and nano-laminate film microstructure. The lateral elemental distribution discussed above was insensitive to the experimental parameters explored. However, the ALD processes involving ZTB, HTB and tBOS exhibited reductions in growth per cycle after saturation in the ZTB and HTB (Figures 4.4 and 4.8).

For the three-component sequential ALD experiments, there was no change in film thickness or stoichiometry for a doubling of the purge time between the ZTB and

HTB pulses. One can infer from this data that the chemical species responsible for deposition are tenaciously adsorbed to the surface after the precursor pulse cycle and do not desorb significantly during the purge cycle. Thus, the loss of precursor from the surface to the gas phase during the pulse cycle can be eliminated as a cause of the evolution of growth rates and stoichiometric changes. However, it should be noted that a significant amount (circa 18%) of the second component (Hf) of the ZTB/HTB/tBOS experiment is observed in the film. Additionally, the amount of hafnium and zirconium in the film increased with pulse length, while the total film thickness and the amount of silicon decreased. This suggests that there is additional reaction of the HTB precursor with the surface after the ZTB purge cycle.

One potential explanation for this phenomenon is a chemical vapor deposition (CVD) mode of film growth, potentially assisted by decomposition by-products (contaminants). Table 4.3 shows results of the experiments performed to verify the presence of a CVD-mode reaction in the ALD experiments. The results indicate decomposition of ZTB and/or HTB was present under the ALD experimental conditions. Onset of thermal decomposition of ZTB in ultra-high vacuum can be noted as low at 300 °C.[57] However, Bradley notes the tetrakis-*tert*-butoxides of zirconium and hafnium suffer from thermal instabilities during distillation at a lower temperature (150 - 200 °C).[58] Alkoxide precursors are not typically chosen for ALD applications, because of limited elemental availability and the tendency of these molecules to undergo thermal decomposition in a CVD mode and release ligands which can interfere with growth.[59] The reported ALD of ZTB and water did not show typical saturation behavior in the length-scale of the experiment and indicated a high level of reactivity of these two species.[60] It is not extraordinary to suggest that a slow CVD-mode reaction on the surface might be the cause of the incorporation of the second component in the three-component ALD reactions, as well as causing the decreasing film growth per cycle with increasing HTB, ZTB or ZTB+HTB pulses. At the surface temperatures involved in these experiments, one would expect to be operating in the rate-limited regime of CVD. At such conditions, precursor molecules would exist in an adsorbed state, but would not immediately continue to decompose into growing film and new surface sites. When a

molecule does undergo decomposition (or contaminant reaction) and a surface site is regenerated, a new molecule would be adsorbed from the gas-phase precursor flux.

Using kinetic parameters available in the literature one can calculate the ZTB and HTB deposition rate predicted at 140 °C in a UHV system.[61,62] Assuming perfect precursor packing on an ideal crystal surface, the predicted growth rates, 9.17×10^{-7} Å/sec for ZrO_2 and 2.43×10^{-5} Å /sec for HfO_2, are orders of magnitude lower than the observed growth rates, suggesting that this deposition process is not the same as at UHV. One potential explanation is that water or alcohols created as a by-product of the reaction is reacting with the precursors to stimulate further film growth.

While the experimental evidence indicates a CVD-mode reaction is occurring on the growing film surface during an ALD experiment, this deposition phenomenon should add atoms to the growing surface. This seems counter to the previous mention of the growth per cycle decreasing with increasing pulse time. One must consider, however, at what cost these molecules are being deposited. Key to the concept of ALD is the idea of limited surface sites. A location must exist on the surface to which an arriving molecule can attach. The loss of surface sites through chemical reaction would decrease the number of available sites for the next half-cycle of ALD experiment. This would, in turn, decrease the amount of material deposited in the next half-cycle of ALD.

The silica precursor used in this report (tBOS) was previously mentioned to have a growth per cycle larger than a single monolayer. In the specific case of trimethylaluminum and tris-*tert*-butoxy silanol, up to 32 monolayers of silica were deposited per cycle. Because the tBOS deposited many atomic layers per cycle, the loss of reactive sites after the HTB+ZTB pulse would have resulted in a substantial decrease in film thickness. It was seen that for the combi-ALD depositions, growth per cycle went down nearly 50% when the HTB+ZTB pulse increased from 2 seconds to 30 seconds (Figure 4.4). Additionally, for the three-component sequential ALD reactions (Figure 4.8), as the films became thinner with longer pulse times, the silicon content in the films decreased while the zirconium and hafnium content increased. Taken together, these data illustrated that increasing the flux of ZTB+HTB to the surface either simultaneously (as in the combi-ALD versus the ZTB/tBOS or HTB/tBOS experiments) or integrally (as in

longer ZTB and HTB pulses to the surface during the ZTB/tBOS, HTB/tBOS and three-component ALD) decreased the overall growth per cycle. Because both the film thickness and the composition do not change with a doubling of the purge time, no chemical changes are expected to occur at the surface during the purge that would affect the state of the growing film.

The conclusion can be drawn that a loss of surface reactive sites after the HTB+ZTB combi pulse contributes to the decrease in film thickness. This reduction in surface sites is postulated to occur through a CVD-mode reaction where the overall number of surface sites is reduced. Decreasing the available surface sites for tBOS growth should result in not only in reduction of GPC, but in a reduction in the amount of silicon per unit distance, or conversely, an increase in the zirconium + hafnium per unit distance. Figure 4.9 demonstrates the increasing amount of hafnium and zirconium per unit distance with increasing pulse time.

4.5. CONCLUSION

Atomic layer deposition of hafnium tetrakis-tert-butoxide with tris-*tert*-butoxy silanol and zirconium tetrakis-tert-butoxide with tris-*tert*-butoxy silanol was reported. The important features of an atomic layer deposition process have been observed: self-limiting growth rates of each precursor and linear relationships of film thickness to number of deposition cycles. Combinatorial atomic layer deposition has been performed and evaluated. The process conforms to an ALD-mode of deposition. A lateral gradient of HfO_2 and ZrO_2 has been measured in the deposited film, while the film thickness remained essentially constant over the same measurements. Repeating bi-layer morphology was analyzed using X-ray reflectivity. The modeled results indicate the interfaces between the layers were not abrupt, but the composition of the two layers (as observed by material density) was different. A slow chemical vapor deposition / contaminant side-reaction interaction was present on the film surface, and this phenomenon was invoked to explain the gradual decrease in deposition rate with increasing precursor pulse time.

CHAPTER 5

Modeling Combinatorial Low-Pressure Chemical Vapor Deposition

5.1. INTRODUCTION

Combinatorial synthesis is an effective research tool for the chemical sciences. From the physical vapor deposition work of van Dover and Schneemeyer[63,64,65] to the use of combinatorial synthesis in pharmaceutical research,[66,67,68,69] many different specialty areas have found advantage in the discovery of new materials and compounds through combinatorial techniques. A combinatorial approach allows for high-throughput synthesis and screening of potential compounds through simultaneous creation of a wide range of stoichiometries or functionalities. Tens to hundreds of experimental depositions would be required to produce a complete library of a ternary system if each film is stoichiometrically homogeneous. By creating many different local stoichiometries on a substrate simultaneously, the time required to deposit potential compositions is significantly reduced. Different locations on the substrate can be probed by various analytical techniques, to gain an understanding of the material composition and properties.

As the miniaturization of computer chips continues, a fundamental limit is approached near 1.5 nm of dielectric thickness where the quantum tunneling properties of electrons reduces the efficacy of insulating layers in electronic devices.[70,71] Once the quantum tunneling limit is reached, either new materials or new designs will be required to continue to produce faster and more efficient electronic components.[72] Owing to the extremely large investment in chip design and fabrication equipment, the desired solution is to find a process-compatible replacement material, with similar physical properties to SiO_2 or SiO_xN_y, but with better electrical properties.[73]

Mixed metal oxides in particular have been investigated as replacements for SiO_2 or SiO_xN_y films. Recently, Gladfelter and coworkers have applied combinatorial concepts to chemical vapor deposition for the investigation of gate dielectric materials for replacement of silicon dioxide in MOSFET electronic devices.[74,75] Gladfelter and coworkers modified an existing low pressure chemical vapor deposition (LPCVD) reactor[76] to simultaneously introduce the precursor gases in close proximity to the

substrate surface and to each other. A single deposition can be performed which creates a range of stoichiometries on a single substrate. Ellipsometric and RBS investigation of deposited films revealed the fastest film growth rates to be directly below each precursor injector.[77,78] As the radial distance from the injector increases, the film growth rate decreases. Films grown from depositions using several injectors are similar, though not identical, to the summation of the growth rates from single injector depositions. It was then supposed that the rate of film growth on the substrate was a combination of chemistry and fluid mechanics.[79]

The current work will attempt to further understand the interplay of chemistry and fluid dynamics in the combinatorial LPCVD reactor. Commercially available finite-element computational fluid dynamics code (CFD-ACE+) from the Computational Fluid Dynamics Research Corporation[80] was chosen to model the LPCVD deposition process. The program CFD-ACE has been used in application studies including fuel cells,[81] heat transfer through porous materials,[82] optoelectronics,[83] radiative heating[84] and BioMEMS.[85a-d] Chemical vapor deposition has also been modeled using CFD-ACE for such applications as metal organic CVD (MOCVD),[86a,b] high pressure CVD,[87] metal organic vapor phase epitaxy[88] and low pressure CVD.[89a-d]

It should be noted that this study was not fully completed. Difficulties were encountered with solver convergence. While many different grid densities were tried, and many different solver parameters attempted, success was elusive. It was possible the low pressure of the deposition lead to difficulties with modeling solver mechanics due to the proximity of rarefaction conditions where the Navier-Stokes approximations fail. This report is included herein for future researchers should they attempt this experiment again.

5.2. EXPERIMENTAL

Depositions were performed using a modified LPCVD reactor described below. Calculations and measurements were performed to determine parameters such as flow rate, background pressure, reaction stoichiometry, and susceptor temperature for use in computational modeling. Details of reactor construction, deposition experiments, measurements of chamber conditions and film properties, and software used for parametric development is presented.

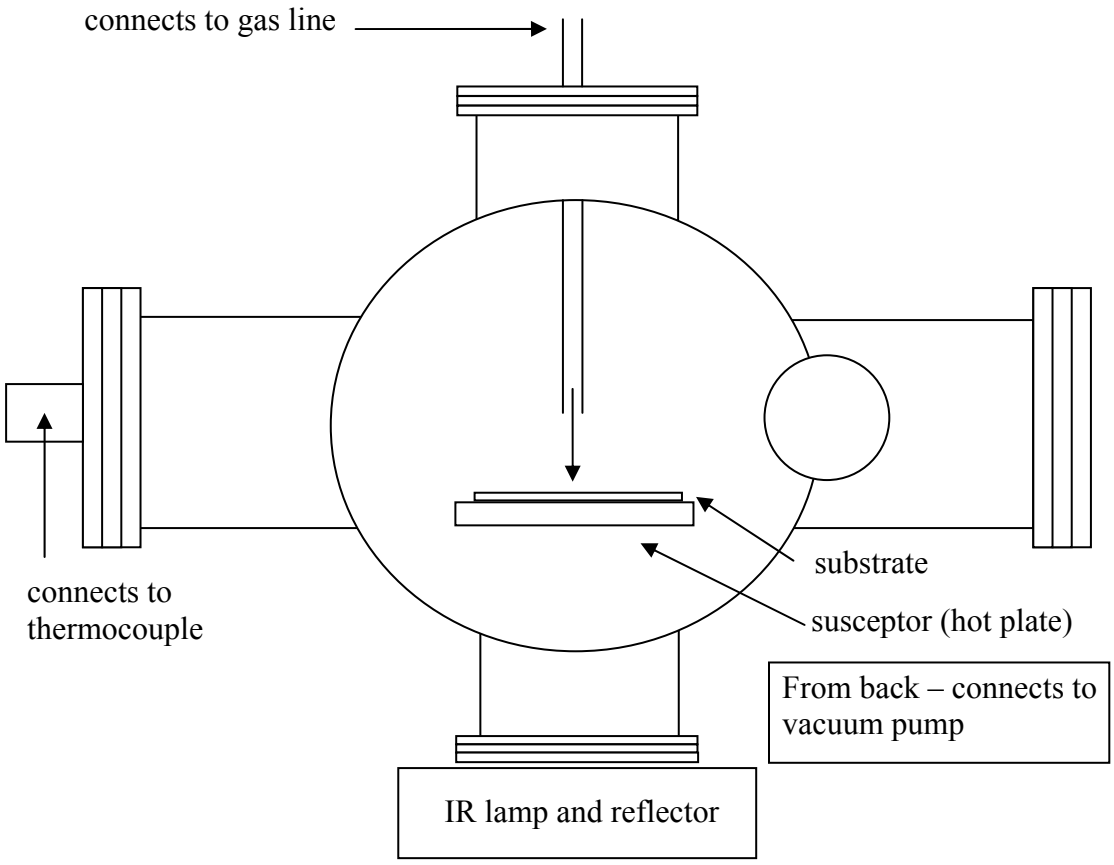

Figure 5.1. Schematic of combi-CVD reactor

Construction of a low pressure chemical vapor deposition (LPCVD) reactor was undertaken with details of the reactor given in Appendix I. The design for the new

reactor was based on a Gladfelter and coworkers' reactor detailed in literature[90]. A schematic of the combinatorial LPCVD reactor is shown in Figure 5.1. The addition of an automated gas handling system with four gas lines equipped with mass flow controllers (MFC's) was employed (Figure 5.2). Each gas delivery line was the same length from precursor vessel to injector head, which allowed for simultaneous arrival of two or more precursor gases to the substrate when the precursor valves were simultaneously opened by an automated gas handling routine in LabVIEW.

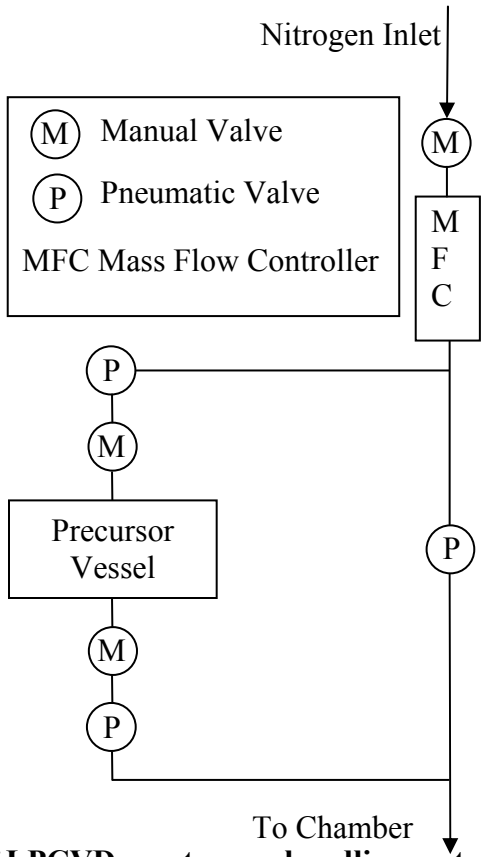

Figure 5.2. Schematic of LPCVD reactor gas handling system

5.2.2. Chemical Vapor Deposition Experiments in the LPCVD Reactor

Depositions were performed in the LPCVD reactor with zirconium tetra-*tert*-butoxide (ZTB) used as received from Alfa Aesar on p-type silicon. The experimental conditions used were as follows:

Table 5.1. Deposition conditions for LPCVD reactor

Nitrogen mass flow rate	2 sccm
ZTB precursor temperature	28 °C
Susceptor temperature	400 °C
Deposition time	2 minutes

Precursor vessels were loaded in a nitrogen glove box with zirconium tetra-*tert*-butoxide. The silicon wafers were cleaned and stored in piranha solution (30% H_2O_2, 70% H_2SO_4). Immediately prior to use, the native oxide layer was removed by immersion in 10% hydrofluoric acid for several minutes to hydrogen terminate the surface.[91] Evidence of the hydrogen terminated surface was the hydrophobic nature of the cleaned substrate when removed from the cleaning solution.

Prior to deposition, the manual valves on the reactor were opened, and the mass flow controller was set to the specified experimental value. The reactor was vented to atmospheric pressure using dry nitrogen. Nitrogen was flowed through the delivery lines while the chamber was open to reduce the water contamination entering the system. The chamber was opened, and a 2.5 x 2.5 cm silicon substrate was placed on the molybdenum susceptor. The chamber was sealed and evacuated for a minimum of 30 minutes while under nitrogen purge through the delivery lines. The in-line cracker oven was heated to 675 °C to decompose any residual precursor gas to reduce wear on the vacuum pump. While the lamp was heating the molybdenum susceptor in the reactor to reaction temperature, compressed air was directed at the IR heating lamp, lens and gasket to keep them cool. Once the susceptor temperature and chamber pressure were stable, the carrier gas was diverted through the precursor vessel for precursor delivery to the substrate. Once deposition was complete, the lamp was turned off, and the system was allowed to

cool. The chamber was brought to atmospheric pressure with dry nitrogen and opened when the temperature of the susceptor was below 70 °C.

Experiments were conducted to measure the effects of susceptor temperature on chamber pressure using the same experimental conditions listed above. After recording a chamber pressure with only nitrogen entering the system, the nitrogen flow was diverted through the precursor vessel. Measurements were recorded of susceptor temperature and chamber pressure every 15 seconds . After the chamber pressure stabilized, the IR heating lamp was turned on. Chamber pressure and susceptor temperature were recorded as the susceptor was heated to 450 °C. The lamp was then turned off, and the flow of nitrogen was diverted to by-pass the precursor vessel.

5.2.3. Ellipsometry Conditions

Ellipsometry was performed at the Microtechnology Lab at the University of Minnesota. A single wavelength of 6328 Å was used with an incident angle of 70° and a 45° polarizer. The index of refraction (3.8646) and extinction coefficient (-0.1414) were measured on a freshly cleaned p-type silicon wafer. Additional details of the ellipsometric mathematics and derivation of thickness and index of refraction from ellipsometric data is given in Appendix III.

5.2.4. Sample Preparation for Scanning Electron Microscopy

One silicon wafer with film sample was fractured through the center by scoring the backside of the wafer and cracking the substrate. A section approximately 2.5 cm long and one cm wide was glued edge-on to a SEM stub with carbon paste. A small piece of silicon was glued perpendicular to the thickest area of the sample, as determined by optical inspection of the interference fringes, when

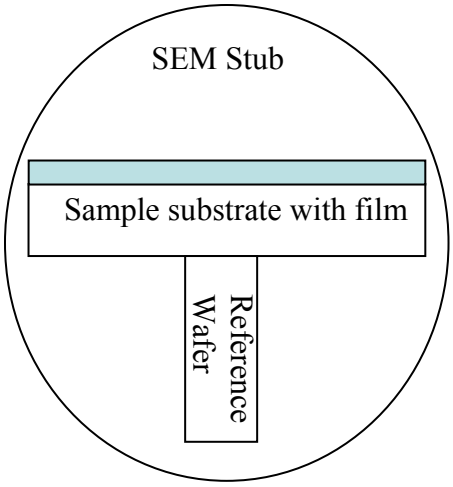

Figure 5.3. Schematic of SEM sample

the sample was mounted on the SEM stub (Figure 5.3). The reference wafer allowed determination of the center of the sample wafer while the sample was in the SEM. Each sample was coated with approximately 10 Å of platinum in a sputter coater. Secondary electron images were taken using a JEOL 6700 scanning electron microscope with beam energies of 2.0 keV and typical working distances of approximately 2.0 mm.

Photoshop was used to determine the thickness of the film by highlighting the film area and measuring the contained pixels. The scale bar was measured in pixels to give a conversion to metric units. The procedure was performed several times for each image, and the average thickness was reported in Figure 5.6.

5.2.5. Calculation of Collision Diameters

Geometric models of tetraethylorthosiloxane (TEOS) and zirconium tetra-*tert*-butoxide (ZTB) were created in PCModel. Gaussian98W was used to geometrically optimize the two structures so collision diameters could be calculated for use in the computational modeling.

5.3. COMPUTATIONAL STUDIES

Using CFD-ACE, a finite-element computational model of the reactor was created. Physical properties such as density, velocity, temperature, and species concentration for a given finite-element are iteratively calculated from the values in the adjacent cell(s) using the Navier-Stokes fluid dynamics equations and other conservation principles discussed in Appendix II. CFD-ACE uses molecular transport, thermodynamic and chemical reaction parameters pre-programmed for each species in the calculations.

CFD-ACE was chosen because it allows utilization of surface chemistry reactions. A deposition profile, which can be empirically compared to samples produced in the LPCVD reactor, is calculated from the model results. The surface chemistry of ZTB was modeled using ultra-high vacuum film growth kinetics derived by Burleson, *et al.*[92] Reaction parameters, such as background pressure, mass flow rate, precursor mass

fraction and substrate temperature, were entered to achieve accurately modeled values. Color visualizations of density, velocity, temperature, flow lines and species concentrations, as well as other parametric values, are achieved using the visualization software, CFD-VIEW.

5.3.1. Construction of a Computational Model of the LPCVD Reactor

A two-dimensional, axi-symmetric geometric model was created to encapsulate the reactor geometry where deposition related processes occured. Ellipsometric measurements of films grown in the LPCVD reactor justify the above assumption of axi-symmetry.

Figure 5.4 shows a schematic of the LPCVD reactor along with the two-dimensional axi-symmetric computational model created in CFD-GEOM. The model had an axis of symmetry along the right vertical axis. The blue-shaded area in the center of the model is the susceptor. It has no finite element mesh, because no property calculations occurred within the volume. The injector stem was modeled as stainless steel with a mesh to allow computation of tube heating by convection. The rest of the internal divisions visible in the model represent transparent interfaces that are artifacts of the model geometry creation. All outside edges, excluding the injector inlet, injector stem and susceptor edges, were programmed as outlets.

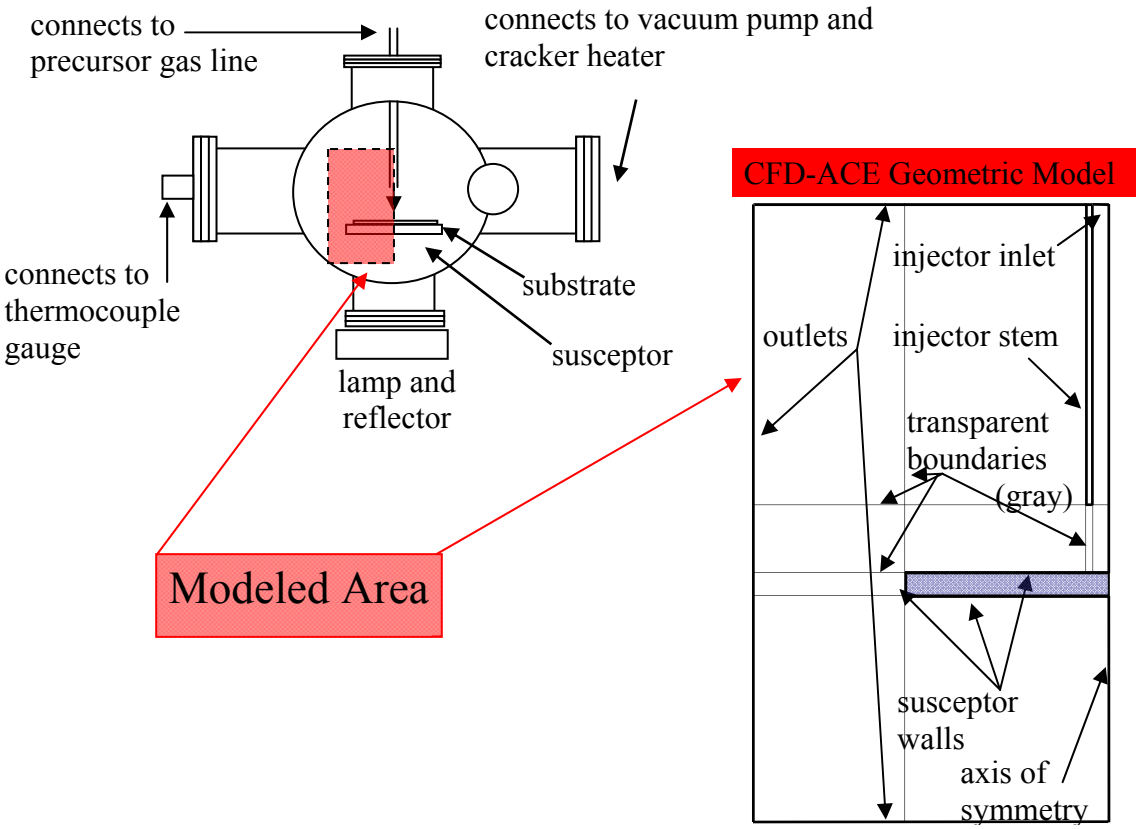

Figure 5.4. LPCVD reactor schematic with associated computational model (reactor model not to scale)

Figure 5.5 shows the CFD-ACE model with dimensions. Relevant geometric features to note are the height of the injector above the substrate (9mm), the width of the injector opening (2mm radius), the width of the susceptor (27 mm radius) and the axis of symmetry, directly down the center of the injector. These specific dimensions are taken from physical measurements of the reactor and injector stems. All other dimensions are compromises to the non-axisymmetric geometry of the LPCVD reactor. The height and width of the outlets are less than the dimensions of the reactor. The assumption was made that the pressure beyond these geometric limits in the LPCVD reactor was constant.

The geometric model was populated with a structured finite volume mesh, also shown in Figure 5.5. Additional details of mass transport parameters, boundary conditions, initial conditions and iterative solver parameters can be found in Appendix III.

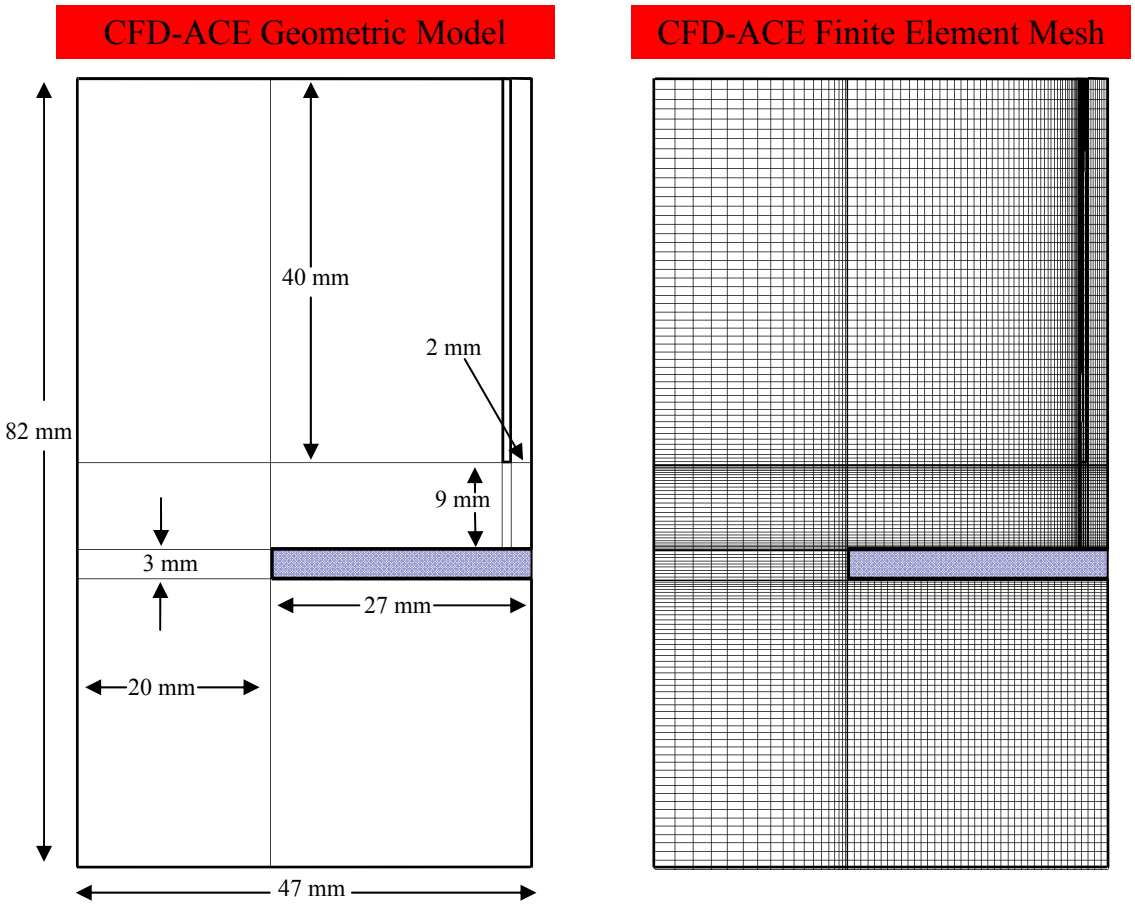

Figure 5.5. Axisymmetric CFD-ACE geometric model with dimensions and finite element mesh

5.4. RESULTS

The films created by single-injector depositions in the LPCVD reactor appeared as circular visible colored rings due to thin-film optical interference. Thicknesses of the as-deposited films were measured by ellipsometry and SEM. Table 5.2 lists the deposition conditions and the maximum deposition rate by ellipsometry for several depositions.

Table 5.2. Deposition conditions and maximum thicknesses for several LPCVD samples

Sample Number	Precursor Temp. (°C)	Susceptor Temp. (°C)	N_2 Flow Rate (sccm)	Dep. Time (min)	Dep. Pressure (mTorr)	Max Thickness (Å)
07010301	27.7	300	2.0	2.0	221	1640
07010302	28.5	300	2.0	2.0	209	1800
07010303	28.7	300	2.0	2.0	202	1900
07010304	28.9	300	2.0	2.0	202	1850
06260301	28.6	350	2.0	2.0	191	1920
06260302	28.9	350	2.0	2.0	---	2370
06270301	28.0	350	2.0	2.0	189	2530
06270302	28.2	350	2.0	2.0	200	2400
06270304	28.2	350	2.0	2.0	198	2430
04110302	27.0	400	2.0	2.0	210	2260
04110301	27.0	400	2.0	2.0	193	3110
06300302	28.7	400	2.0	2.0	215	3150
06300303	28.9	400	2.0	2.0	215	3100
06270305	28.7	450	2.0	2.0	203	3760
06300304	28.9	500	2.0	2.0	219	4040
06300305	28.8	500	2.0	2.0	223	3600
06300306	28.9	500	2.0	2.0	222	3830

5.4.1. Thickness Measurement by Single Wavelength Ellipsometry

The data shown in Figure 5.6 represent ellipsometric measurements performed in two perpendicular directions, "x" and "y", on an as deposited ZrO_2 film. The data in Figure 5.6 support the earlier assumption of the axi-symmetric nature of the deposition process. The error bars in Figure 5.6 are based on a 3% instrument error as presented by Riedling[93] plus the percent error of the index of refraction for each point.

For certain combinations of thickness and index of refraction, the dielectric film

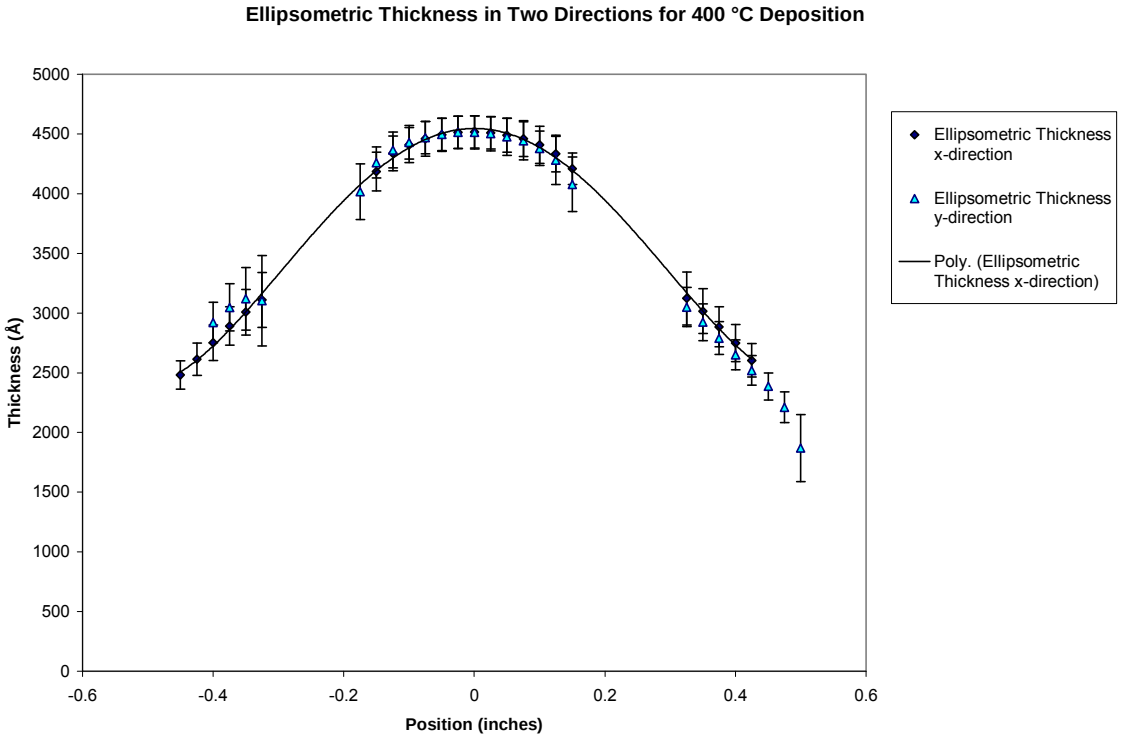

Figure 5.6. Ellipsometric film thickness for a two minute, single-injector deposition in the LPCVD reactor

acts as an anti-reflection coating causing destructive interference of the reflected light. The result is a cyclical pattern corresponding to the zone of ellipsometric conditions where the thickness and index of refraction can not be measured accurately due to low signal to noise. Riedling presents a good explanation of the error effects on the ellipsometric modeling of thin films.[94] The gaps in ellipsometric data in Figure 5.6 and the variability of the index of refraction in Figure 5.7 show regions where accurate single-wavelength ellipsometric measurements are not possible.

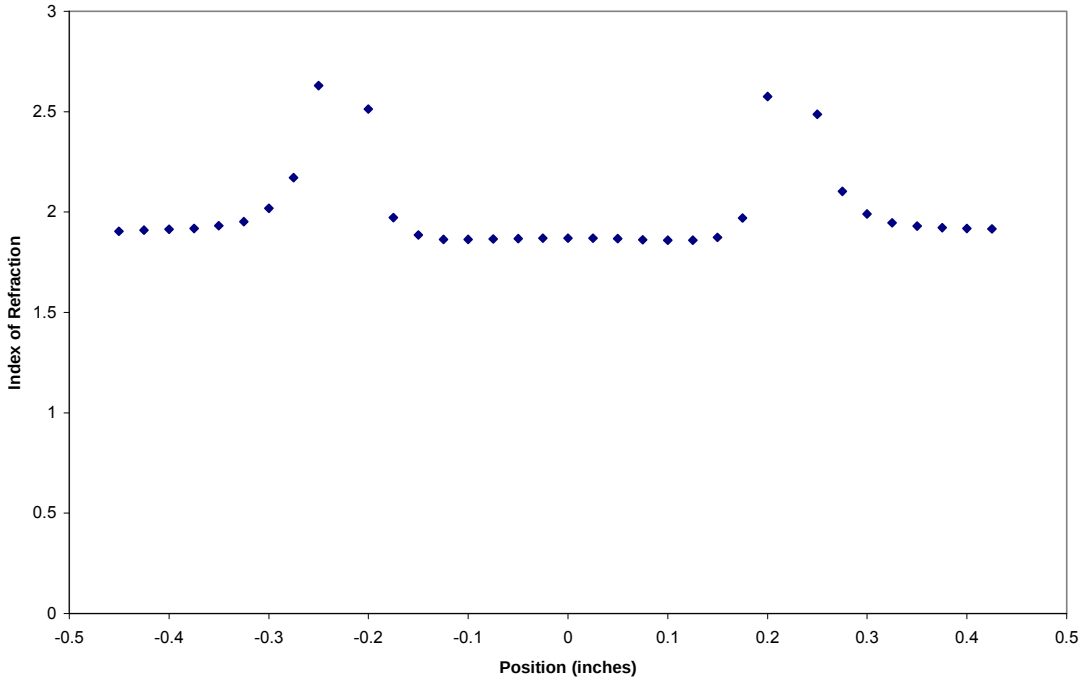

Figure 5.7. Index of refraction calculated from ellipsometric measurements

5.4.2. Thickness Measurements by Scanning Electron Microscopy

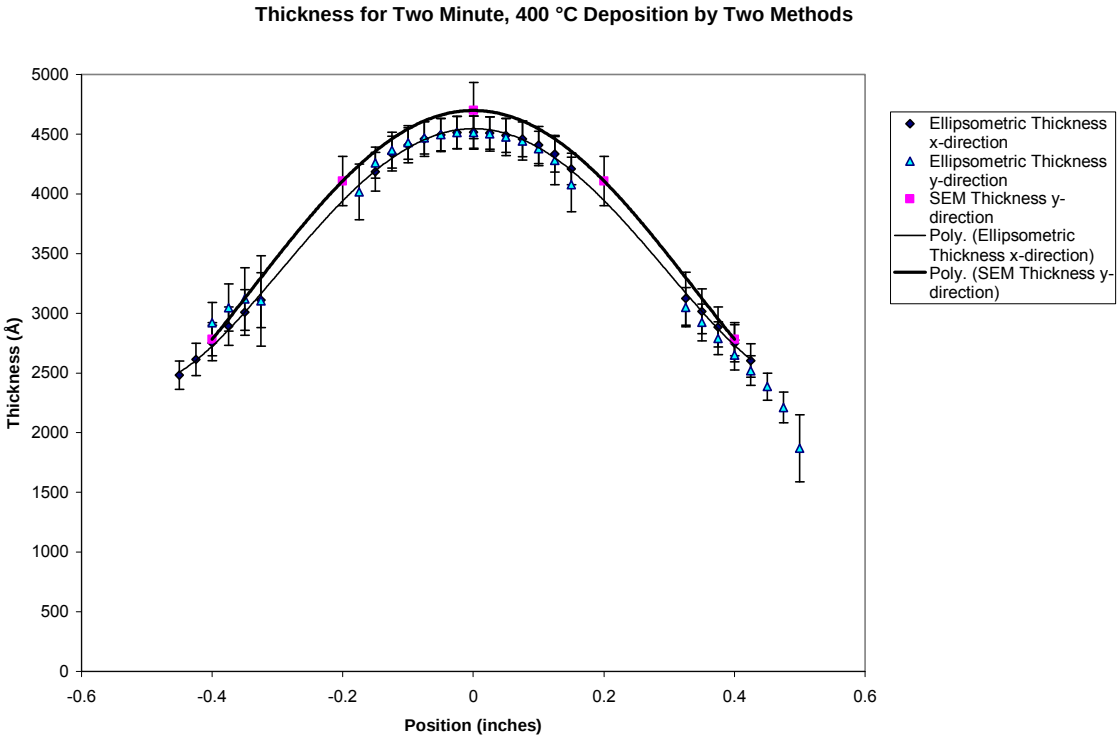

Figure 5.8. Film thickness for a two minute, single-injector LPCVD deposition by SEM and single wavelength ellipsometry

The ellipsometric data were supported by scanning electron microscopy measurements (Figure 5.8). The images were taken at the center point, 0.5 cm and 1 cm from the center of the film, respectively (Figures 5.9-5.11). Imaging was complicated by charging effects, but better images can be obtained by reducing the sample height and increasing the conductive coating thickness. A scanning electron microscope error of 5% was used for error bars in Figure 5.8 due to the poor image quality.

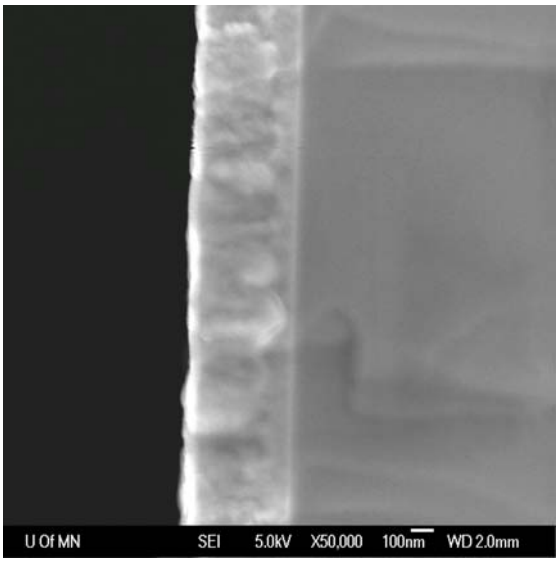

Figure 5.9. SEM cross-sectional image of center of wafer

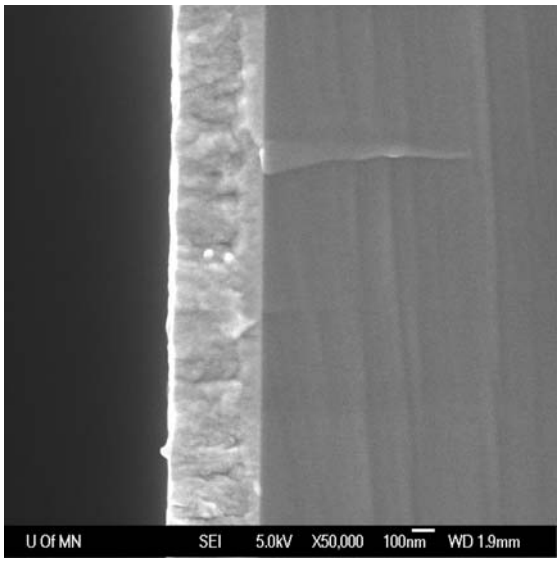

Figure 5.10. SEM cross-sectional image of 0.5 cm from center of wafer

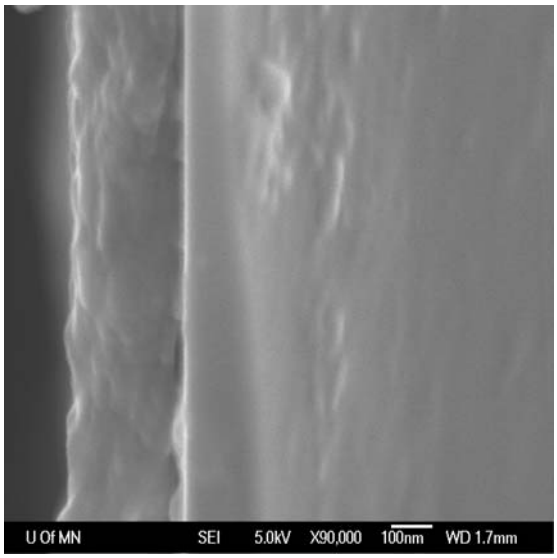

Figure 5.11. SEM cross-sectional image of 1 cm from center of wafer

5.4.3. Precursor and Gas-Phase Product Partial Pressure Experiments

Chamber pressure was measured as a function of temperature during the course of several depositions in the LPCVD reactor (Figure 5.12). The data shown in Figure 5.12 indicate an increase in reactor pressure from 80 to 111 mTorr when the carrier gas was diverted through the ZTB precursor vessel while the susceptor was at room temperature. The increase of 31 mTorr, which was attributed to ZTB, was below the literature vapor pressure of ZTB of 60 mTorr at room temperature[95]. The lower pressure in the reactor due to ZTB was attributed to incomplete saturation of nitrogen with ZTB vapor during its travel through the precursor vessel.

Additional insight into the stoichiometry of ZTB decomposition can be gained from ideal gas calculations using the data from pressure versus temperature

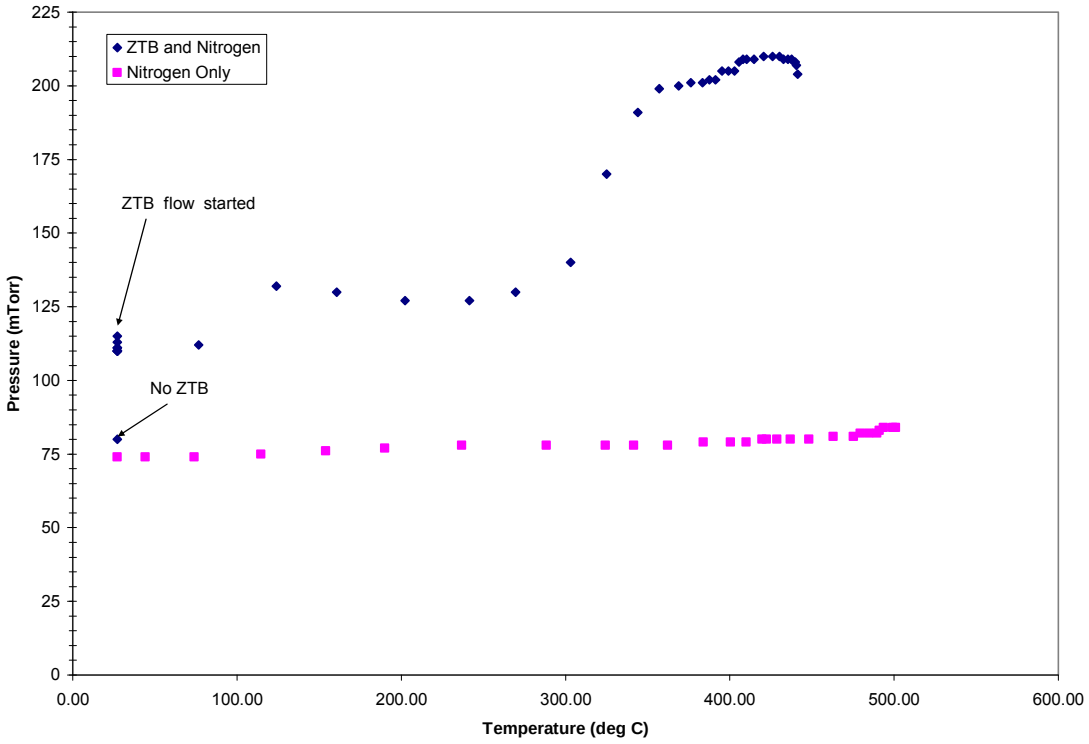

Figure 5.12. Measured pressure (mTorr) in LPCVD reactor versus temperature (°C) showing two experiments, one using nitrogen alone (boxes) and one showing nitrogen and ZTB (diamonds)

measurements. Experiments using a steady nitrogen flow without ZTB demonstrated a pressure increase of less than 10 mTorr when the susceptor was heated from room temperature to 400 °C (Figure 5.12). Similar experiments using ZTB laden nitrogen show an increase of 95 mTorr (Figure 5.12). The chamber pressure at room temperature is due to ZTB and nitrogen. The increase in pressure in the ZTB system when the susceptor is heated to 400 °C is attributed to decomposition by-products. Calculation of an initial gas phase concentration of ZTB by ideal gas theory was possible. Further calculation of the gas concentration at 400 °C allows for determination of ZTB decomposition stoichiometry.

ZTB decomposition yields either 6 moles (Equation 1) or 4 moles (Equation 2) of gas-phase products per mole of ZTB (discussed later). Subtracting the pressure of nitrogen, calculations using the measured pressure at 400 °C (deposition reaction occurring) and the measured pressure at room temperature (no reaction) gives a reaction temperature gas-phase molar concentration of 4.06 times the gas-phase ZTB concentration when no reaction was occurring. As is shown later, most of the ZTB entering the system is pumped out. It was therefore highly unlikely that all of the ZTB was decomposed with unit efficiency to generate 4 times the gas-phase by-product molecule concentration. The decision was made to model the reaction step as follows:

$$Zr[OC(CH_3)_4]\ (ad) \rightarrow ZrO_2(s) + 4\ (CH_3)_2C{=}CH + 2\ H_2O \qquad (1)$$

rather than the alternative:

$$Zr[OC(CH_3)_4]\ (ad) \rightarrow ZrO_2(s) + 2\ (CH_3)_2C(OH)CH + 2\ (CH_3)_2C{=}CH \qquad (2)$$

Undoubtedly both processes are occurring simultaneously via competing reaction pathways; however, for ease of simulation only one route is used in the model.

5.4.4. CFD-ACE Modeling

Surface chemical reactions, mass transport properties, boundary conditions, initial conditions and solver controls were programmed into CFD-ACE with the assumption that no gas phase reactions contributed significantly to the reaction sequence. The three step reaction sequence and corresponding reaction parameters were taken from ultra-high vacuum chemical vapor deposition (UHV-CVD) work by Burleson, *et al.* [96] Gas phase reactions are unlikely in the UHV-CVD work, because the mean free path of the molecules at the pressures studied are larger than the reactor dimensions. The surface chemistry occurring on the substrate is modeled as follows:

(Adsorption)	ZTB(g)	→	ZTB(ad)	(3)
(Desorption)	ZTB(ad)	→	ZTB(g)	(4)
(Reaction)	ZTB(ad)	→	ZrO_2 + Product Gases	(5)

In Burleson, *et al.* the reaction product gases were given as two isobutylene and two isobutanol molecules. Similarly, Cameron and George[97] reported the decomposition of ZTB on a hydroxylated surface to be:

$$ZTB(g) + ZrOH(surf) \rightarrow ZrOH(surf) + ZrO_2 + 2 \text{ isobutylene} + 2 \text{ isobutanol} \quad (6)$$

However Bradley[98] reported a surface catalyzed reaction as follows:

$$ZTB\ (ad) \rightarrow ZrO_2 + 4 \text{ isobutylene} + 2\ H_2O \quad (7)$$

The kinetic parameters reported by Burleson, *et al*. were chosen for use in this simulation; however, the stoichiometry used in the reaction step of the CFD-ACE model was four isobutylenes and two waters evolved per ZTB molecule decomposed.

The general rate of reaction in CFD-ACE's chemical module was:

$$Rate = AT^{n}\exp(-E_a/RT) \quad (8)$$

Where A is the Arrhenius prefactor, E_a is the activation energy, n is a temperature exponent, R is the ideal gas constant and T is the temperature. The parameters A, n, E_a/R are entered into the chemical module. The first reaction step was described as a sticking coefficient reaction with S_o=A=0.0031 from Burleson, *et al.* with a temperature exponent of 0.5 and E_a/R=0.

While no explicit temperature dependence was stated in Burleson, *et al*., according to Muzumder,[99] Mountziaris[100] and Ern,[101] it was appropriate to include a $T^{½}$ term to account for the temperature dependence of the flux of molecules to the surface calculated by kinetic gas theory. In Burleson, *et al*. the gas temperature is constant, which is not necessarily the case in the current study. Because the mean free path of a nitrogen molecule at 200 mTorr is approximately 0.25 mm, the molecules in the LPCVD reactor undergo many collisions over the 9 mm distance from injector to substrate and are not at room temperature due to intermolecular collisions.

As derived from Burleson, the desorption step was described by A=1 x 10^{14} s^{-1} and E_a/R=27061 K^{-1}. The reaction step was described by A=1 x 10^{9} s^{-1} and E_a/R=14793 K^{-1}. Because the kinetic fit parameters taken from Burleson, *et al*. were of the steady state growth, no direct assumption of the chemistry of the growing surface, whether it be hydroxylated, oxygen or metal terminated, was necessary. It was simply assumed that whatever state the surface was in was regenerated by molecular decomposition.

The model took into account the density of material being deposited, the surface density of reactive sites, and the stoichiometry of deposited material. A ZrO_2 density of 5.0 g/cm^3 for a deposition at 400 °C (based on Burleson, *et al.*) was used in the model. Deposited films are often less dense than single crystal solids, and while the processes are not identical, the data from Burleson *et al*. gives a convenient starting point. The density of surface sites was calculated from the bulk density of ZrO_2, 5.7 g/cm^3 via dimensional analysis. The value calculated was 9.2 x 10^{18} molecules / m^2 which was in close

agreement with a density of surface sites calculated for (001) ZrO_2.[102] The density of surface sites was then converted to units of kmole / m^2 for use in CFD-ACE. The stoichiometry of the deposited material is one zirconium atom for every two oxygen atoms.

5.4.4.1. CFD-ACE Solutions

Full color pictorial representations were generated from the output data of CFD-ACE+ of the gas velocity, temperature, pressure and species concentrations using CFD-VIEW. Temperature and species concentrations are presented herein. The velocities calculated in CFD-ACE have a maximum of 60 m/sec, which is much less than the speed of sound. As a result, the Navier-Stokes equation can be used to calculate the velocity of material accurately through the model. The pressure was nearly uniform over the model volume with little pressure exerted by the gas stream on the substrate. The stream function plot (Figure 5.13), which is the path a mass-less particle would follow, indicates that much of the ZTB which enters the system was not converted to ZrO_2 on the surface and was pumped out of the reactor system. From the temperature profile (Figure 5.14), the ZTB molecules are 400 °C by the time that molecule hits the surface due to molecule-molecule interaction on the path to the substrate. As a consequence, gas-phase thermalization may result in gas-phase routes to film formation as discussed later. Figure 5.15 shows the ZTB concentration in the CFD-ACE+ model. Figure 5.16 shows the concentration of the gaseous by-product isobutylene which correlates to the deposition rate at the substrate. The pattern for water concentration is similar.

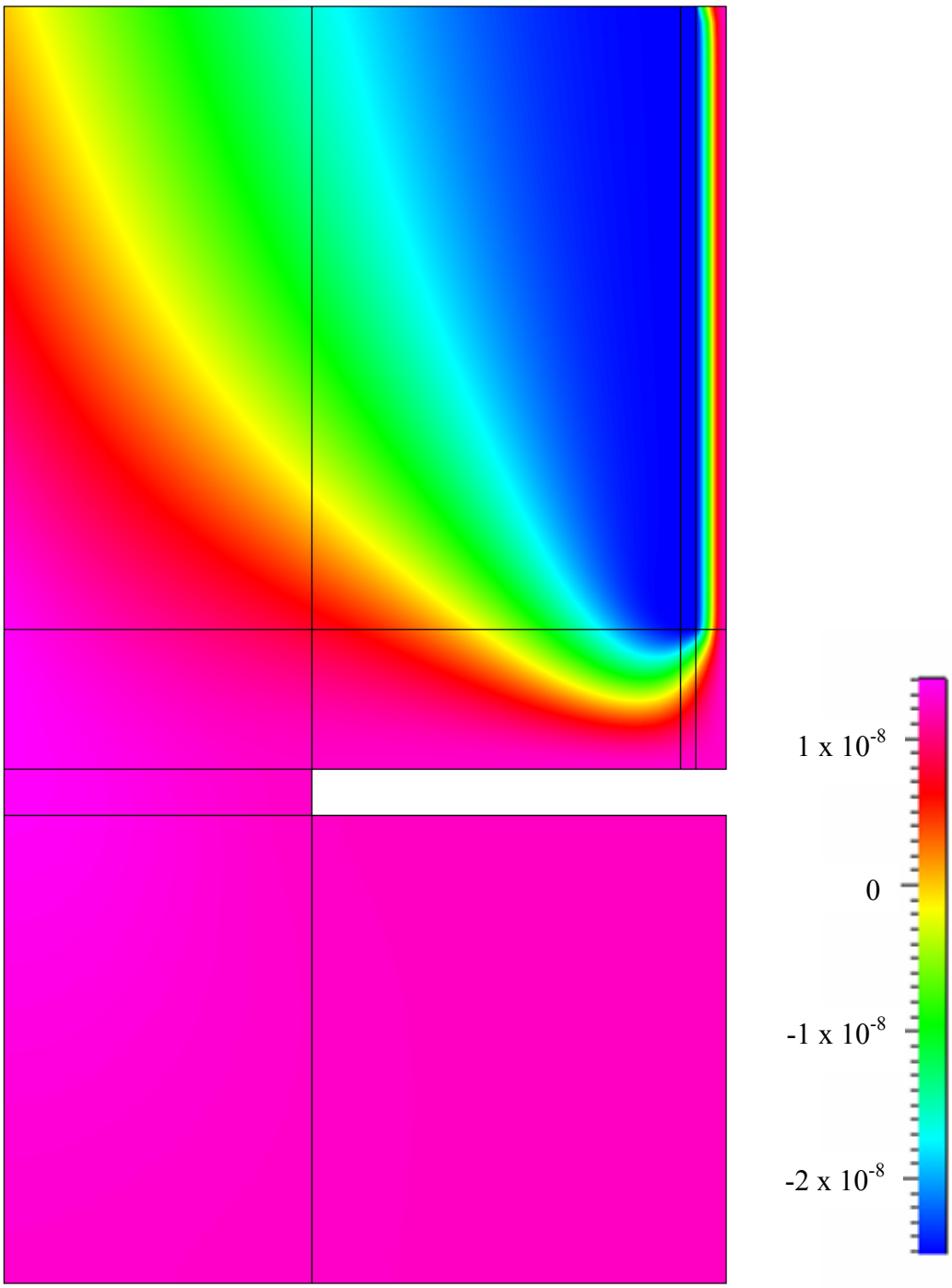

Figure 5.13. Modeled stream function showing paths of travel for gas molecules

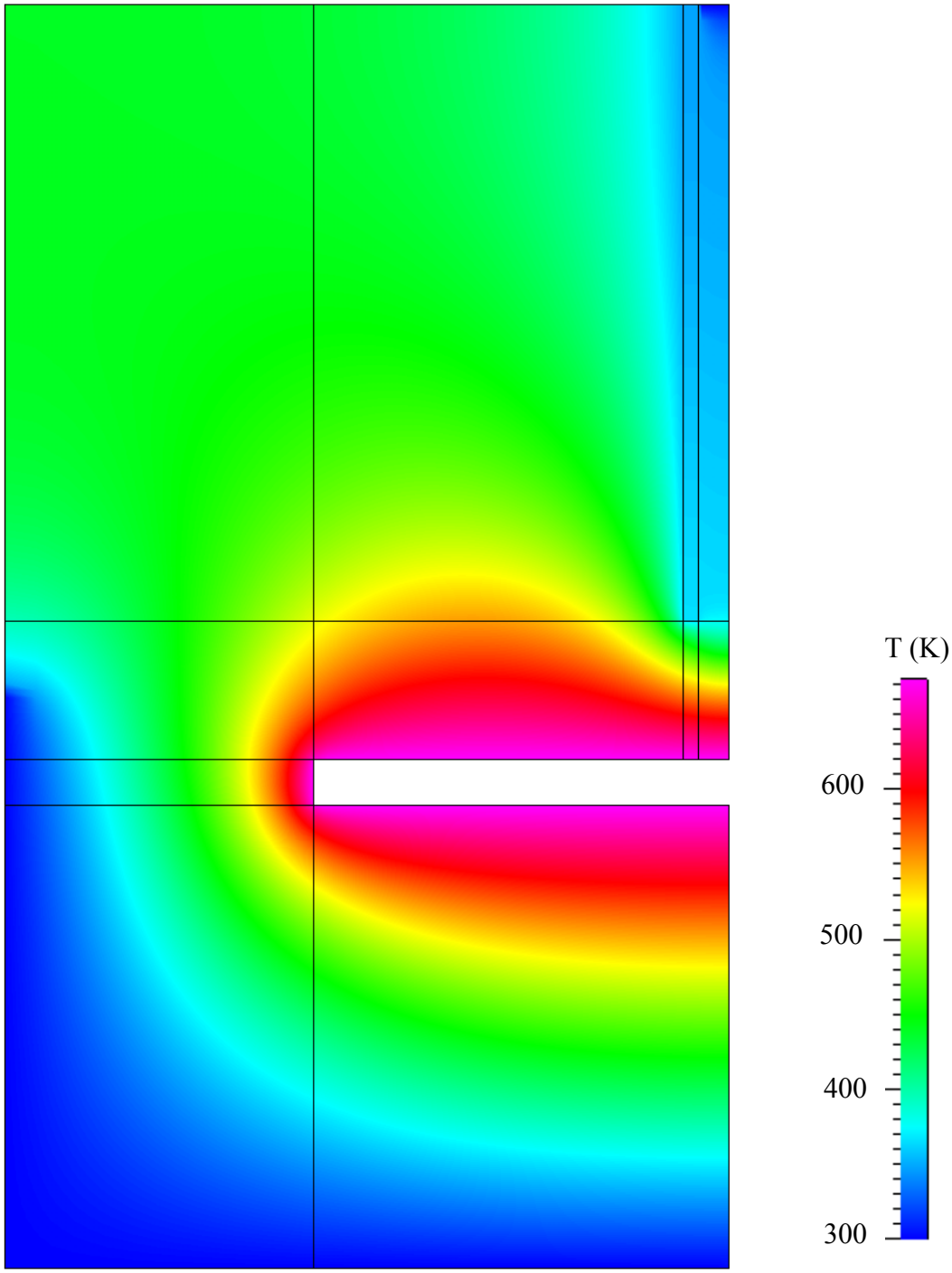

Figure 5.14. Modeled temperature profile (K) demonstrating gas phase temperature in the LPCVD reactor

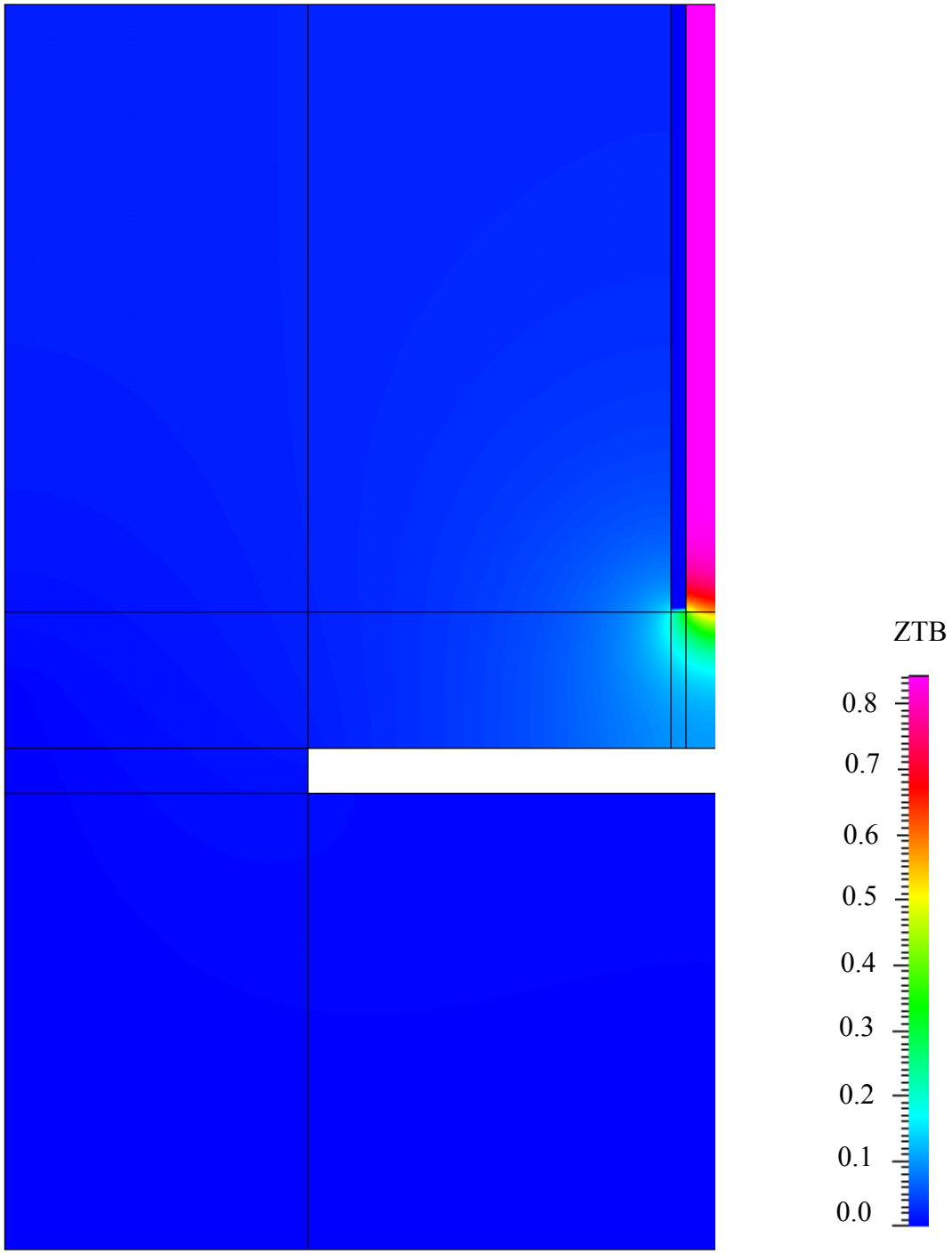

Figure 5.15. Modeled ZTB mass fraction showing depletion of precursor concentration through diffusion

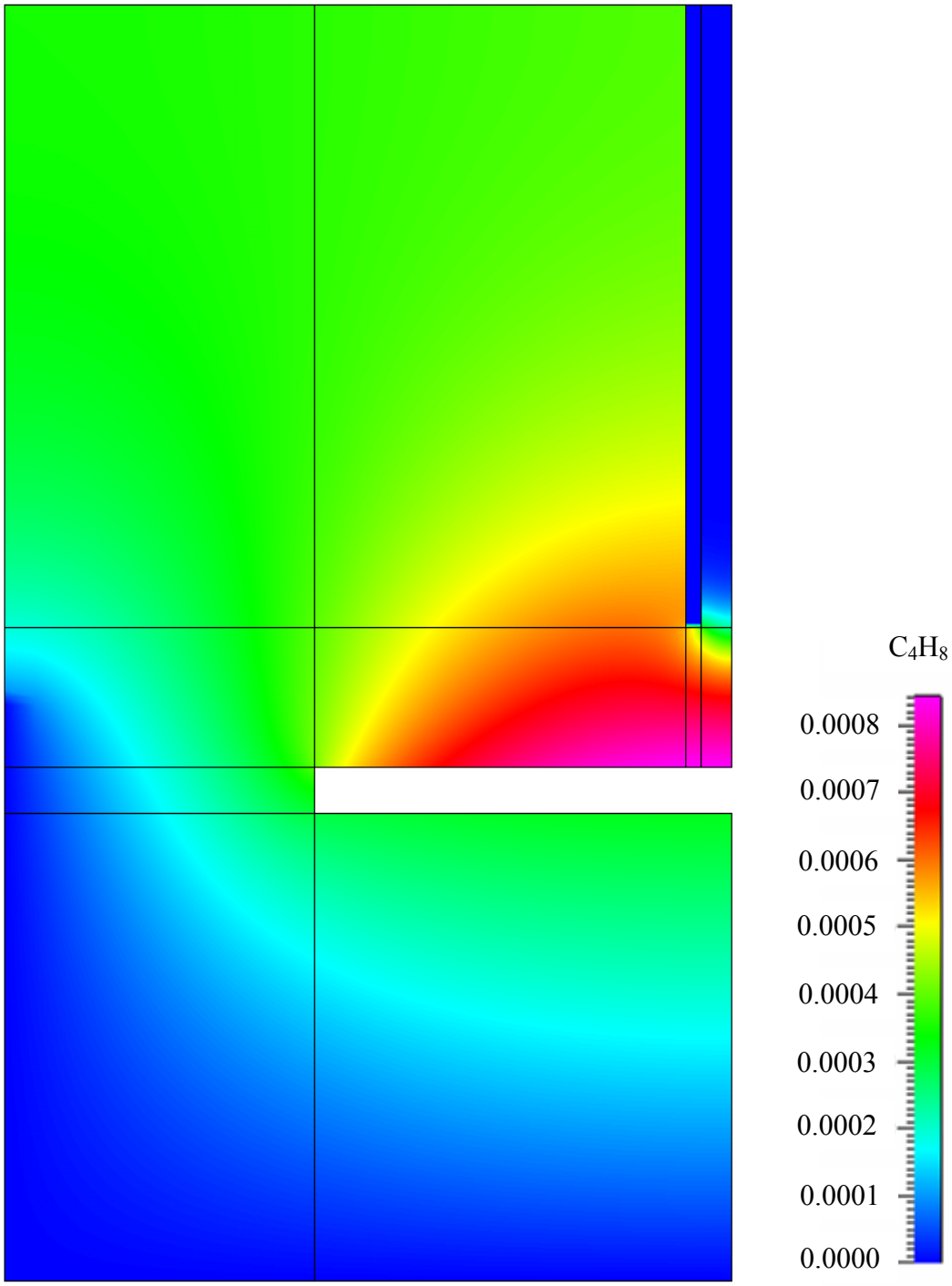

Figure 5.16. Modeled isobutylene mass fraction showing where surface reactions are generating gas-phase by-products. The pattern for H_2O is similar.

5.4.4.2. Calculation of Collision Diameters

The collision diameter of each gas phase molecule was used by CFD-ACE to calculate molecular transport properties. Since the collision diameter of ZTB was not available, a calculation of the collision diameter was made. The collision diameter of the largest molecule in the CFD-ACE library, tetraethylorthosilicate (TEOS), was chosen for use as the ZTB collision diameter. In order to increase the accuracy of the computational model, PCModel was used to calculate collision diameters from molecular volumes generated from Gaussian98W output files. Figure 5.17 shows the optimized structures of TEOS (left) and ZTB (right). From the molecular volumes, an average molecular diameter was calculated, assuming spherical geometry. The optimized molecular diameter of TEOS calculated from PCModel of 7.4 Å was in reasonable agreement with the collision diameter listed in the CFD-ACE library of 7.03 Å. The molecular diameter calculated from the optimized structure of ZTB was 9.4 Å. In order to determine the effect of the increased collision diameter on the CFD-ACE model, a simulation was performed with ZTB collision diameters of 9.4 Å and 7.03 Å. The maximum difference in the deposition rate was approximately 2%. Future work will utilize 9.4 Å as the ZTB collision diameter.

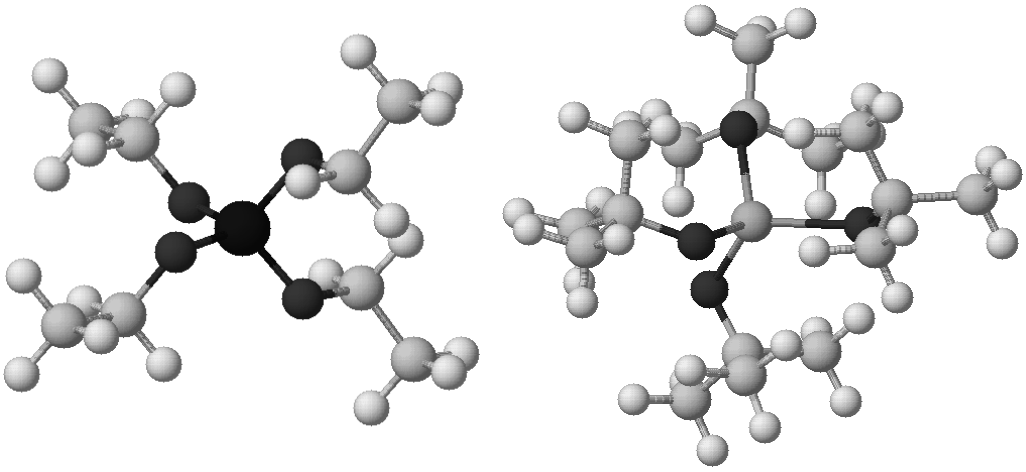

Atom Codes: Silicon (left center), Zirconium (right center), Oxygen (dark gray attached to silicon and zirconium), Carbon (larger gray), Hydrogen (smaller gray)

Figure 5.17. PCModel images of TEOS (left) and ZTB (right) optimized by Gaussian98W

5.5. DISCUSSION

Figure 5.18 shows the computationally predicted deposition rate profiles for many different substrate temperatures. Figure 5.19 presents the same data in a normalized fashion, as to better visualize the effect of temperature on the deposition profile. The deposition rate profile contains information about the process of decomposition and demonstrates how the precursor concentration becomes depleted further from the injector. Figure 5.20 shows the natural log of the predicted maximum deposition rate as a function of inverse substrate temperature. The model predicts the depositions in the LPCVD reactor chamber are occurring in the flux limited regime of CVD film growth.[103,104]

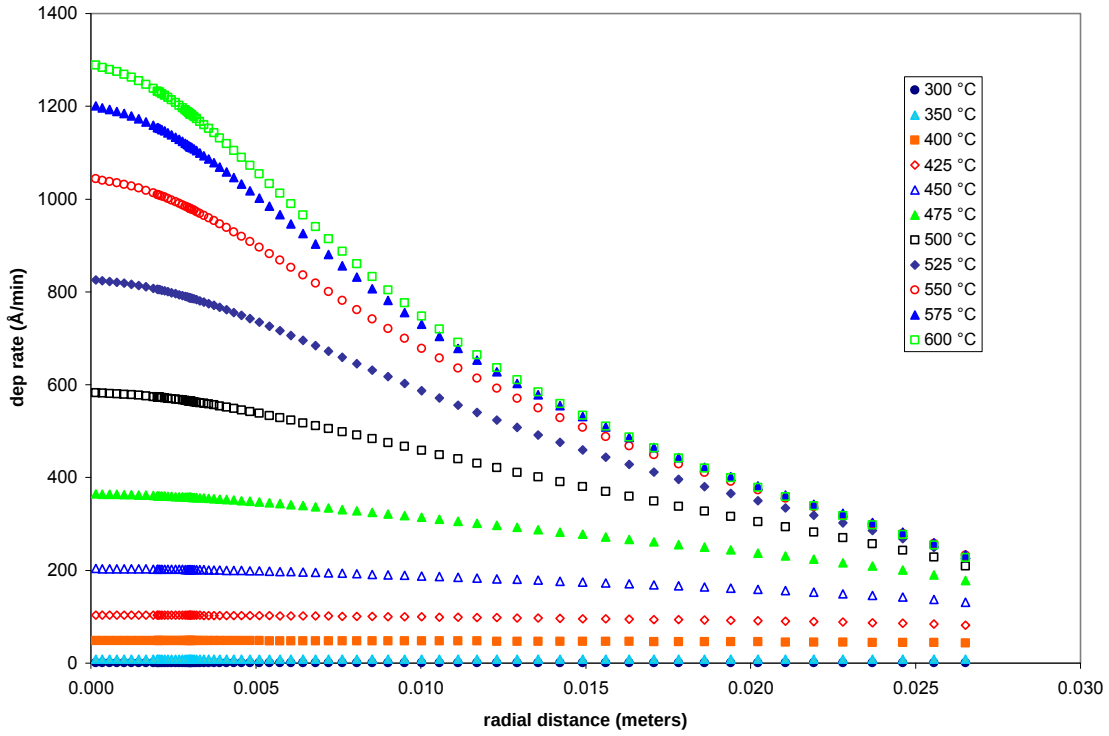

Figure 5.18. Predicted deposition rate (Å/min) as function of radial position (m)

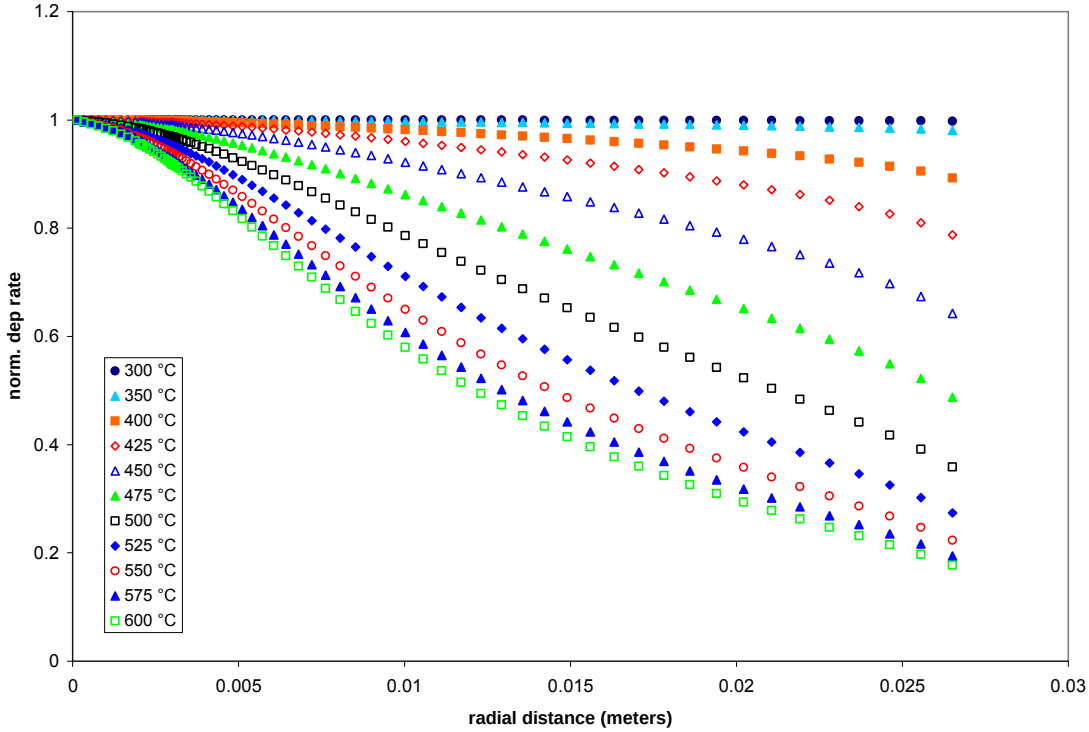

Figure 5.19. Normalized predicted deposition rate as function of radial position (m)

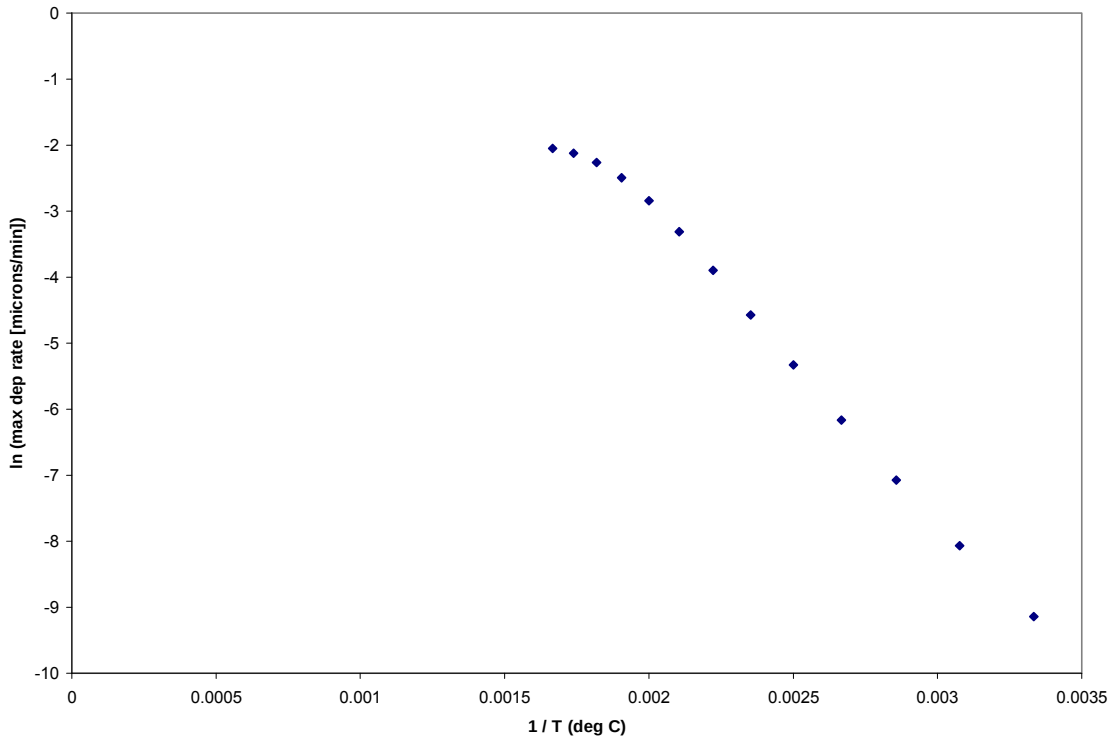

Figure 5.20. Arrhenius activation plot for CFD-ACE results

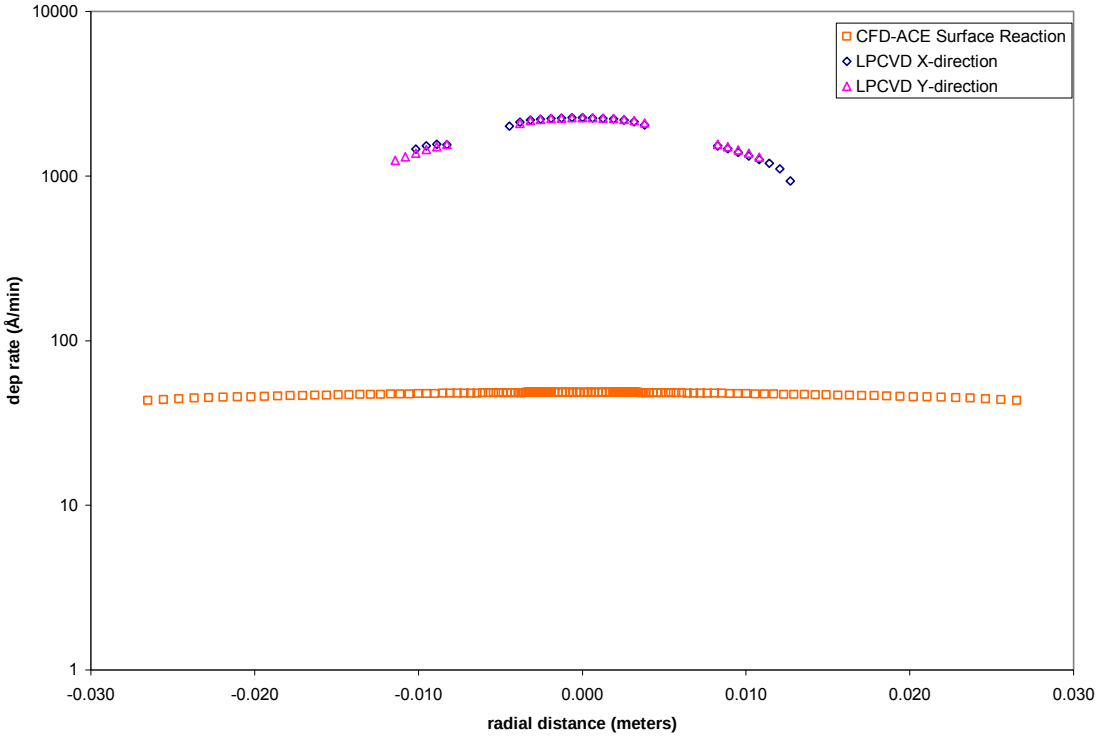

Figure 5.21. Comparison of CFD-ACE and ellipsometric profiles

As shown in Figure 5.21, the deposition rates predicted for 400 °C did not match the experimentally measured deposition rates. Additionally, the 400 °C experimental and predicted profiles do not match. There are at least two possible scenarios that could explain the large difference. One possibility is there are changes in the deposition chemistry, for example, the generation of water as a reaction by-product could catalyze the decomposition of ZTB. Alternatively, there could be gas phase reactions occurring which provide lower energy pathways to decomposition.

Based on the kinetics of Burleson, *et al*., the derivation of which can be found in Taylor, *et al*,[105] one can predict a deposition rate of 61.5 Å / min using a ZTB pressure of 31 mTorr and 400 °C. This value was in reasonable agreement with the CFD-ACE max deposition rate 48.4 Å / min. It was also reasonable for the CFD-ACE maximum rate to be smaller, due to diffusion processes during the nearly one centimeter the precursor molecules travel from injector to substrate. These values are in disagreement with the LPCVD films deposited in the reactor. The maximum measured deposition rate from Figure 5.18 was 2300 Å / min. This suggests that the UHV surface kinetics may not fully describe the chemical reactions occurring at low pressure.

Gas phase reactions may contribute to the observed difference in deposition rate between calculated and measured rates. If the precursor material entering the reactor were converted to product at higher percentages, the predicted deposition rates would increase. Increased deposition rates could be achieved by altering the surface reaction's kinetic parameters or by adding a gas phase reaction, allowing an alternate lower energy path to deposition. Because the good agreement in literature values of surface decomposition, it was not desirable to alter the surface kinetic parameters.

5.6. CONCLUSION

Experiments have been performed using the LPCVD reactor to determine model parameters such as mass flow rate, species mass percentages, background pressure and deposition temperature. Additionally, single-injector depositions were performed in the LPCVD reactor. The resultant films were analyzed for film thickness by ellipsometry,

and the ellipsometric results corroborated with scanning electron microscopy images. The results established the axi-symmetric nature of the deposition process. Comparison of the deposited film profiles to computational fluid dynamical modeling results has been done.

A computational fluid dynamic model of the combinatorial LPCVD reactor has been constructed using the CFD-ACE+ suite of programs, and investigation of the fluid dynamics and chemistry occurring in the LPCVD reactor has been undertaken. A two-dimensional, axi-symmetric model of the zone of interest in the LPCVD reactor has been created, populated with a finite element mesh and used to predict deposition rates, as well as other physical parameters such as pressure, temperature, gas concentrations and stream lines.

5.7. APPENDIX I: Details of Construction of Combinatorial LPCVD Reactor

The current reactor was constructed from vacuum grade stainless steel. A six-way 4 ½ inch outer diameter ConFlat cross (CR-250-6, Thermionics) was used as the main deposition chamber. The front opening of the cross was fitted with a 4 ½ inch Conflat door with viewport (QD-450-VP, MDC) allowing for loading and unloading of samples when the chamber was vented to atmospheric pressure. The bottom opening of the cross was fitted with a quartz IR window (CFQ G&P Disk, 3 ½" x ¼", from GM Associates) and sealed with a 4 ½ inch Viton gasket (VG-450-1, Duniway). Clamps were used to keep the gasket held in place during venting to atmosphere for access to the main chamber.

An IR heating lamp consisting of a cylindrical (5 ¾ inch diameter, 6 ¾ inch height) aluminum housing with a 1000 watt quartz lamp (FEL-120v-1000w, BulbDirect.com) was constructed from a previous design by the University of Minnesota's Physics machine shop. The housing was designed such that the filament of the lamp was at the focus of a parabolic reflector milled from the center of a 5 ¾ inch aluminum cylinder. The reflector was used as received with no additional polishing. The parabolic reflector provided maximum illumination to a molybdenum susceptor in the chamber. A two inch diameter molybdenum susceptor with four ⅛ inch thick, ⅞ inch long supports was machined from one sixteenth inch molybdenum sheet stock by the University of Minnesota Physics machine shop. A small diameter hole (approximately one thirty second inch) was drilled in the side of the susceptor for a thermocouple to be attached.

Type K thermocouples were hand-made from Alumel and Chromel wire stock. One type K thermocouple was placed approximately ¼ inch from the edge of the susceptor and cemented into place with high temperature cement (Omegabond "600", Omega Engineering, Inc). The thermocouple was fed to the outside of the chamber through the left side of the cross which was fitted with a 1 ⅓ inch Conflat type K thermocouple feed-through with two thermocouple capacity (FETC-1332K, Thermionics). The thermocouple feed-through was coupled to the chamber with a 4 ½ inch to 1 ⅓ inch Conflat reducing nipple (RN450-133, Thermionics). A Fluke 50D K/J

two lead thermometer was purchased from Tequipment.net and was calibrated using ice water.

The right port on the cross was fitted with a 4 ½ inch double sided Conflat flange (D-450250, Thermionics) with a hole drilled through its side and a ¼ inch VCR gland with female nut welded to the flange around the through hole for pressure measurements. This flange was capped with a zero profile, wide angle 7056 glass viewport (ZPV-250, Thermionics). Pressure measurements are performed using a thermocouple pressure gauge (DST-531) with meter (TCG-531 BOX, Duniway). An adaptor was made by the University of Minnesota Physics machine shop to convert the NPT fitting on the pressure gauge to the VCR fitting on the vacuum feed through.

The top port on the cross was fitted with a 4 ½ inch double sided Conflat flange (D-450250, Thermionics) altered into a four port CVD injector head (University of Minnesota Physics machine shop) and capped with a zero profile, wide angle 7056 glass viewport (ZPV-250, Thermionics). The injector head had four ¼ inch VCR glands with male nuts attached to the outside of the flange. These fittings attach to the gas delivery lines for injection of precursor gases. Each VCR gland was attached to ¼ inch stainless steel lines and fed through the Conflat flange with appropriately sized holes and welded into place. Three fittings are attached to ¼ inch stainless steel tubes which are directed perpendicular to the substrate. The stems are located at the end points of an equilateral triangle of length ¾ inch and terminate approximately 1 cm from the surface of the susceptor. The fourth VCR feed through does not have an injector stem, but terminates in an openening just inside the Conflat flange's inner edge. This port is used to inject gases into the chamber which are to have uniform concentrations within the chamber.

The back opening of the six way cross is attached to a 4 ½ inch Conflat manual right angle valve (AV250, 310037, MDC) which directs the flow in the downward direction. The downward side of the right angle valve is attached to a 4 ½ to 2 ¾ inch conical connector (FCR450275, 4022032, MDC) which is in turn attached to 1 ½ inch thick, 2 ¾ inch double sided Conflat flange (FD275150-1,140014, MDC) and then to a 3 foot, 2 ¾ inch Conflat flexible vacuum hose (spare parts). The 2 ¾ inch double sided Conflat flange had two ¼ inch VCR glands with male nut feed throughs for attachment of

purge gas lines (to vent the chamber to atmospheric pressure with dry nitrogen) and/or additional vacuum gauge equipment. The flexible Conflat vacuum line is attached to a 2 ¾ inch Conflat 90 degree adaptor (spare parts) and then to the cracker furnace tube.

The cracker furnace tube is made by the University of Minnesota's glass shop from three parts, two 1 inch OD quartz tube on 2 ¾ inch Conflat flanges (SQ-100-F2, 216122, Larson Electronic Glass) and 1 inch stock quartz tube (University of Minnesota glass shop). The overall length of the cracker heater tube is approximately 28 inches of glass from the inside edges of the Conflat flanges. The cracker heater, used to decompose any precursor gases not decomposed in the reaction chamber before they enter the pump and react with the pump oil, is a Lindberg Heavi-duty tube furnace (spare parts) controlled by an Omega series 6000 microprocessor based temperature controller, which was built in-house into a housing with one type-K thermocouple input and a high amperage output (spare parts). The thermocouple used is a quick disconnect type K thermocouple probe with high temperature mini connector (HKMQSS-062U-12, Omega Engineering, Inc) and is placed between the insulated areas of the Lindberg furnace to prevent shorting of the heating elements with the thermocouple.

After the cracker heater, the Conflat style flanges are converted to Kwik Flange style connects with a 2 ¾ inch Conflat to NW25 KwikFlange adaptor (100x275, 730002, MDC). Following is a 3 ½ inch NW25 flexible coupling (722001, MDC) to a 90 degree NW25 adaptor (spare parts), particle filter (AV-104202, Kurt J. Lesker), auto-shut off valve (HPS Vacuum Sentry, spare parts), micromaze (MMA-102-2QF, Kurt J. Lesker), and Leybold Trivan B rotary vane vacuum pump S/D 16, 25B (spare parts). The micromaze was baked out under nitrogen purge using the built-in heater prior to use.

The LPCVD reactor is equipped with an automated gas handling system. Reaction grade nitrogen is introduced into the gas handling system through copper tubing from a high purity tank through a 30 psi max line regulator (3702-510, Matheson) with an output pressure limited to 2 psi above atmospheric pressure. The input gas goes through a manual bellows valve (SS-4BG-V51, Minnesota Valve) and into a distribution line which feeds four separate precursor lines. A manual bellows valve separates each precursor line from the front end distribution line so that only the lines required for each

deposition are fed with nitrogen. Behind the manual valve, the flow of nitrogen into the line is controlled by a mass flow controller (MFC). Lines one, two and three are controlled by 100 sccm MFC's (UFC-1660, Unit Instruments) and line four is controlled by a 300 sccm MFC (UFC-1600, Unit Instruments). The mass flow controllers are regulated by a URS-100 (Unit Instruments) control box which determines the mass flow of gas allowed by each MFC.

Each line is equipped with three pneumatic control bellows valves (SS-4BK-V51-1C), two of which are on either side of a precursor vessel and one is on the precursor by-pass. The pneumatic valves are controlled using LabView and a 16 channel high voltage / current PCI board (PCI-PDI-S016, Omega Engineering) mounted in a Dell computer with a Pentium III processor. The output board controls eight DIN-Rail mounted manifolds (SVP-1, Omega Engineering) which allow conversion of electrical signals to pneumatic signals. A control box was constructed in the University of Minnesota Chemistry electronics shop to allow electrical interface from the computer board to the gas manifolds. Each line is controlled by two manifolds, one gates the two precursor valves and one gates the by-pass valve. When fired in unison, the flow of gas is diverted from the by-pass line through the precursor vessel and into the injector mounted in the LPCVD chamber.

Each precursor vessel is approximately 12 inches tall, with two manual bellows valves (SS-4BG-V51, Minnesota Valve), one at the inlet and one at the outlet. The manual valves on the precursor vessel allow the vessel to be sealed from atmosphere for entrance and exit into a nitrogen glove box for utilization of air and moisture sensitive precursors. The precursor vessel is constructed in two pieces. The top piece has a ¼ inch VCR fitting, for attachment of a manual valve (SS-4BG-V51, Minnesota Valve), a ½ inch VCR fitting, for attachment to the lower half of the vessel, and a ¼ inch stainless steel stem which fits down into the lower half of the vessel, terminating approximately ½ inch from the bottom of the lower half's glass bulb. The lower half of the vessel has a ½ inch VCR fitting for sealing to the upper half of the vessel, a glass to metal seal, a glass bulb of approximately 46 mm outer diameter and a ¼ inch VCR male nut and gland exiting perpendicularly from the metal housing of the glass to metal seal.

The entire construction is assembled so that the carrier gas inlet stem is in close proximity to the precursor material, where the carrier gas becomes laden with precursor and travels out the perpendicular stem into the delivery system. Flexible vacuum lines (321-4-X-12-DMR and 321-4-X-24-DFR, Minnesota Valve) connect the precursor vessel to the gas handling system and the gas handling system to the main reactor chamber.

5.8. Appendix II: Details of CFD-ACE Solver Mathematics

CFD-ACE+ is a multi-physics module that solves the Navier-Stokes (conservation of momentum), continuity (conservation of mass), enthalpy (conservation of energy) and Stefan-Maxwell (conservation of species) equations simultaneously through a finite volume approach. These equations are listed below in vectorial form [1,9]:[106]

Momentum: $$\frac{\partial \rho \mathbf{u}}{\partial t} + \nabla \cdot \rho \mathbf{u}\mathbf{u} = -\nabla p + \nabla \cdot \tau + \rho \mathbf{g} \quad (9)$$

Mass: $$\frac{\partial \rho}{\partial t} + \nabla \cdot \rho \mathbf{u} = 0 \quad (10)$$

Energy: $$\frac{\partial \rho h}{\partial t} + \nabla \cdot \rho \mathbf{u} h = \nabla \cdot \mathbf{q} + \tau : \nabla \mathbf{u} + \frac{\mathrm{d}p}{\mathrm{d}t} \quad (11)$$

Species: $$\frac{\partial \rho Y_i}{\partial t} + \nabla \cdot \rho \mathbf{u} Y_i = \nabla \cdot \mathbf{j}_i + \omega_i \quad (12)$$

Where ρ, **u**, p, h and Y_i are density, velocity, pressure, enthalpy and species mass-fractions, respectively, and ω_i is the species production rate per unit volume due to gas-phase reactions. The auxiliary quantities in the above equations may be written as:

Sheer stress: $$\tau = \mu(\nabla \mathbf{u} + \nabla \mathbf{u}^T) - \frac{2}{3}\mu(\nabla \cdot \mathbf{u})\mathbf{I} \quad (13)$$

Diffusive Energy Flux: $$\mathbf{q} = \lambda \nabla T + \sum_i h_i \mathbf{j}_i \quad (14)$$

Diffusive Species Flux: $$\mathbf{j}_i = \mathbf{j}_i^c + \mathbf{j}_i^T \quad (15)$$

Stefan-Maxwell Diffusion: $$\mathbf{j}_i^c = \rho D_i \nabla Y_i + \frac{\rho Y_i}{M} D_i \nabla M - M \sum_j D_j \nabla Y_j - \nabla M \sum_j D_j Y_j \quad (16)$$

Soret Diffusion: $$\mathbf{j}_i^T = \frac{\rho D_i^T}{T} \nabla T - \rho Y_i \sum_j \frac{D_j^T}{T} \nabla T \quad (17)$$

where μ is the dynamic viscosity, λ is the thermal conductivity, T is the temperature, h_i are the species enthalpies, D_i are the species diffusivities, D_i^T are the species thermal diffusivities and M is the mixture molecular weight.

Solutions to these equations are generated through a finite volume approach which entails iteratively solving several continuous, simultaneous equations by breaking down a given model into individual three-dimensional spaces. Solutions to the relevant equations can be developed through computational methods that first approximate a set of rough solutions in each volume and then mathematically refine the solutions to minimize the amount of variation in each iterative cycle by taking into account the properties of the adjacent cells. The addition of user-defined surface and gas-phase chemical reactions allows a deposition rate to be calculated through a multi-step reaction sequence.

CFD-ACE uses both structured and unstructured geometric meshes to break an analytical volume into finite volumes. A structured mesh is one in which all elements are trapezoidal, versus an unstructured mesh which can have triangular and irregular shapes. Unstructured meshes are computationally more expensive and are often used to subdivide geometries which are complex or have curved surfaces. The rectangular nature of the current model lent itself well to structured meshes. It was important to have sufficient density of volume elements near the surface to allow the solver to model the deposition process adequately. It was also important to have sufficient density of volume elements near large changes in physical properties, such as near the end of the injector stem. In CFD-ACE's two-dimensional modeling, the finite volume elements had the length and width as determined by the mesh and a depth of one radian.

5.9. Appendix III: CFD-ACE Parametric Details

Determination of Mass Transport Parameters

The mass flow rate for material into the system was governed by the mass flow controllers. However, this measurement does not take into account the amount of mass of precursor carried into the reactor by the stream of carrier gas, because the mass flow

controller was upstream of the precursor vessel. The study of reactor pressure versus temperature, shown in Figure 5.12, showed the pressure in the chamber due to ZTB was 31 mTorr. From this pressure and the background pressure of nitrogen in the system, 80 mTorr, we can calculate the ratio of ZTB / N_2 molecules in the chamber. Assuming equal pumping speeds for each gas, this determines the mole ratio of gases entering the chamber.

Using the pressures from nitrogen carrier gas only entering the reactor to when the flow was diverted through the ZTB precursor vessel, a molar percentage of 72% nitrogen and 28% ZTB was calculated. Conversion from mole ratio to mass ratio skewed the value substantially in favor of ZTB, owing to the molecular weight of 383 grams per mole versus molecular nitrogen's 28 grams per mole. This calculation gave 84% ZTB and 16% nitrogen by mass entering the reactor through the injector stem. Multiplication by the mass flow rate of nitrogen, as measured by the mass flow controllers, allowed an overall mass flow rate of material entering the chamber to be estimated.

The value used in the model was a total mass flow rate of 3.75×10^{-8} kg/(radian sec) with a mass ratio of 84% ZTB and 16% N_2.

Mass transport properties needed to be determined for the precursor molecule used in this study, zirconium tetra-*tert*-butoxide (ZTB). Because the mass transport properties of ZTB are not known, some estimate of the appropriate mass transport parameters needed to be made. The largest molecule in the CFD-ACE library was chosen, tetraethoxysilane, and the known differences in properties, the molecular weight and atomic composition, were adjusted to match ZTB. See Table 5.3 for the mass and thermal properties used for each molecule used in the model.

CFD-ACE+ calculated densities of gases in the reactor model from ideal gas theory using the respective molecular weights for each gas molecule. Gas viscosities were calculated from kinetic theory by CFD-ACE+.

While ZTB was substantially heavier than TEOS, the overall size of the molecules was similar, due to the branching of the *tert*-butoxide ligand. The simulated deposition rates reported in this paper used the unaltered collision diameter of TEOS from the CFD-ACE library, 7.03 Å.

Table 5.3. CFD-ACE+ Species Parameters

	ZTB	ZrO_2	N_2	H_2O	C_4H_8
Accomodation Coefficient	0.9317	0.9317	0.9317	0.9317	0.9317
Thermal Accomodation Coefficient	0.9317	0.9317	0.9317	0.9317	0.9317
Molecular Weight (kg/kmole)	383	123	28	18	56
Characteristic Energy (K)	522.7	2954	71.4	809.1	357
Collision Diameter (Å)	7.03	3.706	3.8	2.64	5.179
Polarizability (Å)	1.642	1.642	1.642	1.642	1.642
Charge Exchange Cross Section ($Å^2$)	40	40	40	40	40

Determination of Boundary Conditions

Boundary conditions at the susceptor were set for an isothermal value of 400 °C, and the previously defined surface chemistry was activated on the susceptor surface. Surface deposition was allowed on all sides of the susceptor as well as the injector stem. Since most of the reactor was already covered in a fine layer of metal oxide due to previous deposition experiments, modeling deposition parameters for these surfaces as

steady state decomposition on zirconia was not unreasonable.

The injector stem was given material properties of stainless steel as listed in the CFD-ACE+ library. Heating of the injector stem was allowed by convection, as well as cooling by the inlet gases. The mass flow rate and mass ratio of ZTB to N_2 at the injector inlet was given as listed above and the temperature of the inlet gas was 25 degrees Celsius. The pressure at the inlet was not required to be specified when using a mass flow rate formulism.

Values taken from the measured pressure versus time and temperature experiments were used to determine the boundary conditions at the outlets of the reactor model. A background pressure of 24 Pascal was specified at the outlets of the model. Gravity was activated in the negative x-direction. In order for CFD-ACE+ to utilize axi-symmetric models, the axis of symmetry must be on the x-axis. By specifying gravity in the negative x direction, the reactor geometry was as experienced in the LPCVD reactor. All images in this publication of the CFD-ACE model have been rotated 90°, so the x-direction is vertical.

Determination of Initial Conditions

Because of the complexity of the calculations in CFD-ACE+, it was important to create the solution to the model in steps to ensure convergent solutions. The initial step was to use the geometric model to solve the flow of material only. The relative difficulty of this step was very low; however, it gave confidence that the geometry and model mesh were appropriate. Next, the heat module was activated and a solution was calculated which involved computation of heat and flow. This step additionally insures no complications in the fluid dynamical solution utilized in the final model. Finally, the chemistry module was activated. Inlet mass fractions and mass flow rates were programmed, as well as outlet boundary conditions and surface reactions, as previously mentioned. Initial conditions for most of the reactor were set to be nitrogen at 25 °C. Initial conditions for the injector stem and zones just below were set to the same mass fraction of ZTB and nitrogen as given for the inlet. While the final solution of the model

did not explicitly depend on the initial conditions, starting with accurate initial conditions ensured quick convergence of the iterative solver.

Iterative Solver Parameters

The iterative solver included separate adjustments for each calculated property. By observing the residuals, calculation cycle remnants similar to remainders in integer division, a determination was made as per whether the solution was achieving convergence. Small residuals indicate good solutions; however, too aggressive of solver parameters may cause unstable solutions. The mathematical scheme used in this work was an upwind solver, meaning the calculation routine used the parameters from the upwind cells to refine the values in the cell being calculated. The upwind direction began at the injector inlet and terminated at the outlets of the model. The parameters, such as step size, in the solver for each property were adjusted for optimal convergence of solution.

5.10. APPENDIX IV: Ellipsometric Equations

Ellipsometry provides values of Ψ and Δ. Ψ is the amplitude shift of the parallel (p) and perpendicular (s) light waves, and Δ is the phase angle, or phase difference between the parallel (p) and perpendicular (s) light waves. These values are derived from physical measurements of intensities and amplitudes of the reflected waves as a function of polarization angle.

$$\tan\Psi = \frac{|R^p|}{|R^s|} \tag{18}$$

$$\tan\Psi e^{i\Delta} = \frac{\Re^p}{\Re^s} \tag{19}$$

where R^p, R^s are wave amplitudes of the parallel and perpendicular wave and $\Re^p, \Re^s$ are the intensities of the perpendicular and parallel wave components. R^p and R^s are related to $\Re^p$ and $\Re^s$ through the relationship:

$$\frac{\Re^p}{\Re^s} = \frac{|R^p|^2}{|R^s|^2} \tag{20}$$

These values are correlated to the thickness and index of refraction of a dielectric film on a dielectric substrate.[107] The solutions to the equations are cyclical, giving rise to multiple potential solutions of thickness and index of refraction. The correct thickness, or ellipsometric order, must be chosen in correlation with other information.

6. BIBLIOGRAPHY

[1] B.O. Field and C.J. Hardy, *Proc. Chem. Soc.* **1962** 76

[2] C.C. Addison and N. Logan, *Adv. Inorg. Chem. Radiochem.* **1964** 6, 72

[3] a) Zhang, Wen-Qi; Huang, Liu-Ying; Li, Ai-Dong; Shao, Qi-Yue; Wu, Di., *Integrated Ferroelectrics* **2008**, 97, 93-102 b) Shao, Qi-yue; Yuan, Tao; Li, Ai-dong; Dong, Yan; Fang, Feng; Jiang, Jan-qing; Liu, Zhi-guo., *Gongneng Cailiao* **2008**, 39(4), 574-577 c) Shao, Qi-Yue; Li, Ai-Dong; Zhang, Wen-Qi; Wu, Di; Liu, Zhi-Guo; Ming, Nai-Ben., *Materials Research Society Symposium Proceedings* **2006**, 917E(Gate Stack Scaling--Materials Selection, Role of Interfaces, and Reliability Implications) d) Shao, Qi Yue; Li, Ai Dong; Dong, Yan; Fang, Feng; Jiang, Jian Qing; Liu, Zhi Guo., *Applied Surface Science* **2008**, 254(8), 2224-2228 e) Gladfelter, Wayne L.; Moersch, Tyler L.; Xia, Bin; Boyd, David C.; Yu, Dan; Campbell, Stephen A.**,** *Abstracts of Papers, 234th ACS National Meeting, Boston, MA, United States*, August 19-23, **2007** f) Shao, Qiyue; Li, Aidong; Zhang, Wenqi; Wu, Di; Liu, Zhiguo; Ming, Naiben., *Chemical Vapor Deposition* **2006**, 12(7), 423-428 g) Zhong, Lijuan; Zhang, Zhihong; Campbell, Stephen A.; Gladfelter, Wayne L. *Journal of Materials Chemistry* **2004**, 14(21), 3203-3209 h) Xia, Bin; Chen, Fang; Campbell, Stephen A.; Roberts, Jeffrey T.; Gladfelter, Wayne L., *Chemical Vapor Deposition* **2004**, 10(4), 195-200 i) Xia, Bin; Smith, Ryan C.; Moersch, Tyler L.; Gladfelter, Wayne L., *Applied Surface Science* **2004** 223(1-3), 14-19 j) Xia, Bin; Smith, Ryan; Chen, Fang; Campbell, Stephen A.; Gladfelter, Wayne L.**,** *Materials Research Society Symposium Proceedings* **2003**, 765(CMOS Front-End Materials and Process Technology), 33-37 k) Gladfelter, Wayne L.; Xia, Bin; Chen, Fang; Campbell, Stephen A.; Roberts, Jeffrey T., *Proceedings - Electrochemical Society* **2003**, 2003-8(Chemical Vapor Deposition XVI and EUROCVD 14, Volume 2), 829-838 l) Smith, Ryan C.; Hoilien, Noel; Roberts, Jeffrey T.; Campbell, Stephen A.; Gladfelter, Wayne L., *Advances in Science and Technology* (Faenza, Italy) **2003**, 32(10th International Ceramics Congress, 2002, Part C), 27-35 m) Smith, Ryan C.; Hoilien, Noel; Chien, Jimmy; Campbell, Stephen A.; Roberts, Jeffrey T.; Gladfelter, Wayne L., *Chemistry of Materials* **2003**, 15(1), 292-298 n) Smith, Ryan C.; Hoilien, Noel; Roberts, Jeff; Campbell, Stephen A.; Gladfelter, Wayne L., Chemistry of Materials **2002**, 14(2), 474-476 o) Ma, Tiezhong; Campbell, Stephen A.; Smith, Ryan; Hoilien, Noel; He, Boyong; Gladfelter, Wayne L.; Hobbs, Christopher; Buchanan, Doug; Taylor, Charles; Gribelyuk, Michael; Tiner, Mike; Coppel, Matthew; Lee, Jang Jung., *IEEE Transactions on Electron Devices* **2001**, 48(10), 2348-2356 p) Roberts, J. T.; Gladfelter, W. L.; Campbell, S.; Burleson, D.; Hoelien, N.; Ma, T.; Smith, R., *Book of Abstracts, 219th ACS National Meeting, San Francisco, CA, March 26-30,* **2000** COLL-090

[4] V. Kaiser, S. Ebinal, F. Menzel and E. Stupp, *Z. Anorg. Allg. Chem.* **1997** 623, 449-455

[5] G. Tikhomirov, I. Morozov, K. Znamenkov, E. Kemnitz and S. Troyanov, *Z. Anorg. Allg. Chem.* **2002** 628, 872-876

[6] B.O. Field and C.J. Hardy, *Proc. Chem. Soc.* **1962** 76

[7] C.C. Addison and N. Logan, *Adv. Inorg. Chem. Radiochem.* **1964** 6, 72

[8] B.O. Field and C.J. Hardy, *Proc. Chem. Soc.* **1962** 76

[9] G. Tikhomirov, I. Morozov, K. Znamenkov, E. Kemnitz and S. Troyanov, *Z. Anorg. Allg. Chem.* **2002** 628, 872-876
[10] B.O. Field and C.J. Hardy, *J. Chem. Soc. Abstracts* **1964** (Nov) 5130-5234
[11] C.C. Addison and N. Logan, *Adv. Inorg. Chem. Radiochem.* **1964** 6, 72
[12] B.O. Field and C.J. Hardy *J. Chem. Soc.* **1963** 5278-5281
[13] A. Givan and A. Loewenschuss, *J. Chem. Phys.* **1989** 90, 11
[14] C.C. Addison, P.M. Boorman and N. Logan *J. Chem. Soc.* **1965** 4978
[15] Christos Sarantopoulos, Master's Thesis, CIRIMAT, ENCIACET, Toulouse, France
[16] Vahlas, Constantin; Caussat, Brigitte; Senocq, Francois; Gladfelter, Wayne L.; Sarantopoulos, Christos; Toro, David; Moersch, Tyler., *Proceedings - Electrochemical Society* **2005** 2005-09(EUROCVD-15), 221-228
[17] Vahlas, Constantin; Caussat, Brigitte; Senocq, Francois; Gladfelter, Wayne L.; Aloui, Lyacine; Moersch, Tyler. *Chemical Vapor Deposition* **2007**, 13(2-3), 123-129.
[18] Christos Sarantopoulos, Master's Thesis, CIRIMAT, ENCIACET, Toulouse, France
[19] Ibid
[20] This is the so called "Mohr method", which is described in G. Charlot, Les méthodes de la chimie analytique, Analyse quantitative minérale, Masson & Cie Ed., 1961, as well as many old analytical chemistry texts
[21] Viola & al. J. Chem. & Eng. Data; 22(4), 1977, pp 367-370
[22] Christos Sarantopoulos, Master's Thesis, CIRIMAT, ENCIACET, Toulouse, France
[23] Merrifield R.B. *J. Am. Chem. Soc.* **1963**, *85*, (14) 2149
[24] J.J. Hanak *J. Mat. Sci.* **1970**, *5*, 964
[25] Ichiro Takeuchi, Jochen Lauterbach and Michael J. Fasolka, *Materials Today* **Oct 2005**, 8 (10) 18-26
[26] Xiang X.D., Sun X.D., Briceno G., Lou Y.L., Wang K.A., Chang H.Y., Wallace-Freedman W.G., Chen S.W., Schultz P.G.A. *Science* **1995**, 268, (5218) 1738.
[27] Gabriel Briceño, Hauyee Chang, Xiaodong Sun, Peter G. Schultz, X. -D. Xiang *Science* **1995**, 270, (5234) 273-275
[28] van Dover R.B., Schneemeyer L.D., Fleming R.M. *Nature* **1998**, 392, (6672)162.
[29] Qi Wang, Guozhen Yue, Jing Li, Daxing Han *Solid State Communications* **2000**, 113, 175–178
[30] Hemantkumar N. Aiyer, Daikichi Nishioka, Ryuichirou Maruyama, Hiroyuki Shinno, Nobuyuki Matsuki, Kaori Miyazaki, Hiroshi Fujioka and Hideomi Koinuma *Jpn. J. Appl. Phys.* **2001**, 40, L81-L83
[31] Minami H., Itaka K., Ahmet P., Komiyama D., Chikyow T., Lippmaa M., Koinuma H., *Jpn. J. Appl. Phys. Part 2*, **2002** 41 (2A) L149.
[32] Wang Q., Perkins J., Branz H.M., Alleman J., Duncan C., Ginley D., *Appl. Surf. Sci.* **2002** 189 (3-4) 271.
[33] Charles J. Taylor and Steve Semancik, *Chem. Mater.* **2002**, *14,* 1671-1677
[34] a) Qi Wang, Fengzhen Liu, Daxing Han, *Macromol. Rapid Commun.* **2004**, 25, 326–329 b) Qi Wang, *Thin Solid Films* **2003**, 430, 78–82 c) Qi Wang, *Meas. Sci. Technol.* **2005**, 16, 162–166 d) Qi Wang; Page, M.; Yanfa Yan; Tihu Wang, *Photovoltaic Specialists Conference, 2005. Conference Record of the Thirty-first IEEE* **Jan 2005**, 3, 7, 1233 – 1236 e) N. Matsuki, Y. Abiko, M. Kobayashi, K. Miyazaki, H. Fujioka, H.

Koinuma, *Appl. Phys. A* **2004**, 79, 1413–1416 f) Hemantkumar N. Aiyer, Daikichi Nishioka, Ryuichirou Mayuyama, Hiroyuki Shinno, Nobuyuki Matsuki, Kaori Mayazaki, Hiroshi Fujioka and Hideomi Koinuma, *Jpn. J. Appl. Phys,* **2001**, 40, L81-L83 g) Tyler P. Martin and Karen K. Gleason, *Chem. Vap. Deposition* **2006**, *12*, 685–691 h) M.Y. Afridi, J.S. Suehle, M.E. Zaghoul, D.W. Berning, A.R. Hefner, R.E. Cavicchi, S. Semancik, C.B. Montgomery, and C.J. Taylor, *IEEE Sensors Journal*, **2002**, 2, 664-655 i) Cavicchi, R. E.; Semancik, S.; Di Meo, F., Jr.; Taylor, C. J. *Journal of Electroceramics* **2002**, 9(3), 155-164 j) C.J. Taylor, R.E. Cavicchi, C.B. Montgomery and S.M. Turner, *Nanotechnology*, **2004**, 15, 62-65 k) D.C. Meier, C.J. Taylor, R.E. Cavicchi, S. Semancik, E. White V, M.E. Ellzy and K.B. Sumpter, *IEEE Sensors Journal*, **2005**, 5, 712-725 l) Xiaonan Li, Timothy A. Gessert, Timothy Coutts, *Applied Surface Science* **2004**, 223, 138–143 m) Geoffrey Hyett and Ivan P. Parkin, *Surface & Coatings Technology* **2007**, 201, 8966–8970 n) Geoffrey Hyett, Mark A. Green, and Ivan P. Parkin, *J. Am. Chem. Soc.* **2007**, 129, 15541-15548 o) Tevye Kuykendall, Philipp Ulrich, Shaul Aloni and Peidong Yang, *Nature Materials* **Dec 2007**, 6, 951-956

[35] a) Jae-Ouk Choo and Raymond A. Adomaitis; Gary W. Rubloff, Laurent Henn-Lecordier, and Yijun Liu, *AIChE Journal* **Feb 2005**, 51 (2) 572-584 b) J. O. Choo and R. A. Adomaitis; L. Henn-Lecordier, Y. Cai, and G. W. Rubloff *Rev. Sci. Inst.* **2005**, 76, 062217 - 062217-10 c) Ramaswamy Sreenivasan and Raymond A. Adomaitis; Gary W. Rubloff, **J**. *Vac. Sci. Technol. B* **Nov/Dec 2006**, 24 (6) 2706-2715 d) Raymond A. Adomaitis, *Surface & Coatings Technology* **2007**, 201, 9025–9029 e) Yuhong Cai, Laurent Henn-Lecordier, and Gary W. Rubloff; Ramaswamy Sreenivasan, Jae-Ouk Choo, and Raymond A. Adomaitis *J. Vac. Sci. Technol. B* **Jul/Aug 2007**, 25 (4) 1288-1297 f) Ramaswamy Sreenivasan, Raymond A. Adomaitis, Gary W. Rubloff *Journal of Crystal Growth* **2008**, 310, 270–283

[36] Smith R.C., Hoilien N., Roberts J., Campbell S.A., Gladfelter W.L., *Chem. Mater.* **2002**, 14 (2) 474

[37] Ryan C. Smith, Noel Hoilien, Jimmy Chien, Stephen A. Campbell, Jeffrey T. Roberts, and Wayne L. Gladfelter, *Chem. Mater.* **2003**, *15,* 292-298

[38] Bin Xia, Fang Chen, Stephen A. Campbell, Jeffrey T. Roberts, and Wayne L. Gladfelter *Chem. Vap. Dep.* **2004**, *10*, No 4, 195-200

[39] Bin Xia, Ryan C. Smith, Tyler L. Moersch, Wayne L. Gladfelter *Applied Surface Science* **2004**, *223*,14–19

[40] Bin Xia, Yong S. Chu, and Wayne L. Gladfelter *Surface & Coatings Technology* **2007**, 201, 9041–9045

[41] Zhong L.J., Zhang Z.H., Campbell S.A., Gladfelter W.L., *J. Mater. Chem.* **2004**, 14 (21) 3203

[42] L. Zhong, F. Chen, S. A. Campbell, W. L. Gladfelter, *Chem. Mater.* **2004**, 16, 1098

[43] L. Zhong, W. L. Daniel, Z. Zhang, S. A. Campbell, W. L. Gladfelter, *Chem. Vap. Deposition* **2006**, 12, 143

[44] Rikka Puurunen, *Journal of Applied Physics*, **2005**, 97, 2, 121301-121301-52

[45] Charles B. Musgrave and Roy G. Gordon, *Future Fab. Intl.* **2005**, 18

[46] a) Roy G. Gordon, Jill Becker, Dennis Hausmann, and Seigi Suh, *Chem. Mater.* **2001**, *13,* 2463-2464 b) Dennis Hausmann, Jill Becker, Shenglong Wang, Roy G.Gordon,

Science **2002**, 298, 401-406 c) W. He and R. Solankia; J. F. Conley, Jr. and Y. Ono, *J. Appl. Phys.* **2003**, 94 (5) 3657-3659 d) Philippe de Rouffignac, Zhengwen Li, and Roy G. Gordon, *Electrochemical and Solid-State Letters*, **2004**, 7 (12) G306-G308 e) Zhong L.J., Zhang Z.H., Campbell S.A., Gladfelter W.L., *J. Mater. Chem.* **2004**, 14 (21) 3203 f) Lijuan Zhong, Weston L. Daniel, Zhihong Zhang, Stephen A. Campbell, and Wayne L. Gladfelter, *Chem. Vap. Deposition* **2006**, *12*, 143–150 g) K.A. Miller, C. John, K.Z. Zhanga, K.T. Nicholson, F.R. McFeely, M.M. Banaszak Holl, *Thin Solid Films* **2001**, 397, 78–82

[47] a) Jaehyun Kim and Kijung Yong, *Japanese Journal of Applied Physics* **2006**, 45 (6A) 5174–5177 b) H. S. Chang, S.-K. Baek, H. Park, H. Hwang, J. H. Oh, W. S. Shin, J. H. Yeo, K. H. Hwang, S. W. Nam, H. D. Lee, et al., *Electrochem. Solid-State Lett.* **2004**, 7, F42 c) Y. Senzaki, S. Park, H. Chatham, L. Bartholomew, and W. Nieveen, *J. Vac. Sci. Technol., A* **2004**, 22, 1175 d) K. Endo and T. Tatsumi, Jpn. *J. Appl. Phys., Part 2* **2003,** 42, L685

[48] a) H. Shin, D.-K. Jeong, J. Lee, M. M. Sung, and J. Kim, *Adv.Mater.* **2004**, 16, 1197 b) D. K. Jeong, N. H. Park, S. H. Jung, W. G. Jung, H. Shin, J. G. Lee, and J. Y. Kim, *Mater. Sci. Forum* **2004**, 449-452, 1165 c) D. Jeong, J. Lee, H. Shin, J. Lee, J. Kim, and M. Sung, *J. Korean Phys. Soc.* **2004**, 45, 1249 d) K. Kukli, M. Ritala, and M. Leskelä, *Chem. Vap. Deposition* **2000**, 6, 297 e) A. Nakajima, T. Kidera, H. Ishii, and S. Yokoyama, *Appl. Phys. Lett.* **2002**, 81, 2824 f) J. Park, B. Choi, N. Park, H. J. Shin, J. G. Lee, and J. Kim, *Integr. Ferroelectr.* **2002**, **48**, 23 g) H. Ishii, A. Nakajima, and S. Yokoyama, *J. Appl. Phys.* **2004**, 95, 536 h) D. Jeong, J. Lee, and J. Kim, *Integr. Ferroelectr.* **2004**, 67, 41 i) J. Koo, Y. Kim, and H. Jeon, *Jpn. J. Appl. Phys., Part 1* **2002**, 41, 3043 j) Y. Kim, J. Koo, J. Han, S. Choi, H. Jeon, and C.-G. Park, *J. Appl. Phys.* **2002**, 92, 5443 k) K. Endo and T. Tatsumi, *Jpn. J. Appl. Phys., Part 2* **2003**, 42, L685 l) K. Endo and T. Tatsumi, *Jpn. J. Appl. Phys., Part 2* **2004**, 43, L1296 m) M. Putkonen and L. Niinistö, *J. Mater. Chem.* **2001**, 11, 3141

[49] Karl W. Terry and T. Don Tilley, *Chem. Mater.* **1991**, 3, 1001-1003

[50] Karl W. Terry, Claus G. Lugmair, and T. Don Tilley, *J. Am. Chem. Soc.* **1997**, 119, 9745-9756

[51] Wei Lei, Laurent Henn-Lecordier, Mariano Anderle, and Gary W. Rubloff; Mario Barozzi and Massimo Bersani, *Journal of Vacuum Science & Technology B: Microelectronics and Nanometer Structures* **2006**, 24 (2) 780-789

[52] W. Lei, L. Henn-Lecordier, M. Anderle, Gary W. Rubloff, M. Barozzi, and M. Bersani, *J. Vac. Sci. Technol. B* **2006**, 24 (2), 780-789

[53] Henn-Lecordier, W. Lei, M. Anderle, and G.W. Rubloff, *J. Vac. Sci. Technol. B* **2007**, 25 (1) 130-139

[54] Smith R.C., Hoilien N., Roberts J., Campbell S.A., Gladfelter W.L., *Chem. Mater.* **2002**, 14 (2) 474

[55] Smith, R. C.; Hoilien, N.; Taylor, C. J.; Ma, T.; Campbell, S. A.; Roberts, J. T.; Copel, M.; Buchanan, D. A.; Gribelyuk, M.; Gladfelter, W. L., *J. Electrochem. Soc.* **2000**, 147, 3472-3476.

[56] Dennis Hausmann, Jill Becker, Shenglong Wang, Roy G.Gordon, *Science* **2002**, 298, 401-406

[57] M.A. Cameron and S.M. George, *Thin Solid Films*, **1999**, 348, 90-98
[58] Donald C. Bradley, *Chem. Rev.*, **1989**, 89, 1317-1322
[59] Rikka Puurunen, *Journal of Applied Physics*, **2005**, 97, 2, 121301-121301-52
[60] K. Kukli, M. Ritala, and M. Leskelä, *Chem. Vap. Deposition* **2000**, 6, 297
[61] Burleson, David J.; Roberts, Jeffrey T.; Gladfelter, Wayne L.; Campbell, Stephen A.; Smith, Ryan C., *Chemistry of Materials* **2002**, 14 (3) 1269-1276.
[62] Hella, Curtiss Jae, "The chemical vapor deposition of hafnium dioxide and hafnium dioxide/silicon dioxide nanolaminates." (PhD dissertation, University of Minnesota, 2006)

[63] van Dover, R.B.; Scheemeyer, L.F.; Fleming, R.M.; Huggins, H.A. *Biotechnol. Bioeng.* **1999**, *61*, 217-225
[64] van Dover, R.B.; Schneemeyer, L.F.; Fleming, R.M. *Nature* **1998**, *392*, 162-164
[65] van Dover, R.B; Schneemeyer, L.F. *IEEE Electron Device Lett.* **1998**, *19*, 329-331
[66] Oliver, S.F.; Abell, C., *Current Opinion in Chemical Biology* **1999**, *3*(3), 299-306.
[67] Merritt, A. T., Combinatorial Chemistry and High Throughput Screening **1998**, *1*(2), 57-72
[68] Zheng, Q.; Kyle, D.J., *Drug Discovery Today,* **1997**, *2*(6), 229-234.
[69] Osborne, Scott E.; Ellington, Andrew D., *Chemical Reviews* (Washington, D. C.), **1997**, 97(2), 349-370.
[70] L. Feldman, E.P. Gusev and E. Garfunkel, in *Fundamental Aspects of Ultrathin Dielectrics on Di-based Devices*, edited by E. Garfunkel, E.P. Gusev and A.Y. Vul' (Kluwer, Dordrecht, 1998) p.1
[71] D.A. Buchanan, IBM *J. Res. Dev*, **1999**, *43*, 245
[72] International Technology Roadmap for Semiconductors, **2000**, International Semitech (Austin)
[73] B. Brar, G.D. Wilk, A.C. Seabaugh, *Appl. Phys. Lett.* **1996**, *69*, 2728
[74] Ryan C. Smith, Noel Hoilien, Jeff Roberts, Stephen A. Campbell, and Wayne L. Gladfelter, *Chem. Mater.* **2002,** *14,* 474-476
[75] Ryan C. Smith, Noel Hoilien, Jimmy Chien, Stephen A. Campbell, Jeffrey T. Roberts, and Wayne L. Gladfelter, *Chem Mater*. **2003**, *15*, 292-298
[76] Ryan C. Smith, Noel Hoilien, Jeff Roberts, Stephen A. Campbell, and Wayne L. Gladfelter, *Chem. Mater.* **2002,** *14,* 474-476
[77] Ryan C. Smith, Noel Hoilien, Jeff Roberts, Stephen A. Campbell, and Wayne L. Gladfelter, *Chem. Mater.* **2002,** *14,* 474-476
[78] Ryan C. Smith, Noel Hoilien, Jimmy Chien, Stephen A. Campbell, Jeffrey T. Roberts, and Wayne L. Gladfelter, *Chem Mater*. **2003**, *15*, 292-298
[79] *ibid*
[80] www.cfdrc.com
[81] Vladimir Kudriatsev and Rupak Das, *PVP (American Society of Mechanical Engineers)* **2002** 448-1(Computational Technologies for Fluid/Thermal/Structural/Chemical Systems with Industrial Applications, Vol. 1) 101-111

[82] Alton J. Reich and Mahesh M. Athavale, *PVP (American Society of Mechanical Engineers)* **2002** 448-2(Computational Technologies for Fluid/Thermal/Structural/Chemical Systems with Industrial Applications, Vol. 2) 215-220

[83] Brian P. Riely, Jiang J. Liu, Hongden Shen, Gerard Dang, Wayne H. Chang, Y. Jiang, Z. Sikorski, T. Czyszanowski, Andrzej Przekwas *SPIE – The International Society for Optical Engineering* **2003,** 4986 (Physics and Simulation of Optoelectronic Devices XI), 343-354

[84] Sandip Mazumar and Alfred Kersch, *Proceedings – Electrochemical Society* **1999,** 99-10 (Advances in Rapid Thermal Processing), 435-442

[85] a) Ralf Lenigk, Robin H. Liu, David Rhine, Pankaj Singhal, Mahesh Athavale, Zhijian Chen, Piotr Grodzinski, *Abstract of Papers, 224th ACS National Meeting, Boston, MA, United States, August 18-22, 2002* **2002**, BIOT-027 b) Daniel J. McCall, Rajnish Changrani, Peter Roberts, Chia-Fu Chou, Frederic Zenhausern, *Itherm 2002, Intersociety Conference on Thermal and Thermomechanical Phenomenon in Electronic Systems, 8th, San Diego, CA, United States, May 30-June 1, 2002* **2002**, 1025-1032 c) A. Przekwas, V. Makhajani, M. Athavale, A. Klein, P. Bartsch, *Micro Total Analysis Systems 2000, Procedings of the μTAS Symposium, 4th, Enschede, Netherlands, May 14-18, 2000* **2000**, 561-564 d) Agata Przekwas, DeMing Wang, Vinod B. Makhijani, Andrzej J. Przekwas, *Microreaction Technology: Industrial Prospects, Proceedings of the International Conference on Microreaction Technology, 3rd, Frankfurt, Apr. 18-21, 1999* **1999**, 488-497

[86] a) E.V. Yakovlev, R.A. Talalaev, S. Yu. Karpov, Yu. A. Shpolyanskiy, Yu. N. Makarov, S.A. Lowrey *Materials Research Society Symposium Proceedings (2002)* **2002,** 616 (New Methods, Mechanisms and Models of Vapor Deposition) 153-158 b) S. Lowrey, A. Krishnan, I. Clark *NASA Conference Publication* **1999**, 209092 (NASA Microgravity Materials Science Conference, 1998) 399-405

[87] Sonya D. McCall, Klaus J. Bachmann, *Materials Research Society Symposium Proceedings* **2002**, 693 (GaN and Related Alloys – 2001), 73-80

[88] E.V. Yakovlev, Yu. A. Shpolyanskiy, R.A. Talalaev, S. Yu. Karpov, Yu. N. Makarov, T. Bergunde, S.A. Lowrey, *Proceedings – Electrochemical Society* **2001**, 2001-13 (Fundemental Gas-Phase and Surface Chemistry of Vapor Phase Deposition II), 292-299

[89] a) G. J. Schoof, C.R. Kleijn, H.E.A. Van der Akker, T.G.M. Oosterlaken, H.J.C.M. Terhorst, F. Hussen, *PVP (American Society of Mechanical Engineers)* **2002**, 448-1 (Computational Technologies forFluid/Thermal/Structural/Chemical Systems with Industrial Applications, vol 1) 101-111 b) G.J. Schoof, C.R. Kleijn, H.E.A. Van der Akker, T.G.M. Oosterlaken, H.J.C.M. Terhorst, F. Hussen, *Journal de Physique IV: Proceedings* **2002**, 12 (Pr4 Thirteenth European Conference on Chemical Vapor Deposition, 2001), Pr4/51-Pr4/61 c) A.S. Segal, A.V. Kondratyev, A.O. Galyukov, S. Yu. Karpov, Yu. N. Makarov, W. Siebert, P. Storck, S. Lowrey, *Proceedings – Electrochemical Society* **2000**, 2000-13 (CVDXV), 456-463 d) Vikram Singh, Butch Verney, Anantha Krishnan, *Journal of Vacuum Science and Technology, A: Vacuum, Surfaces and Films* **1996**, 14 (3, Pt.1), 1252-1257

[90] Smith, R. C.; Hoilien, N.; Taylor, C. J.; Ma, T.; Campbell, S. A.; Roberts, J. T.; Copel, M.; Buchanan, D. A.; Gribelyuk, M.; Gladfelter, W. L. *J. Electrochem. Soc.* **2000**, *147*, 3472-3476.
[91] Kim, H.-S. *J. Appl. Phys.* **1998**, *85*, 3278
[92] David J Burleson, Jeffrey T. Roberts, Wayne L. Gladfelter, Stephen A. Campbell, and Ryan C. Smith, *Chem Mater*. **2002**, *14*, 1269-1276
[93] K. Riedling, *Thin Solid Films*, **1981**, *75*, 355-369
[94] K. Riedling, *Thin Solid Films*, **1981**, *75*, 355-369
[95] D.C. Bradley and J.D. Swanwick, *J. Chem. Soc.* **1959**, 748-752
[96] David J Burleson, Jeffrey T. Roberts, Wayne L. Gladfelter, Stephen A. Campbell, and Ryan C. Smith, *Chem Mater*. **2002**, *14*, 1269-1276
[97] M.A. Cameron, S.M. George *Thin Solid Films* **1999** *348*, 90-98
[98] Donald C. Bradley, *Chem Rev.* **1989**, 1317-1322
[99] Sandip Mazumder and Samuel A. Lowry, CFD Research Corporation Publication: *The Importance of Predicting Rate-Limited Growth for Accurate Modeling of Commercial MOCVD Reactors*
[100] N.K. Ingle, C. Theodoropoulos, T.J. Mountziaris, R.M. Wexler, F.T.J. Smith, *Journal of Crystal Growth* **1996**, *167*, 543-556
[101] Alaxandre Ern, Vincent Giovangigli and Mitchell D. Smooke, *Journal of Computational Physics*, **1996**, *126*, 21-39
[102] J. Adam and M.D. Rogers, *Acta Cryst.* **1959**, *12*, 951
[103] David J Burleson, Jeffrey T. Roberts, Wayne L. Gladfelter, Stephen A. Campbell, and Ryan C. Smith, *Chem Mater*. **2002**, *14*, 1269-1276
[104] M.A. Cameron, S.M. George *Thin Solid Films* **1999** *348*, 90-98
[105] Charles J. Taylor, David C. Gilmer, Daniel G. Colombo, G.D. Wilk, Shephen A. Campbell, Jerr Roberts, and Wayne L. Gladfelter, *J. Am. Chem. Soc.* **1999**, *121*, 5220-5229
[106] Sandip Mazumder and Samuel A. Lowry, CFD Research Corporation Publication: *The Importance of Predicting Rate-Limited Growth for Accurate Modeling of Commercial MOCVD Reactors*
[107] www.jawoollam.com